Effect of Surface Morphological Changes on Flow over a Sphere

Thesis by

Adam Norman

In Partial Fulfillment of the Requirements

for the Degree of

Doctor of Philosophy

California Institute of Technology

Pasadena, California

2010

(Defended April 16, 2010)

To Chondra and Eli

Acknowledgments

I would like to begin by thanking my advisor, Professor Beverley McKeon. The past four years in her research group have been very enjoyable. I am grateful that Beverley gave me a certain amount of freedom to guide my own research, while at the same time always encouraging me to think more deeply and theoretically. My years in her group would not have been the same without the amazing research group that built up over time.

I greatly appreciate the enthusiasm and thoughtful discussions with my various committee members: Tim Colonius, Mory Gharib, Fazle Hussain, Tony Leonard, and Dale Pullin. Special thanks go to Fazle for being on my committee even though it required travel.

This work was improved by the help of many other people. In particular I would like to thank Dr. Eric Kerrigan from Imperial College London for teaching me so much about control theory, and for spending time getting the motor controller working so well, which made some of this research possible. I would also like to thank Dr. Luca Maddalena for his input on my design, and Jeff LeHew for showing me how to build a power-boosting circuit.

I also appreciate the help of the aeroshop staff, particularly Ali for his precise workmanship on much of my design. The administrative staff was also great, always willing to help. I was also lucky to share an office with many great people.

I have benefited from the friendship of many people while at Caltech, though I must thank Geoff Ward in particular. We have enjoyed many games of ping-pong, tennis, and racquetball, along with many other activities outside of Caltech.

Thanks must also go to my flight instructor, Joe Areeda, who shared his passion of flying with me. He did not charge me nearly enough for flying lessons, and his response was that it did not matter because there was no other job with such a great view out the window. Though I have not had much time to fly since getting my pilot's license, I often dream of being up in the sky when I am sitting at my desk.

The most important acknowledgments go to my family. My parents and brother have always believed in me, giving me the confidence to pursue my dreams. In addition, I appreciate the encouragement of my wife's family, who are much more than just in-laws to me. Finally, this work simply would not have been possible without the love and support of my wife. While in California we have enjoyed many great adventures together, the most exciting being raising our wonderful son, who is 18 months old at the time of writing.

Support from the National Science Foundation under Grant No. 0747672 is gratefully acknowledged.

Abstract

An experimental investigation was undertaken to examine the effect of a morphing surface on the flow over a sphere in the Reynolds number range of 5×10^4 to 5×10^5. Here, a morphing surface is defined as a continuous surface that undergoes small amplitude changes in order to excite flow instabilities, rather than utilizing large mechanical changes to the overall shape as with traditional aerodynamic control surfaces. The sphere was chosen as an ideal geometry for testing morphing surfaces, because of the well-known sensitivity of the flow to small asymmetries on the surface. In this study, an approximation of a morphing surface was made by dynamically moving a small isolated roughness element along the sphere, thus producing small amplitude time-dependent changes to the surface shape. An experimental apparatus was designed that produced the actuation with an internal motor, which moved the roughness element via magnetic interaction. A three-component piezoelectric force sensor placed inside the sphere allowed for accurate, instantaneous measurements of the global effect of the actuator on the flow. It was found that the moving roughness could produce an instantaneous lateral force as large as the drag. Simultaneous force and particle image velocimetry measurements in the subcritical regime were used to show that there is a relatively long timescale associated with the instability growth, entrainment of fluid, and local change of the position of separation. This allowed the roughness to trip an extended region of the flow at once. It is shown that the three-dimensionality of the disturbance leads to the production of two helical counter-rotating vortices in the wake. In addition, it is demonstrated that a mean side force can be obtained by oscillating the roughness element about a point, producing a lateral force an order of magnitude larger than the force caused by a stationary roughness element. Finally, the results from the dynamic roughness were used to help interpret the underlying physical mechanisms that govern the forcing on a smooth sphere.

Contents

List of Figures

Nomenclature

$\hat{t}$	Dimensionless time $= tU_\infty/D$
μ	Dynamic viscosity
ω^*	Dimensionless angular frequency of stud $= \dot{\theta}_k D/U_\infty$
ϕ	Streamwise angle
ρ	Fluid density
θ	Spanwise angle
$\vec{C}_L$	Lateral force coefficient $= C_y\hat{y} + C_z\hat{z}$
C_D	Drag coefficient $= F_D/(\frac{1}{2}\rho U_\infty^2 \pi \frac{D^2}{4})$
C_i	Force coefficient $= F_i/(\frac{1}{2}\rho U_\infty^2 \pi \frac{D^2}{4})$, for $i = x$, y, or z
D	Sphere diameter
f	Frequency
k	Characteristic roughness scale
Re	Reynolds number $= \rho U_\infty D/\mu$
St	Strouhal number $= fD/U_\infty$
U_∞	Free stream velocity

Chapter 1

Introduction

1.1 Motivation

The research detailed in this thesis is motivated by the broad goal of understanding the effect of morphing surfaces on wall-bounded flows, with the aim of improving performance and efficiency for a wide range of technologies, as well as utilizing these surfaces to gain insight into the fundamental physical mechanisms that govern the behavior of the flow.

A morphing surface is different from traditional control surfaces, such as flaps on an aircraft, in that there is a continuous surface (a "skin"). The interest is in exciting and utilizing flow instabilities to coerce the flow to perform as desired, with minimal energy input. This is accomplished by making small amplitude, targeted changes to the surface, rather than large mechanical changes to the overall shape.

Because true morphing surfaces with a quick response time are not currently readily available, an experimental apparatus was developed which mimics some of the desired features. In order to demonstrate the potential of a morphing surface, a sphere was chosen as the base geometry, because it is well known that the flow is extremely sensitive to small changes in the surface condition. Instead of examining the effect of a true morphing skin, small amplitude changes to the surface were produced by moving a small isolated roughness element (a "stud") along the sphere surface at a fixed streamwise angle. Because the flow is so sensitive to the surface finish, the stud was held in place by a small magnet located inside the hollow sphere, which was itself moved with the use of a small motor, removing the need to have slots or other discontinuities.

The flow regime examined in this study was that of flow over a sphere in which there is a large turbulent wake, with flow separation occurring near the equator. This "bluff body" flow is characterized by two instabilities, that of the wake and that of the free shear layer. Many objects in daily use are bluff, from cars to sports balls. Understanding why the flow separates, and how it can be enticed to remain attached, allows for the possibility of making more-efficient and better-performing devices. In addition, the dynamics of the separation share some similarities with stalled airfoils, as will be discussed in chapter 5.

The effect of the morphing surface was primarily determined with the use of a time-resolved three-component force sensor, and supplemented with simultaneous particle image velocimetry and hot-film mea-

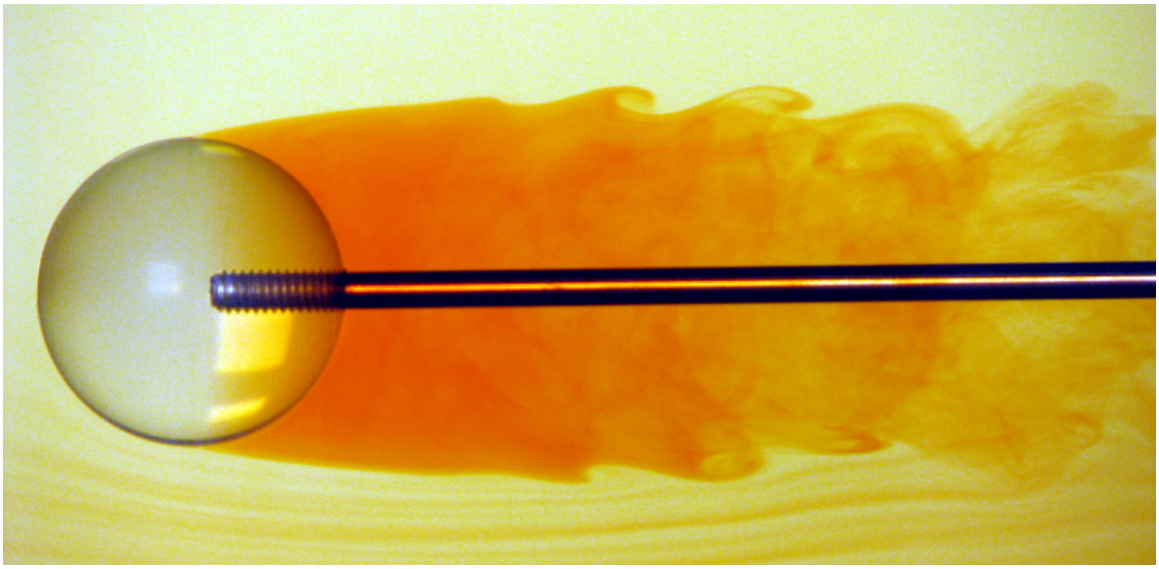

Figure 1.1: Dye visualization at a Reynolds number of 3.8×10^3, showing the roll-up of the shear layer in the near wake.

surements when needed to interpret the force measurements. As will be shown, a single moving roughness element has a profound effect on the flow, dramatically altering the separation point over the entire sphere, and completely changing the dynamics of the wake. In addition, the response of the flow to the prescribed disturbance provided a better understanding of sphere flow in general.

This is a first step toward understanding the effect of a dynamic surface on the flow field and forces, and paves the way for future studies which will utilize true morphing surfaces. In addition, it is demonstrated that the new experimental apparatus is an excellent testbed for examining the effectiveness of morphing surfaces.

1.2 Background

The flow field around a sphere is very rich (see, e.g. figure 1.1), beckoning theorists, numerical modelers, and experimentalists alike. Here is given a brief overview of the literature that is relevant to the current study.

1.2.1 Flow Over a Smooth Sphere

Despite geometrical axisymmetry, aspects of the complexity of flow over a sphere for a wide Reynolds number range (where $Re = \rho U_\infty D/\mu$ is based on sphere diameter D, free stream velocity U_∞, density ρ, and dynamic viscosity μ) are well known and reported in the literature. The instabilities of the wake and the sensitivity of the flow to perturbations to either the external flow field or the sphere surface lead to asymmetry of the separation line and wake in the instantaneous and/or mean senses on long and short timescales, depending on the Reynolds number. As noted by Willmarth & Enlow (1969), the unsteady forces on a sphere have been observed since the time of Newton, and their exact nature has continued to remain elusive, despite

the ubiquity of spheres in sports.

For the Reynolds numbers of this study, there are three flow regimes of interest. In the subcritical regime, laminar boundary layer separation occurs at about 80°, producing a large mean drag coefficient that is nearly independent of Reynolds number. Following this is the critical regime, which is associated with the separation location moving from about 80° to 120°, causing a rapid drop in the drag coefficient (the "drag crisis"), and ending at the lowest drag state, the "critical Reynolds number". In this regime the global flow is highly dependent on the condition of the boundary layer and in particular the transition process. In the supercritical regime, a separation bubble which decreases in size as the Reynolds number is increased has been identified using oil film visualization (Taneda, 1978; Suryanarayana & Prabhu, 2000). Achenbach (1972) did not detect the separation bubble in the supercritical regime when measuring the shear stress, though the previously cited studies and the similarities to cylinder flow (Roshko, 1961) suggest that it is present and contributes to producing the low drag state. At higher Reynolds numbers (beyond the scope of this study), the drag begins to increase again, transitioning to the transcritical regime, which begins when the point of boundary layer transition begins to move upstream (Achenbach, 1972).

There is conflicting evidence concerning the mean lateral force in the supercritical regime. Taneda (1978) observed a mean wake offset, corresponding to a side force, in early experiments. The observation that the direction of this offset could be manipulated using a small stud positioned on the sphere surface suggests that this could be the result of an initial asymmetry in the experiment. In simulations of sphere flow, the investigations of Constantinescu & Squires (2004) also showed a mean supercritical side force, although the authors noted this may be a result of the relatively short simulations rather than a physical result.

The fluctuating, three-component force distribution acting on the sphere reflects the instabilities and structure of the wake. For sphere Reynolds numbers above approximately 800 and below the critical Reynolds number, $Re_{crit} = \mathrm{O}(10^5)$, frequencies corresponding to both a small-scale shear layer instability and a larger wake instability dominate the force spectrum, while below this lower limit only the larger scale is observed (Sakamoto & Haniu, 1990; Kim & Durbin, 1988; Bakić & Perić, 2005; Achenbach, 1974*b*). With increasing Reynolds number the Strouhal number ($St = fD/U_\infty$, where f is the frequency) of the shear instability increases as Re^n (Kim & Durbin, 1988), with $0.5 \leq n < 1$ for $10^3 < Re_D < 10^5$, while the large-scale Strouhal number remains approximately equal to 0.2, typical of vortex shedding. The wake instability has been described as both a helical instability (Chomaz *et al.*, 2006) and as vortex shedding in a randomly rotating azimuthal plane (Sakamoto & Haniu, 1990). In the subcritical regime, computational studies (Yun *et al.*, 2006; Constantinescu & Squires, 2004) have also found evidence of low frequency oscillations of the wake, below that of the large-scale vortex shedding frequency.

Though the mean drag force has been measured by many researchers, the literature concerning the dynamic forces on a sphere is sparse. In the subcritical regime, Lauchle & Jones (1998) indirectly measured the forces on a suspended sphere using an accelerometer, obtaining the decay of the frequency spectrum for $St > 1.5$. For the supercritical regime, Willmarth & Enlow (1969) reported the experimentally obtained fre-

quency spectrum and the mean squared lift for the case of a rough sphere. The subcritical Reynolds number range has been examined computationally by Yun *et al.* (2006) with large eddy simulation (LES), while both the subcritical and supercritical regimes have been investigated by Constantinescu & Squires (2004) using detached eddy simulation (DES). The phenomenological model for subcritical *Re* developed by Howe *et al.* (2001) by considering the spectra developed by the shedding of randomly oriented vortex rings appears to give reasonable agreement with the trends in the existing literature for high St.

The combination of axisymmetry, extreme sensitivity of the flow to boundary conditions, and the long sampling times required to obtain converged statistics make this a challenging flow to investigate either experimentally or numerically, especially in comparison to the nominally two-dimensional flow over a cylinder. In particular, obtaining the three-dimensional velocity field required to fully capture the sphere wake remains challenging in experiments, while the resolution requirements imposed by a very thin (possibly transitioning) boundary layer and a broad wake, combined with the low frequency content, are numerically exacting.

1.2.2 Effect of Static Changes to the Sphere Shape

Though the effect of distributed surface roughness on the mean drag force experienced by a fixed sphere in uniform flow has been examined in detail (e.g., Achenbach, 1974*a*; Choi *et al.*, 2006), there are few studies that consider asymmetric roughness distribution or isolated roughness elements. In the presence of distributed roughness the boundary layer at all azimuthal locations transitions to a turbulent state at a lower Reynolds number than it does for the smooth sphere, reducing the critical Reynolds number at which the flow changes from the high drag subcritical regime to the lower drag supercritical regime. This phenomenon is used as a control technique in the familiar example of the dimpled surface of golf balls, designed to maximize the velocity range during which the ball experiences the low drag regime. Similar drag curves have been observed by using a two-dimensional trip wire (Maxworthy, 1969). For a rough sphere beyond the critical regime, the drag increases well beyond smooth sphere levels (Achenbach, 1974*a*).

When the symmetry of the surface condition is broken, the condition of the boundary layer has an azimuthal dependence that is reflected in the mean separation location and therefore the mean force vector. Mehta (1985) notes that a positive side force at subcritical *Re*, and a negative side force at supercritical *Re* was recorded by Hunt in experiments on a half-roughened cricket ball. If instead of distributed roughness there is a single isolated roughness element (a "stud"), both the streamwise angle, ϕ_k (see figure 2.2) and the local Reynolds number, $Re_k = \rho U_k D_k / \mu$, must be considered, where U_k is the local velocity at the top of the stud. For Re_k above about 500, the flow behind a small element is expected to separate and rapidly becomes turbulent. Morkovin (1985) notes that at Re_k above about 450, intertwined hairpin vortices form behind an element in a zero pressure gradient boundary layer. Therefore it is expected that if Re_k is large enough the stud will cause a region of transition of the boundary layer, of extent dependent on the details of the local boundary layer, and will potentially alter the location of boundary layer separation.

The roughness element will disturb the base flow, which has distinct features in the subcritical and su-

percritical regimes. The subcritical near wake is approximately the size of the sphere, and experiments and numerical simulations (e.g., Taneda, 1978; Yun *et al.*, 2006)) have shown periodic vortex shedding at a Strouhal number ($St = fD/U_\infty$) of about 0.2, with an apparently random orientation. The boundary layer separates at approximately $\phi = 80^\circ$ (Achenbach, 1972), and the shear layer subsequently rolls up, forming vortex tubes with a Strouhal number that increases with *Re* (Sakamoto & Haniu, 1990). In the supercritical regime using smoke visualization, Taneda (1978) observed that the wake was much smaller and composed of a pair of offset counter-rotating vortices, with circulation such that they pushed each other away from the sting. Constantinescu & Squires (2004) found a similar wake offset in their detached-eddy simulations, and also found the shedding of hairpinlike vortices at $St \approx 1.3$. Taneda (1978) visualized the boundary layer by covering the sphere with oil and examining the resultant pattern. He found that, on average, the supercritical boundary layer separates laminarly at about $\phi = 100^\circ$, after which there is a recirculation bubble with turbulent reattachment at about $\phi = 117^\circ$, and turbulent separation at about $\phi = 135^\circ$.

Several studies have been performed that can be used to identify the influence of an isolated roughness element. Bacon & Reid (1924) examined the effect of their supporting spindle (diameter not stated) as a function of angle, at supercritical *Re*, finding that the largest drag coefficient, C_D, occurred for a streamwise spindle angle of $\phi \approx 77^\circ$. They also examined the effect of a support wire with diameter $0.0023D$ at supercritical *Re*, at several streamwise angles. At $\phi = 60^\circ$ the wire only had a small effect, but at 67.5°, 80°, and 90° the drag nearly doubled for $3 \times 10^5 < Re < 4 \times 10^5$. In addition, Taneda observed that the orientation of the mean supercritical wake offset could be controlled by placing a stud at $\phi_k = 90^\circ$.

1.2.3 Active Manipulation of the Flow

There have been far fewer studies examining the use of active methods for altering the flow over a sphere. Kim & Durbin (1988) acoustically excited the flow instabilities, leading to an increase in drag. Jeon *et al.* (2004) were able to achieve a drag reduction at a subcritical *Re* of 10^5 by applying periodic blowing and suction just upstream of the separation point, producing a similar effect as dimples. They attributed this to exciting the boundary layer instability, which lead to a delayed separation and a laminar separation bubble (similar to the supercritical state).

Though the geometry of the body plays an important role in the specific dynamics of the separation, the fundamental mechanism is the same: fluid entrainment keeps a flow attached that would otherwise separate. In the context of an airfoil at a high angle of attack, Seifert *et al.* (2004) note that in order to keep the flow attached using periodic excitation, between one and four vortices from the actuator must be over the body at all times. Darabi & Wygnanski (2004*a*,*b*) describe the temporal evolution of the attachment process, showing that when periodic excitation is abruptly started, the peak lift can be obtained within a dimensionless time of about $\hat{t} \equiv tU_\infty/D = 16$ (where D is the characteristic length, in this case the chord). They also examined the separation process, finding that when the forcing is abruptly stopped, the flow becomes fully detached after about $\hat{t} = 20$.

Table 1.1: Parameter space investigated in this thesis. The stud is a circular cylinder with width and height k, and stud parameters are indicated with a k subscript. The entire parameter space of the first three parameters was investigated and used to select a more narrow parameter space for the dynamic stud ($k/D = 0.01$ and $\phi_k = 60^\circ$).

Property	Range	Description
$Re = \rho U_\infty D/\mu$	5×10^4 to 5×10^5	Reynolds number
k/D	0.01, 0.02, 0.04	Dimensionless size of the stud
ϕ_k	10° to 120°	Streamwise angle of stud
$\omega^* = \dot{\theta}_k D/U_\infty$	0 to 1.1	Dimensionless angular frequency of the stud

Using plasma actuation on a circular cylinder, Jukes & Choi (2009*a*,*b*) examined the effect of a single short pulse near the subcritical separation point, finding that the flow was modified for up to $\hat{t} = 40$ after the pulse. Flow visualization revealed that the pulse produced a spanwise vortex, which traveled downstream and momentarily changed the separation point to about 120°. Similarly, Williams *et al.* (2009) examined the effect of a single blowing/suction pulse near the leading edge of a low Reynolds number stalled airfoil, finding that after the disturbance is introduced into the flow, the lift gradually increases until it reaches a maximum after $\hat{t} \approx 3$, and then the lift decays in a similar amount of time.

1.3 Thesis Outline

An integral part of this research was the design of an experimental apparatus which was capable of answering fundamental questions related to the unsteady forces on a sphere, along with the ability to instantaneously determine the effect of surface actuation. This design is detailed in chapter 2. In chapters 3 and 4 the framework is laid for understanding the effect of surface actuation by taking a close look at the unsteady forces and the effect of in isolated roughness element on the flow field. In chapter 5 the significant effect that a small dynamic roughness element has on flow separation and the near wake is examined in detail, where the stud is moved in the azimuthal direction, θ (see figure 2.2). Table 1.1 lists the parameter space investigated in this study. Lastly, our most significant findings are summarized, and suggestions for future work are provided.

Chapter 2

Experimental Methods

2.1 Experimental Facility

The experiments were performed in the temperature controlled 61 cm $\times$ 61 cm $\times$ 244 cm recirculating Merrill wind tunnel at the California Institute of Technology, which is powered by a 12 kW (50 HP) variable speed AC induction motor. The motor rpm was controlled with a variable frequency inverter, and the fan pitch was adjusted to minimize the free stream turbulence (controlled with a pressure regulator, which was set for 83 kPa). The free stream turbulence intensity, as measured by a hot wire located at the entrance of the test section, was $\sqrt{\overline{u'u'}}/U_\infty < 0.3\%$, similar to that used by Achenbach (1972) and Willmarth & Enlow (1969) (where $u'(t) = u(t) - \overline{u}$ is the streamwise fluctuating velocity and $\overline{u}$ is the mean velocity at a point). The dynamic pressure was measured at the entrance of the test section using a pitot-static probe from United Sensor, along with an MKS 220D pressure transducer, with a useful range of up to 2600 Pa. This was converted to velocity by using Bernoulli's principle and taking into account the temperature, atmospheric pressure, and humidity. The test section velocity ranged from about 5 m/s to 50 m/s, corresponding to a unit Reynolds number range of about 3.3×10^5 to 3.3×10^6 per meter, and a Mach number of at most 15%.

2.2 Model and Test Stand

In order to measure the unsteady forces on a sphere, a new apparatus was constructed which consisted of a rigid test stand mounted to an optical table, a lightweight sphere, a three-component piezoelectric force sensor, and a hollow sting to allow for the passage of wires (figure 2.1). In addition, the unsteady flow was examined using hot-film and particle image velocimetry measurements (PIV).

2.2.1 Coordinate System

In order to account for the time-dependent nature of the forces on the sphere due to the unsteady wake, the following notation was used. The force vector is written as $\vec{C}_F(\hat{t}) = C_D(\hat{t})\hat{x} + C_y(\hat{t})\hat{y} + C_z(\hat{t})\hat{z}$ (figure 2.2),

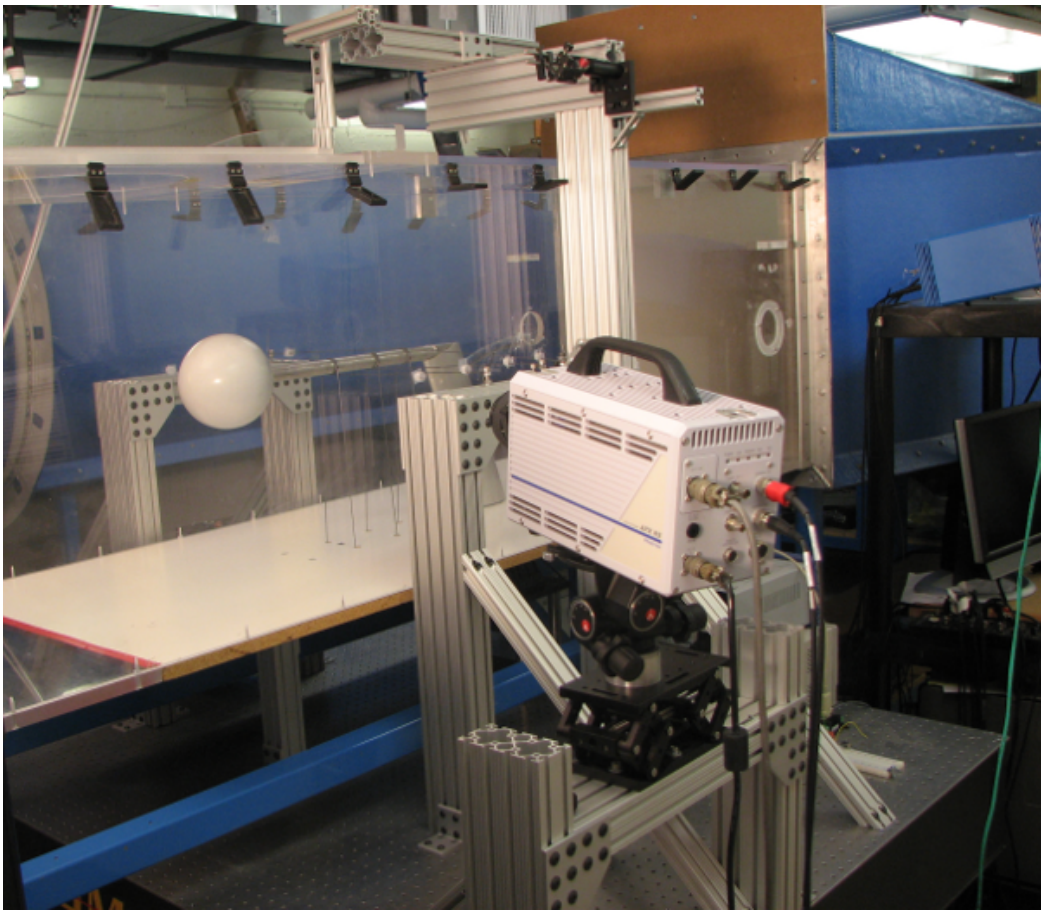

Figure 2.1: Sphere centered in test section, showing the support structure for the sting and the piano wires, along with the PIV camera and optical table.

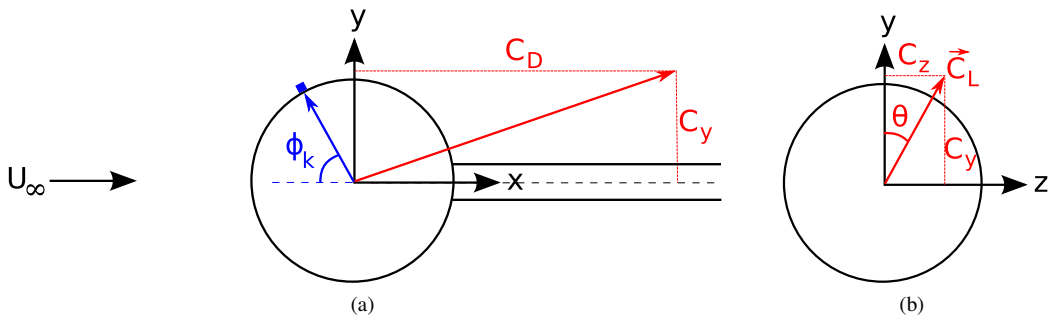

Figure 2.2: (a) Coordinate system chosen with x as the streamwise direction. The streamwise angle from the stagnation point is ϕ, with the k subscript indicating the streamwise angle to the stud. The drag coefficient is labeled C_D. (b) Looking downstream: the lateral force coefficient vector is labeled $\vec{C}_L$, and is composed of $C_y\hat{y}+C_z\hat{z}$. θ is the lateral angle from the y-axis to $\vec{C}_L$.

where $\hat{t}=tU_\infty/D$ is the dimensionless time, and $\hat{x}$, $\hat{y}$, and $\hat{z}$ are unit vectors. The lateral force vector is defined to be $\vec{C}_L(\hat{t})=C_y(\hat{t})\hat{y}+C_z(\hat{t})\hat{z}$, with the lateral angle to $\vec{C}_L(\hat{t})$ being $\theta(\hat{t})$. The mean lateral force (which should be zero for symmetric flow) is given by $\overline{\vec{C}}_L=\overline{C}_y\hat{y}+\overline{C}_z\hat{z}$, and the fluctuating forces are indicated by a prime, $C_y(\hat{t})=\overline{C}_y+C'_y(\hat{t})$. The magnitude of the lateral force as a function of time is $|\vec{C}_L(\hat{t})|=\sqrt{C_y(\hat{t})^2+C_z(\hat{t})^2}$, which is always greater than zero due to the unsteady flow. The streamwise angle from the stagnation point is labeled ϕ, and the k subscript is used to indicate the position of the stud.

2.2.2 Rigid Stand

Considerable attention was paid to the sphere support system with a view to minimizing its effect on the sphere wake while keeping the natural frequency high in order to optimize the frequency range of forces that could be resolved. A stainless steel sting with an outside diameter of 2.54cm, an inside diameter of 1.27cm, and length 39cm beyond $x/D=0.5$ was attached to a 5cm x 2.5cm stainless steel beam tilted 15° with respect to the flow direction normal. A streamlined fairing covered the beam to reduce blockage effects (see figure 2.3).

The sting diameter was selected based on a study of the influence of the ratio of sting to sphere diameter on the wake statistics (see appendix A). It was concluded that in the subcritical regime the presence of the sting has a negligible effect on the velocity statistics for $D_{sting}<0.25D$, approximately. In the supercritical regime, however, Hoerner (1935) has shown a noticeable decrease in the measured mean drag with increasing relative sting size, an enhanced sensitivity that should be expected due to the narrower supercritical wake. Nevertheless, for the sting size used in this study, $D_{sting}/D=0.17$, only a negligible change to the wake should be expected.

The addition of piano wires with a diameter of 0.1cm to anchor the sting at three streamwise locations ($x/D=1.5$, 2.1, and 2.6) increased the minimum natural frequency of the system from about 35Hz to 75Hz, or from $St=0.1$ to 0.2 at $Re=5\times10^5$ (worst case). The position of the closest supporting wires was chosen

as a compromise between increasing the natural frequency and minimizing the disturbance to the flow. Wires placed at $x/D = 0.8$ noticeably altered the statistics of the unsteady forces, whereas there was only a small broadband change in the spectral density centered on $St = 0.1$ at high subcritical Reynolds numbers when the closest wires were at $x/D = 1.5$. The minimum wire Reynolds number was 300, indicating that vortex shedding occurs behind the wires over the Reynolds numbers investigated in this study, with a potential influence on the development of the shear layer. However a downstream wire location of $x/D = 1.5$ meant that the wires were located essentially downstream of the recirculating wake region, which was observed using particle image velocimetry to have a mean reattachment point (the point were the mean streamwise velocity is zero) of $x/D = 1.43$ at a subcritical Re of 2.1×10^5 and an $x/D = 0.63$ at a supercritical Re of 4.1×10^5.

2.2.3 Sphere Model

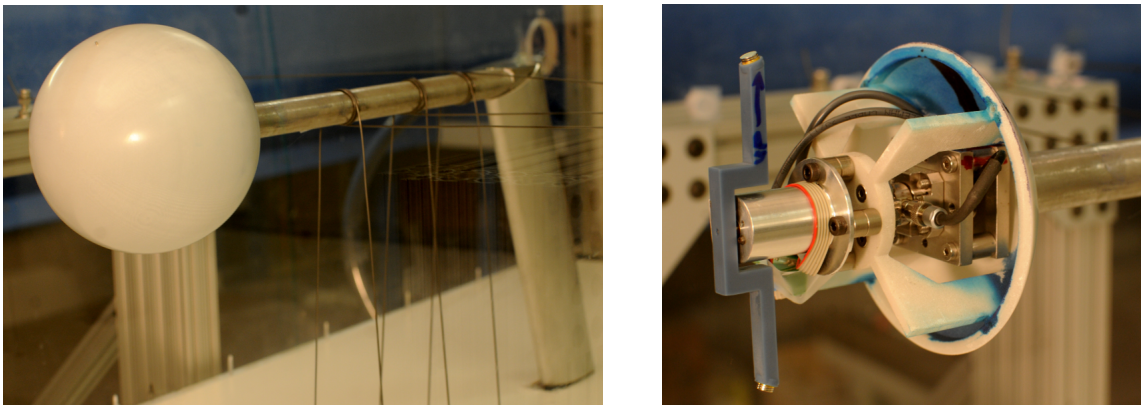

(a) (b)

Figure 2.3: (a) Model in 61cm by 61cm recirculating wind tunnel test section, with piano wires used to increase the natural frequency of the sphere-support system. (b) Inside of the sphere showing the motor, motor arm and magnet, and three-component force sensor attached to a stainless steel base.

Two different sphere models were produced, one for the basic measurements, and then one with a low friction coating for the dynamic roughness element experiments. Both had a diameter of $D = 15$cm and were rapid prototyped, consisting of two hollow pieces with a smooth seam located at $\phi = 125°$, i.e. downstream of the supercritical separation point (Achenbach, 1972) (figure 2.3). The internal structure was designed such that it was rigid and allowed room for the placement of the force sensor and steel mount, which attached to the sting while leaving room for the passage of wires.

The basic sphere was ordered from American Precision Prototyping, and was fabricated using the stereolithography Accura Bluestone plastic, with an out-of-round build tolerance of $\pm 0.002D$, and was subsequently sanded to 600 grit to remove stair stepping, which gives a conservative estimated rms surface roughness of $k/D \approx 1 \times 10^{-4}$. A varnish coating was then applied to the sanded surface to further improve the

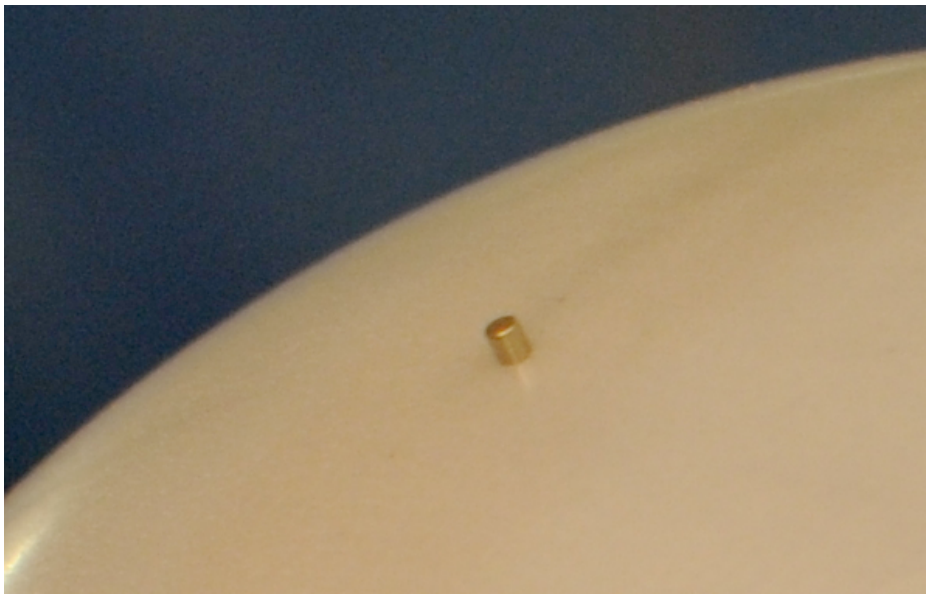

Figure 2.4: Stud with a width and height of $k/D = 0.01$, held in place with a magnet that is inside of the sphere.

finish. The low friction sphere was ordered from Scicon Technologies and was fabricated using selective laser sintering with the DuraForm HST plastic, after which it was finished and a Teflon coating was applied. The accuracy of this surface finish was more stringent than that of the basic sphere, in order to provide a smooth, low friction surface for the roughness element.

2.2.4 Surface Actuation

Surface actuation was achieved with a hollow-core DC motor that was placed inside the sphere (figure 2.3b). The arm, attached to the motor shaft, had a magnet on the end of it which was positioned about 3mm from the outside surface of the sphere, where a small cylindrical magnet was placed (henceforth the "stud"). As the motor shaft turned, it pulled the stud along the azimuthal direction. The position of the stud was determined from a magnetic encoder attached to the motor, which produced 512 square wave pulses per revolution in two channels (to indicate the direction of rotation). A high-speed camera revealed that the stud followed the motor arm to within about $\pm 2^\circ$. The streamwise angle of the stud was chosen to be $\phi_k = 60^\circ$, because a static stud produces the largest force close to this angle (see chapter 4). The advantage of pulling the stud by using a magnet was that no holes or gaps needed to be machined in the sphere, allowing for a continuous, polished surface.

The stud consisted of a neodymium magnet that was a circular cylinder, with equal width and height, k, such that $k/D = 0.01$, 0.02, and 0.04 (an example of a small stud is shown in figure 2.4). For the dynamic tests, only the small stud was used. Though many different roughness geometries could have been used, the basic requirement was that the stud eventually trip the boundary layer. A cylindrical geometry was selected

to remove issues of alignment with the mean flow direction, with consideration of other geometries reserved for future work. In terms of the boundary layer momentum thickness, θ, the stud height in the subcritical case is estimated to fall into the range $0.04 < \theta/k < 0.13$ (with the exact value depending on Re and ϕ_k) for the smallest stud. This estimate was obtained using Thwaite's method (see, e.g., White, 2006) and an experimentally measured velocity profile measured by Fage (1937). The drag contribution of even the largest stud to the total drag is negligible, as its area is about three orders of magnitude smaller than the sphere. Thus, any changes to the forces on the sphere in the presence of the stud are caused by its local alteration of the state of the flow, and not directly by the forces acting on the stud itself.

The motor was powered by two DC power supplies, to allow for both positive and negative voltage to be supplied. The voltage was calculated in Labview (based on the desired trajectory) and output as a low current voltage signal, which was amplified using an op amp (741) in a follower configuration, with the TIP 33C and 34C complementary transistors (see, e.g., Horowitz & Hill, 1989).

In order to reduce the friction of the dynamic stud, a Teflon pad with a diameter of about $0.03D$ was glued onto the bottom of the stud. This reduced friction, combined with the strong neodymium magnets, allowed the stud to move at up to 7Hz (over 3m/s), after which point the magnetic pull was not strong enough to keep it attached to the sphere.

In order to eliminate the effect of frictional forces on the force sensor, the motor was attached directly to the sphere instead of the support structure. Thus, the friction force was canceled by the equal and opposite force on the motor arm. With the motor aligned in this way, the motor had to be precisely balanced (due to centripetal force), which was accomplished by making a symmetric arm, and attaching small weights to the arm until the no flow lateral forces were near zero at the highest rotation rate.

2.3 Actuation Method

In order to obtain precise control of the motor, which controls the position of the roughness element, a linear quadratic regulator (LQR) was implemented. Here the focus is on controlling the position, but a similar approach was also followed to obtain a separate velocity controller. The motor dynamics are given by

$$J\ddot{\theta} = K_t i - b\dot{\theta}, \tag{2.1}$$

where θ is the rotational angle, J is the moment of inertia, K_t is the torque constant, i is the current, and b is the damping constant. This equation is coupled to the applied voltage by

$$V = L\frac{di}{dt} + Ri + K_t\dot{\theta}, \tag{2.2}$$

where L is the motor inductance, $\varepsilon = K_t\dot{\theta}$ is the electromotive force, $R = R_m + R_s$ is the combination of the motor resistance (R_m), and a small resistor placed in series (R_s), which was used to measure the current.

The motor was a hollow core DC motor purchased from MicroMo (part number e_2232 − 012SR). This motor was chosen because it was small enough to fit inside the sphere (22mm in diameter and 41mm long, including shaft), and the hollow-core allowed rapid acceleration, as compared to solid-core motors. The physical constants for the motor, as supplied in the specifications, are $J = 2.42 \times 10^{-5}$Nms^2 (this includes the encoder, and the calculated moment of inertia of the rapid-prototyped arm and magnets), $K_t = 1.6 \times 10^{-2}$Nm/A, $R_m = 4.09\Omega$, and $L = 1.80 \times 10^{-4}$H. The damping constant was estimated using the no-load current and no-load speed, giving $b \approx KI_0\omega_0 = 3.8 \times 10^{-7}$Nms.

In order to calculate the LQR gains, it is convenient to put the equations in state-space form. Using standard notation (see, e.g., Åström & Murray (2008)),

$$\dot{x} = Ax + Bu, \tag{2.3}$$

$$y = Cx + Du, \tag{2.4}$$

where x is the state vector, u is the control input, y is the measured output, and A, B, C, and D are constant matrices. Defining $x_1 = \theta$, $x_2 = \dot{\theta}$, and $x_3 = i$, with measurements $y_1 = \theta$ and $y_2 = i$, combined with the governing equations yields

$$\frac{d}{dt}\begin{pmatrix} \theta \\ \dot{\theta} \\ i \end{pmatrix} = \begin{pmatrix} 0 & 1 & 0 \\ 0 & -b/J & K_t/J \\ 0 & -K_t/L & -R/L \end{pmatrix}\begin{pmatrix} \theta \\ \dot{\theta} \\ i \end{pmatrix} + \begin{pmatrix} 0 \\ 0 \\ 1/L \end{pmatrix} V, \tag{2.5}$$

$$y = \begin{pmatrix} y_1 \\ y_2 \end{pmatrix} = \begin{pmatrix} 1 & 0 & 0 \\ 0 & 0 & 1 \end{pmatrix}\begin{pmatrix} \theta \\ \dot{\theta} \\ i \end{pmatrix}. \tag{2.6}$$

With the voltage as the control input, precise control of θ could only be accomplished if there was no uncertainty in the system. Since this is impossible, feedback is added in order to control the position of the roughness element. Now, define the control input to be dependent on the state of the system and the setpoint, $u = Kx + Mr$. This gives

$$\dot{x} = A_K x + B_K r, \tag{2.7}$$

$$y = C_K x + D_K r, \tag{2.8}$$

where $A_K = A + BK$, $B_K = BM$, $C_K = C + DK$, and $D_K = DM$. The feedforward gain M is found by setting $\dot{x} = 0$ and noting that θ should equal r in steady state. The feedback gain K is found by minimizing the cost function,

$$J \equiv \int_0^\infty [x(t)^T Q x(t) + u(t)^T R u(t)]dt = \int_0^\infty [x(t)^T Q x(t) + u(t)^2]dt, \tag{2.9}$$

subject to (2.3) and $u(t) = Kx(t)$. There is only one input, and hence R can be set to 1 without loss of generality, since the solution is a function only of the ratios of the components of Q to R.

In order to avoid sharp high-amplitude changes in the voltage when there are step changes in the angular frequency, and instead have an optimal transition, a preview controller was also implemented. Instead of just feeding the controller the desired position or velocity, a few hundred milliseconds of the future setpoints is also passed along. This is more easily explained by considering the following suitably defined discrete-time model, where the input is applied with a zero-order hold:

$$\tilde{x}_{j+1} = A_p \tilde{x}_j + B_p u_j, \tag{2.10}$$

$$y_{j+1} = C_p x_j + D_p u_j, \tag{2.11}$$

Now, the state is augmented to include the future N setpoints ($r_i = \theta_{set}(t + j\Delta t)$, $j = 0, \ldots, N$ and Δt is the sample period):

$$\tilde{x} \equiv \begin{pmatrix} \theta \\ \dot{\theta} \\ i \\ r_0 \\ r_1 \\ . \\ . \\ r_N \end{pmatrix}. \tag{2.12}$$

And the equivalent discrete-time system's dynamics matrix $\Phi := e^{A\Delta t}$ is augmented with an $(N+1) \times (N+1)$ matrix, which shifts the setpoint values up by one time step:

$$A_p \equiv \begin{pmatrix} \Phi & 0 \\ 0 & A_r \end{pmatrix}, \tag{2.13}$$

where A_r is the following matrix of compatible dimensions:

$$A_r \equiv \begin{pmatrix} 0 & I_N \\ 0 & 0 \end{pmatrix}. \tag{2.14}$$

Here, u is still the applied voltage, and B_p is obtained by augmenting the discrete-time control matrix by a zero column vector of length $N+1$. The C and D matrices are also padded with zeros so that they are of the appropriate size, because no new states are being measured. Now, set the control input (the voltage) to be dependent on all of the augmented states: $u_j = K_p \tilde{x}_j$. Note that a feedforward matrix M is not needed if the

preview horizon N is sufficiently large.

With the new state space that includes a preview of the upcoming trajectory/velocity, a similar routine is followed to optimize the voltage: a series of gains are found by minimizing the following discrete-time cost:

$$J_p \equiv \sum_{j=0}^{\infty} \tilde{x}_j^T Q_p \tilde{x}_j + u_j^2. \tag{2.15}$$

In order to penalize an error in position, Q_p is given by

$$Q_p = \begin{pmatrix} q & 0 & 0 & -q & & \\ 0 & 0 & 0 & 0 & & \\ 0 & 0 & 0 & 0 & & \\ -q & 0 & 0 & q & & \\ & & & & \ddots & \\ & & & & & 0 \end{pmatrix}, \tag{2.16}$$

that, when multiplied out, just gives $x^T Q_p x = e^T q e$, where $e := \theta - r_0$.

In order to provide reduced noise measurements to the LQR controller, a Kalman filter was implemented to provide an estimate of the state. It was designed by first augmenting the continuous-time system with a constant, unknown, additive disturbance d acting on $\dot{\theta}$, to take account of unmodeled effects such as the damping actually being a function of angular frequency. Defining the augmented state as

$$\bar{x} \equiv \begin{pmatrix} x \\ d \end{pmatrix},$$

and with measured variables

$$y \equiv \begin{pmatrix} \theta \\ i \end{pmatrix},$$

the continuous-time model was converted to an equivalent discrete-time model of the form:

$$\bar{x}_{j+1} = \bar{\Phi}\bar{x}_j + \bar{\Gamma}u_j + \bar{G}w_j,$$
$$y_j = \bar{C}\bar{x}_j + \bar{D}u_j + v_j,$$

where w_j represents process noise and v_j denotes measurement noise. Under the assumption that the covariance matrix of the process noise was the identity matrix, the method described by Rajamani & Rawlings (2009) was applied to some measured data in order to estimate $\hat{G}$ and the covariance matrix of the measurement noise; it was found that a $\hat{G}$ with column rank 2 gave acceptable performance when designing the Kalman filter.

Sampling at 1000Hz and utilizing the preview controller along with the Kalman filter, excellent trajectory control was obtained, and a similar controller provided precise velocity control. The measured system response agreed quite well with a Matlab simulation of the motor and controller.

2.4 Measurement Techniques

The primary tool used to investigate the flow was a three-component piezoelectric force sensor. This allowed for a relatively quick analysis of a large parameter space, after which more detailed, time-consuming methods were used to gain an understanding of the flow physics, such as particle image velocimetry and hot-film anemometry. Other techniques that were used, including dye visualization in a water tunnel, and pitot and hot-wire measurements of the free-stream flow, will not be described in detail.

2.4.1 Time-Resolved Three-Component Force Measurements

The three-component piezoelectric force sensor (Kistler Type 9317B), with dimensions of 2.5 cm $\times$ 2.5 cm $\times$ 3.0 cm, was placed inside the sphere, connecting the sphere and the sting (figure 2.3b) such that the sphere was not in contact with anything other than the force sensor. Each of the three piezoelements was connected to a charge amplifier (Kistler 5010B), which output a voltage to a data acquisition board (National Instrument's PCI-6014 with a board-2120 connector block).

Piezoelectric force sensors have been used in wind tunnel testing extensively by Schewe (see, e.g., Schewe, 1983) in examining the flow over a cylinder. The advantage of the sensor is that it is extremely rigid and has a linear charge-load relationship over several decades. The main disadvantage is that the charge drifts slowly with time, however, this limitation can be overcome with careful use, as described in detail in section 2.5.

2.4.2 Particle Image Velocimetry

Particle image velocimetry (PIV) data was taken with simultaneous force measurements by triggering a LaVision PIV system using a TTL signal from Labview (which was utilized to collect force data). The system consisted of a 30 W Photonics Industries pulsed ND-YLF laser, a high speed Photron Fastcam camera with a 1-megapixel CCD (of which only half was used) and 10-bit depth, and a computer with a precision timing unit. The laser sheet illuminated an aerosol of Bis(2-ethylhexyl) Sebacate particles, which have been found to have a mean diameter of about 1 μm (Raffel *et al.*, 2007), and thus, for the present application, are sufficiently small to accurately follow the flow. Image pairs were recorded at 500 Hz for 4 s, corresponding to a nondimensional time greater than $\hat{t} = tU_\infty/D = 500$ for all of the average vector fields shown in the following chapters, which is long enough to get decent convergence (see chapter 3 and appendix A). For the dynamic stud runs, data was collected for at least 12 stud revolutions.

The accuracy of the LaVision PIV system and the associated DaVis software has been reviewed and compared with other systems (Stanislas *et al.*, 2003, 2005), and is certainly sufficient for our needs.

2.4.3 Hot-film Anemometry

A hot-film was used to examine the boundary layer near the separation point. The sensor was a glue-on type (Dantec Dynamics 55R47), and temporarily placed at $\phi_k = 70^\circ$ using a silicone adhesive. The sensing element was a 0.1mm by 0.9mm thin nickel layer deposited onto a 50 μm thick Kapton foil base. This caused the sensor to protrude part way into the boundary layer, which was estimated to have a momentum thickness of less than 100 μm. The sensor was operated in constant temperature mode using an AA Lab Systems (AN-1005) unit, with an overheat ratio of 1.43, corresponding to a sensor temperature of about 150° C. Fluid movement causes cooling, thus the applied voltage is related to the shear stress and free stream velocity. For our experiments a calibration relating the voltage to the shear stress was not necessary (and would have been difficult given that the probe was not flush with the wall) because our primary interests were determining whether the boundary layer was turbulent (based on the intensity of the fluctuations), and determining the timescales associated with a change to the base flow.

2.5 Data Reduction

2.5.1 Signal Conditioning

The three-component piezoelectric force sensor allowed time-resolved force measurements with a very low rms noise level of about 1mN. However, true static measurements were impossible because the charge on a piezoelement drifts with time due to imperfect electrical insulation. This apparent zero drift can be overcome by limiting the sensor "on" time to the duration of the static measurements, such that any charge drift is not significant or can be corrected using a simple compensation scheme. The static force results were obtained with short duration runs in which the tunnel was at the full operating speed for 15 seconds, and a careful linear interpolation between the zero flow data points was used to estimate the drift. This allowed static measurements with an error of a few millinewton.

Dynamic force data at a given run condition were obtained over an extended period of time (usually $\hat{t} = 1.5 \times 10^5$) and the zero drift was estimated using a combination of the least squares method and cubic splines. Very similar results were obtained using the amplifier's high-pass filter on the uncorrected time signal or an external pass filter during postprocessing. The cubic spline method was chosen due to its simplicity and zero-phase shift. The number of knots used in the cubic spline was found to have a negligible effect on the convergence of the dynamic force statistics. A single polynomial curve was sufficient to estimate the drift for shorter acquisition times.

To isolate the signal from structural vibrations of the support system, a non-causal low-pass Butterworth

filter with a cutoff frequency of 50 Hz was applied to the force signal in both the forward and reverse directions, which doubles the order of the filter and produces a zero-phase shift. The natural frequency of the sphere-support system was approximately 75 Hz, well above the subcritical vortex shedding frequency.

2.5.2 Current Correction

In an ideal motor, all of the electrical energy is converted to rotational energy. Neglecting damping, the torque is proportional to the current. This torque is generated through the Lorentz force: electrons move through the motor coils, which are surrounded by a magnetic field such that $\mathbf{F} = q(\mathbf{E} + \mathbf{v} \times \mathbf{B})$ produces torque. This cross product is very unlikely to produce only a torque, but also a mean force on the motor coils. In most situations this is not a problem because (1) it is only relevant during acceleration, and (2) most of the energy is converted into torque. Because our motor is sitting directly on top of the force sensor, this force is detected, interfering with the desired measurement of the forces caused by fluid motion. However, because the force is directly proportional to the current, it is easy to correct for, given that the applied current is measured: $F_{fluid} = F_{total} - F_{motor}$. The experimentally determined correction factor is given by

$$F_{motor} = i(0.088\hat{x} - 0.0625\hat{y} - 0.0145\hat{z}). \tag{2.17}$$

Comparing with the torque, this indicates that about 6% of the force goes into a mean force, while 94% is converted to torque. Note that this equation is a function of the motor orientation. With this correction, fairly large oscillating currents only increased the sensor noise by a few millinewtons. The correction is applied to the raw data, before any filtering is done.

2.5.3 Analysis Routines

Force and pitot-static data were collected at a sampling frequency of 1 kHz, and the temperature, humidity, and atmospheric pressure were noted for each run. A series of Matlab programs were written to load the data and automatically correct for the drift, filter the signal, nondimensionalize the data, and calculate the statistics, the spectral density and the probability density.

In order to quantify the effect as a function of stud speed, the forces were examined in a stud reference frame such that the $+y$-direction always pointed toward the stud. This allowed the measurement of the phase even when the unsteady force vector loops around the origin.

A particularly important calculation included finding the lateral force and phase difference between the stud and the force vector, for the dynamic stud runs. In this case it is most useful to examine the force with respect to the stud position, so a coordinate transformation was used on the temporal lateral force data such that the new coordinate system rotated with the stud (with the $+y$-direction pointing at the stud). Then, the mean C_y and C_z (in the stud frame, based on many rotations) were found and converted to the mean C_L and θ. An alternative method would be to calculate C_L and θ at each time step, and then average at the end.

However, this gives incorrect results because for a stationary stud the fluctuating force takes on all angles, which would yield a mean lag of 180° instead of zero.

2.6 Error Analysis

The linearity of the force sensor, as measured by the manufacturer, is $\leq \pm 44$ mN over the calibration range of $0-10$ N for the three force components. The actual linearity is likely much better, as it is difficult to calibrate the sensors down to small loads due to the charge drift. To verify the calibration, small weights were placed on the sensor and the method described above was used to correct for zero drift. The results reported here are similar to those found by Schewe (1982), who assumed that the sensor was linear over several decades. The cross talk between components is $\leq \pm 2.2\%$, as measured by the manufacturer.

Zero-flow measurements of the noise floor on each component of the force sensor revealed a standard deviation of $\sigma_x = 1.7$ mN in the drag direction and lower standard deviations of about $\sigma_y = \sigma_z = 0.5$ mN in the lateral components. The noise was for the most part between 2 to 6 orders of magnitude lower than the amplitude of the measured data, depending on *Re* and the force component being examined.

Despite considerable care in the experimental setup, the (well-known) sensitivity of sphere flow to the input boundary conditions was observed during these experiments. The mean force variation and especially the critical *Re* are greatly affected by surface roughness, free stream turbulence, tunnel blockage, and method of support, as has been systematically demonstrated by others (see, e.g., Bacon & Reid, 1924; Hoerner, 1935; Achenbach, 1974*a*). In this study, rotation of the sphere or relocation with respect to the center of the test section led to small but noticeable changes to the mean forces. However, for a given configuration the results were repeatable, and changes caused by boundary conditions were minimal compared with purposely imposed changes caused by, e.g. placing a small roughness element on the sphere, with a diameter of only 1% the sphere diameter (see chapter 4). In other words, the nature of the flow leads to a large bias error, which is setup dependent, while the uncertainties in our measurements result in comparably small random error.

The most important factor governing the error in calculating the Reynolds number was uncertainty in temperature. Though the temperature was controlled, there could still be a slow drift, usually 1K at most. An error of 3K corresponds to a Reynolds number uncertainty of 2%, which is likely an upper bound since the effects of errors in humidity and atmospheric pressure are much smaller. In addition, the uncertainty in the pitot-static measurement leading to a measurement of velocity was comparably negligible.

Chapter 3

Forces on a Smooth Sphere

3.1 Overview

A three-component piezoelectric force sensor was used to verify the presence of low frequency energetic forcing on a smooth sphere, and provide guidance as to how long the flow needs to be examined to provide converged statistics. It is argued that the low frequency forcing and modulation of the wake is caused by local variation of the separation location, and that this needs to be taken into account in any attempts to model the flow. In addition, a simple model is proposed which captures much of the energetic behavior of the wake.

3.2 Fluctuating Forces

The variation of the mean drag force observed over a range of Reynolds numbers is shown in figure 3.1, and can be seen to be in good agreement with the classical results of Achenbach (1974*a*). The critical Reynolds number, defined by Achenbach to indicate the onset of the drag crisis, falls between that of Achenbach's smooth ($k/D \approx 0$) and slightly rough ($k/D = 2.5 \times 10^{-4}$) sphere results, in good agreement with our earlier estimate of $k/D = 1 \times 10^{-4}$. The subcritical, critical and supercritical regimes can be clearly distinguished.

Figure 3.2 shows a time history of the lateral forces, i.e., a phase diagram for C_y and C_z, for both subcritical and supercritical *Re*. The subcritical force history has a strong oscillatory component, which will be shown to be associated with vortex shedding, and is qualitatively similar to the simulation of Yun *et al.* (2006). In the supercritical case, the phase of the force appears to be significantly more random, with a noticeable bias to a nonzero mean for this time record. Note that the maximum *St* that could be resolved for the supercritical case was about 0.2 because the dimensionless natural frequency of the mount structure decreased with increasing *Re*. At these Reynolds numbers, therefore, the force history was effectively low-pass filtered, such that higher frequency oscillations and/or supercritical vortex shedding were not recorded. If there is significant energy at higher frequencies, this will affect the supercritical standard deviation estimates that are presented later.

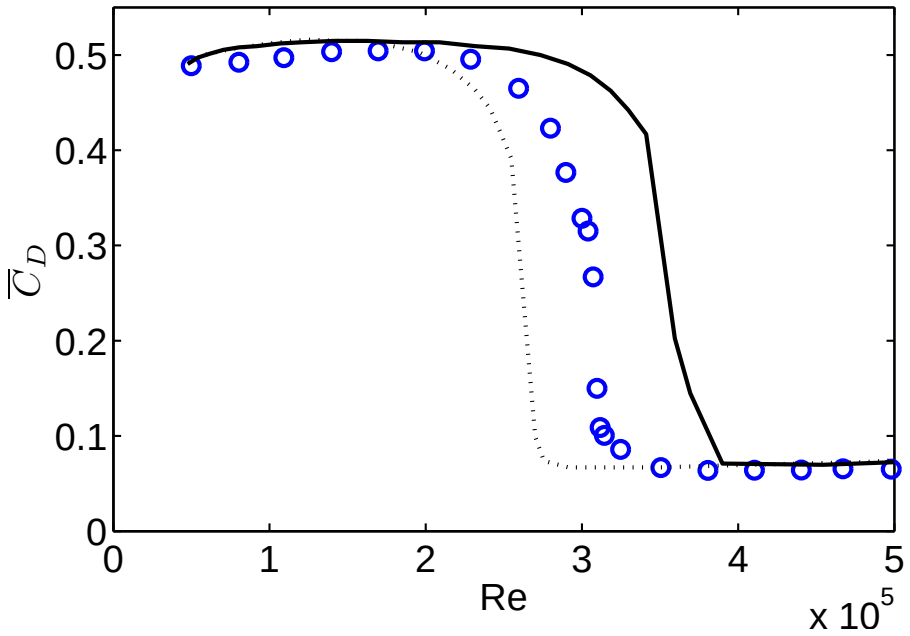

Figure 3.1: Variation of the coefficient of mean drag with Reynolds number: present data (o) compared with the results of Achenbach for a smooth (−) and slightly rough sphere ($k/D = 2.5 \times 10^{-4}$, ····).

3.3 Statistical Convergence

In order to verify statistical convergence of the dynamic force data, and to allow us to address the open question concerning observations of a nonzero mean lateral force at supercritical Reynolds numbers, the time variation of the force statistics were examined for both subcritical (figure 3.3) and supercritical (figure 3.4) Reynolds numbers. Long dynamic data records were taken at each Re ($\hat{t} = 1.5 \times 10^5$), such that each data set could be split into 75 subsets of length N (each assumed to be independent). The running mean (μ), standard deviation (σ), skewness (s), and kurtosis (k) were then calculated for all force components (i-subscript) and for each subset (j-superscript), as a function of the time step t_n ($1 < n < N$):

$$\mu_i^j(t_n) = \frac{1}{n}\Sigma_{p=1}^{n} C_i^j(t_p), \tag{3.1}$$

$$\sigma_i^j(t_n) = \sqrt{\frac{1}{n}\Sigma_{p=1}^{n}(C_i^j(t_p) - \mu_i^j(t_n))^2}, \tag{3.2}$$

$$s_i^j(t_n) = \frac{1}{n}\Sigma_{p=1}^{n}(C_i^j(t_p) - \mu_i^j(t_n))^3/\sigma_i^j(t_n)^3, \tag{3.3}$$

$$k_i^j(t_n) = \frac{1}{n}\Sigma_{1=p}^{n}(C_i^j(t_p) - \mu_i^j(t_n))^4/\sigma_i^j(t_n)^4. \tag{3.4}$$

The final statistics were then formed by taking the running standard deviation of the 75 subsets.

$$convergence(m_i(t_n)) = \sqrt{\frac{1}{75}\Sigma_{j=1}^{75}(m_i^j(t_n) - m_i(t_n))^2}, \tag{3.5}$$

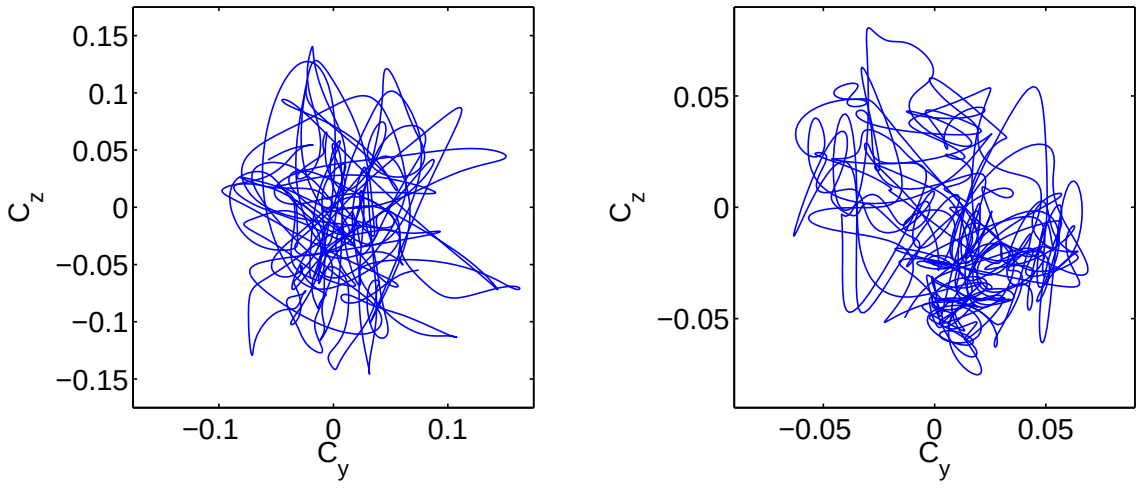

Figure 3.2: Time trace of the lateral forces for (a) subcritical $Re = 1.1 \times 10^5$ with $\Delta\hat{t} = 250$ and (b) supercritical $Re = 4.1 \times 10^5$ with $\Delta\hat{t} = 800$.

where m represents one of the four statistics being examined, and m_i is the expected value of the statistic based on all of the subsets, $m_i(t_n) = \frac{1}{75}\Sigma_{j=1}^{75} m_i^j(t_n)$.

Examining the convergence of the mean in figures 3.3a and 3.4a, the limit as $n \rightarrow 1$ should be equal to the standard deviation of the forces, given enough subsets of data. Using 75 subsets, this limit is approximately held. Note that there is very little measurement noise (see section 3.5), so the convergence rate is dependent on the unsteady forces caused by the flow. After the relatively long sample time of $\hat{t} = 500$, the calculated mean value of all three force components is within 0.01 of the true mean, which would be barely noticeable on mean force plots.

Accurately estimating the standard deviation takes more time, as can be seen in figures 3.3b and 3.4b. After a $\hat{t}$ of 1000, σ for the lower Re will be within (on average) about 5% of the actual value for the lateral forces, and for the higher Re within about 8%. The convergence of the supercritical drag compared with its actual standard deviation is somewhat slower.

The convergence of the skewness and kurtosis of the probability distribution are also shown in figures 3.3 and 3.4. Of particular note is that the drag kurtosis converges more slowly than those of the lateral forces. By a $\hat{t}$ of $2,000$, the mean error in skewness and kurtosis is still quite large compared with our estimate based on the full data set (figure 3.5). In addition, the convergence statistics are still rapidly converging toward zero, indicating that more time would be needed to accurately estimate these higher-order statistics.

The slow convergence of all measures of the mean and fluctuating forces represents a challenge for simulations of sphere flows, and may contribute to the apparent supercritical mean lateral force observed in the literature. The results presented in the next section are based on data records with length $\hat{t}$ of 1.5×10^5 and thus represent fully converged results. This is also evident by noting the small scatter of the data in the sub-

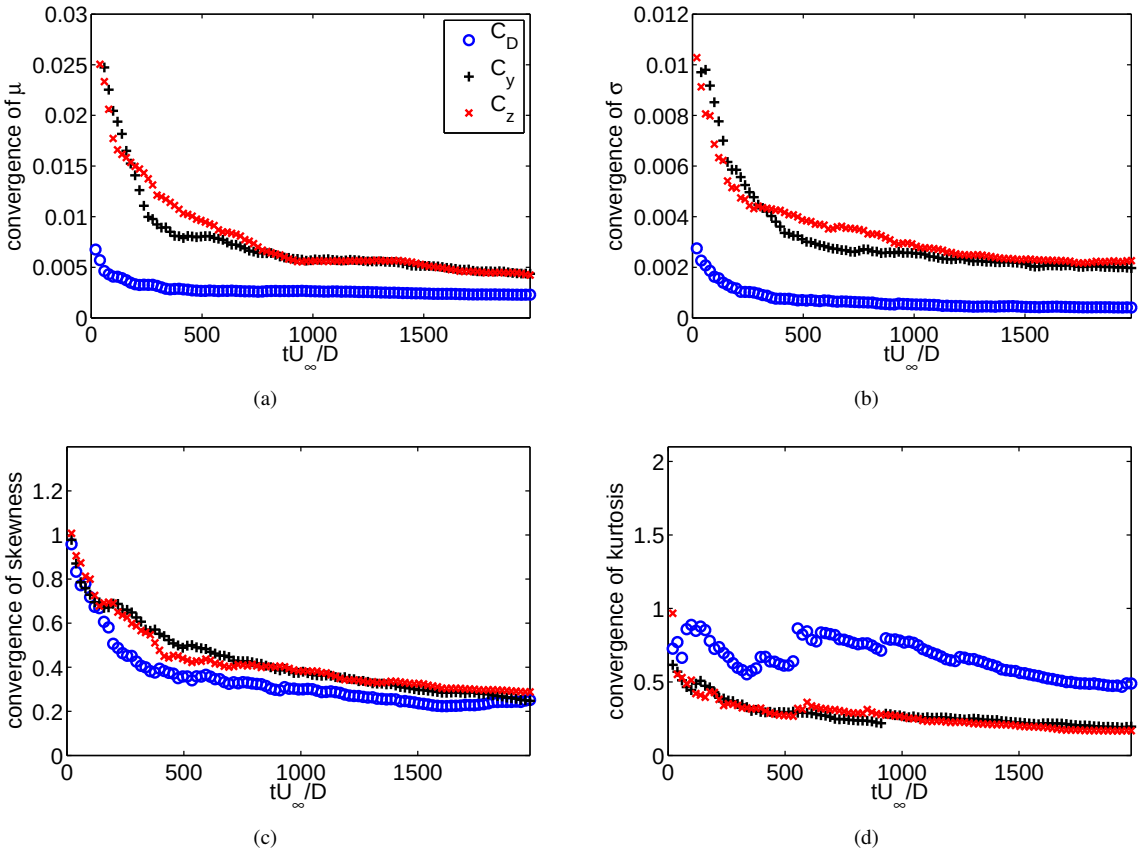

Figure 3.3: Statistical convergence of dynamic force data: standard deviation of the moments as a function of averaging time, subcritical $Re = 1.1 \times 10^5$,

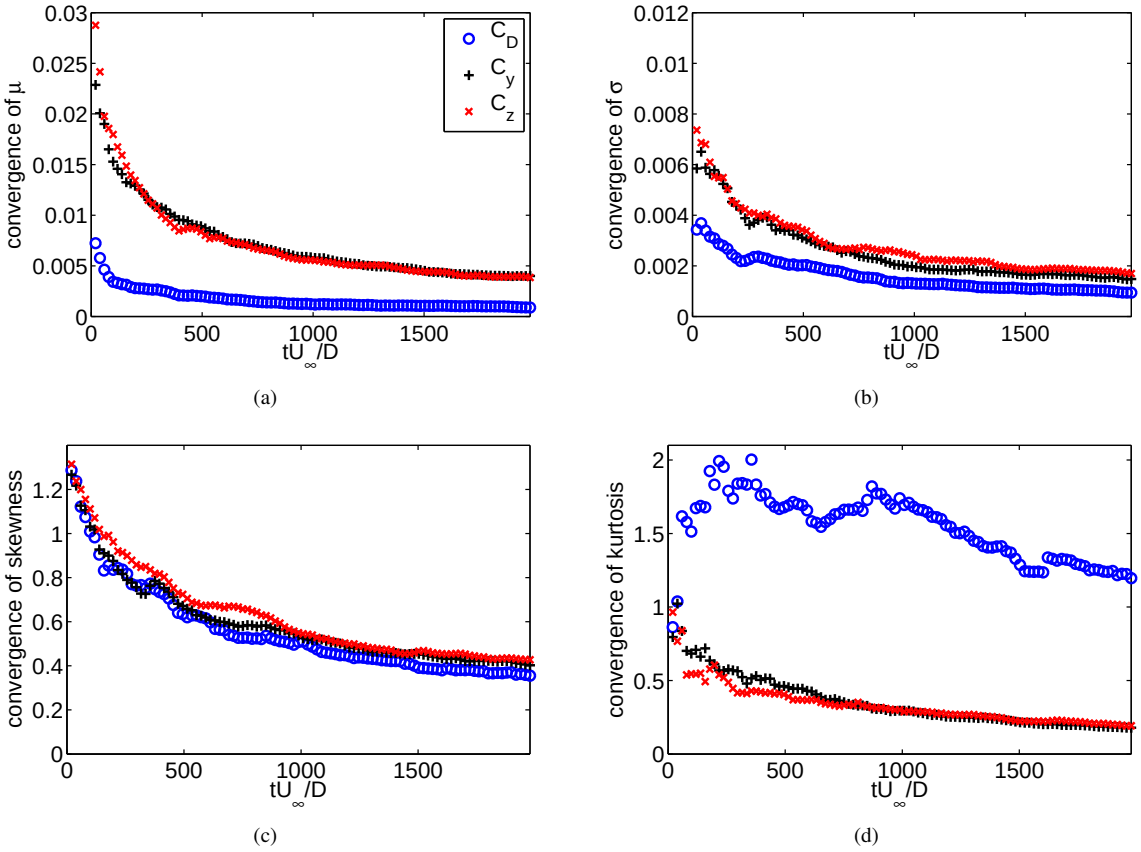

Figure 3.4: As figure 3.3, supercritical $Re = 4.1 \times 10^5$.

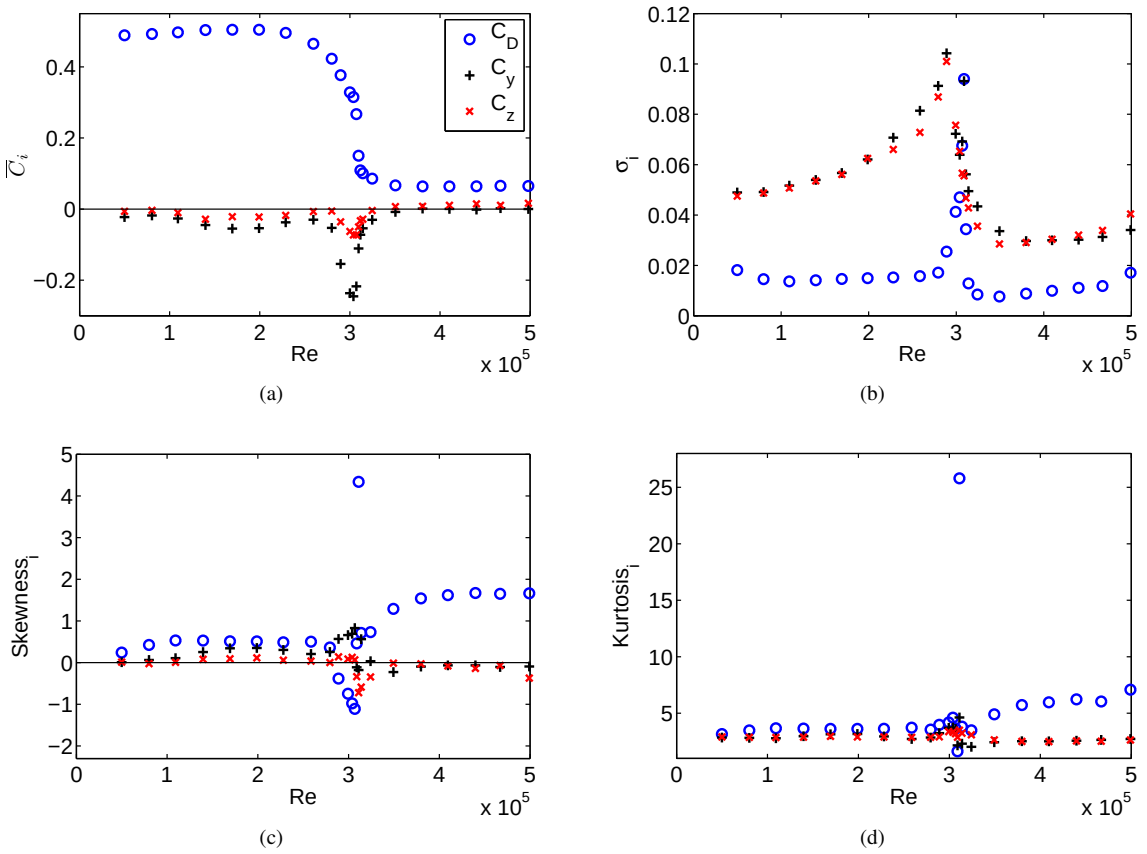

Figure 3.5: Statistical summary of the force coefficients, C_i,: (a) mean (b) standard deviation (c) skewness and (d) kurtosis.

critical and supercritical regimes, where it is well known that the flow undergoes only gradual change as a function of *Re*.

3.4 Mean Force and Higher Moments

Figure 3.5a shows the Reynolds number variation of the mean values of all three force components, $\overline{C_i}$. The mean lateral force is close to zero in both subcritical and supercritical regimes (figure 3.5a), in apparent contradiction to earlier results suggesting a mean side force (Taneda, 1978; Constantinescu & Squires, 2004). Of more interest, in the critical regime both C_y and C_z take large nonzero values, indicating that a large mean lateral force develops as the Reynolds number increases through the critical value. If the sphere is rotated, the angle corresponding to the mean lateral force rotates accordingly, indicating that the flow in the critical regime is controlled by imperfections on the sphere (asymmetric roughness and/or shape), even though the sphere was designed with precision in mind. A mean lateral force in the critical regime has also been observed in cylinder flow by Schewe (1983), although in that study the direction of the mean force varied from run to

run.

The second moment of each force component is shown in figure 3.5b. For most of the Reynolds number range investigated the variance of drag is approximately a factor of three smaller than the variance of the lateral forces, which are in good agreement as would be expected for a nominally axisymmetric flow. Force histories in the critical regime at $Re = 3.09 \times 10^5$ reveal an intermittent drag signal, alternating between the subcritical and supercritical values (manifest as the bimodal probability density 4 shown in figure 3.6, described in detail later) and giving rise to the large variance observed over the narrow critical Reynolds number band. Interestingly, there is little appreciable difference in the variance of the drag from sub to supercritical Reynolds numbers, despite the inferred difference in wake structure (see section 3.5).

The second moments of the lateral forces, σ_y and σ_z increase rapidly with increasing Reynolds number to a maximum in the critical regime at a Reynolds number slightly below the value at which a maximum was observed in σ_x. An approximately constant, lower value of $\sigma_{y,z} \approx 0.04$ is observed for supercritical *Re*. This value is in reasonable agreement with the root-mean-square lateral force (which is equivalent to the standard deviation only if the mean lateral force is zero) of approximately 0.06 reported by Willmarth & Enlow (1969) for $5 \times 10^5 < Re < 1.8 \times 10^6$, considering that they examined a rough sphere with a smaller ratio of sting to sphere diameter.

Despite small differences between the standard deviation of the streamwise and lateral forces, all components reach a minimum at around $Re = 3.5 \times 10^5$, at which *Re* the mean forces have taken their supercritical values.

Figures 3.5c and 3.5d show that the skewness and kurtosis of all three force components are approximately 0 and 3, respectively, indicative of a Gaussian distribution in the subcritical regime. In the supercritical regime the lateral forces take similar values, but the supercritical drag has a large skew and kurtosis, reflecting a different wake structure, in particular with respect to vortex shedding (see section 3.5). In the critical regime, the skewness and kurtosis deviate from Gaussian, and the exact values are likely dependent on the minute imperfections associated with the sphere (section 2.2.3). The extreme values of skewness and kurtosis near $Re = 3.0 \times 10^5$ are associated with the intermittency of the drag history as the wake alternates between the subcritical and supercritical states. It is worth repeating that the limitation of the natural frequency of the sting system at supercritical Reynolds numbers constrains our results to lower bounds on the true moments if there is significant forcing above about $St = 0.2$.

The probability density functions (pdfs) for several representative *Re* (normalized such that the total area under the curve equals one) shown in Figure 3.6 summarize these results. Here only the drag force is examined because it exhibits the widest variation in pdf form. The pdfs for subcritical *Re* (1-2) are essentially Gaussian, while the supercritical state (6) is highly skewed around $C_D \approx 0.06$, with occasional deviations to higher drag. The pdf in the critical regime (4) is bimodal, leading to the large values of skew, kurtosis, and standard deviation discussed above. Lines 3 and 5 correspond to the minima and maxima in skewness and kurtosis, respectively, indicating that the corresponding Reynolds numbers approximately bound the

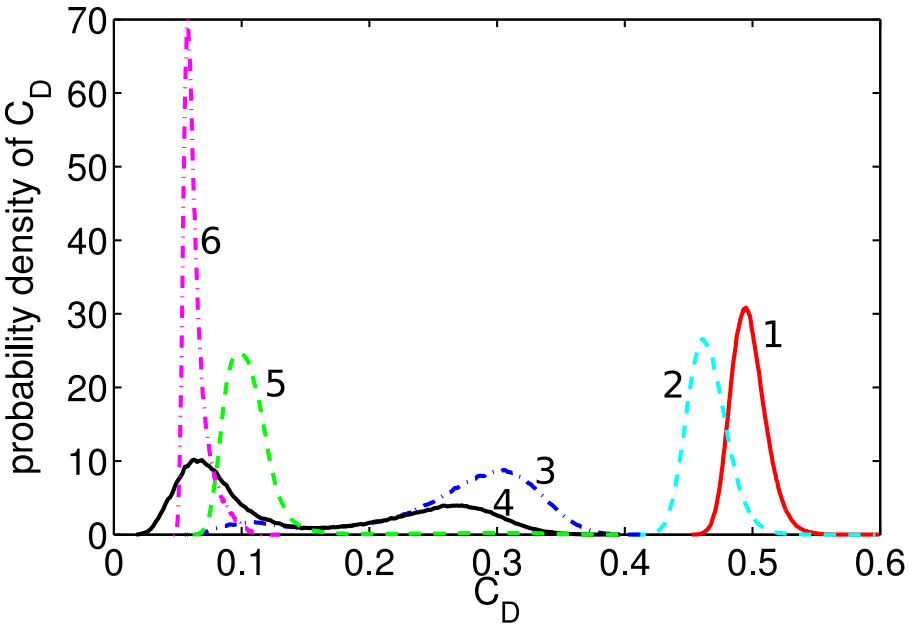

Figure 3.6: Probability density for: subcritical Reynolds numbers (1) 1.1×10^5, (2) 2.6×10^5; critical *Re* (3) 3.07×10^5, (4) 3.09×10^5, (5) 3.11×10^5; and supercritical *Re* (6) 4.1×10^5.

beginning and end of the regime in which the drag force switches intermittently between sub and supercritical values. However, small variations in the Reynolds number ($\sigma(Re) = 800$ based on hot-wire measurements) do not allow for precise conclusions about the sharpness of the change. The pdf at the intermediate Reynolds number (line 4) shows that the drag is approximately evenly distributed between the two states, leading to smaller values of skew and kurtosis, but a maximum in standard deviation.

3.5 Force Spectral Density

The dimensionless spectral density of the forces, $\Phi_i(St)$, obtained in these experiments are presented for a range of representative *Re* in figures 3.7 through 3.10, where the i subscript represents one of the force components. Data at specific *Re* and *St* ranges reported in the literature are also plotted, where applicable. Each spectral component was calculated using Welch's method (Welch, 1967) and was normalized such that the total area under the spectrum was equal to the mean squared force fluctuations:

$$\overline{C_i'^2} = \int_0^\infty \Phi_i(St) d(St). \tag{3.6}$$

The present lateral force spectra at subcritical *Re* in figure 3.7 show a gradual reduction in the energy associated with vortex shedding (at $St = 0.2$) as the critical regime is approached, accompanied by an increase in energy at lower frequencies. The peak associated with vortex shedding is no longer detected by $Re \approx 2.7 \times 10^5$ (not shown).

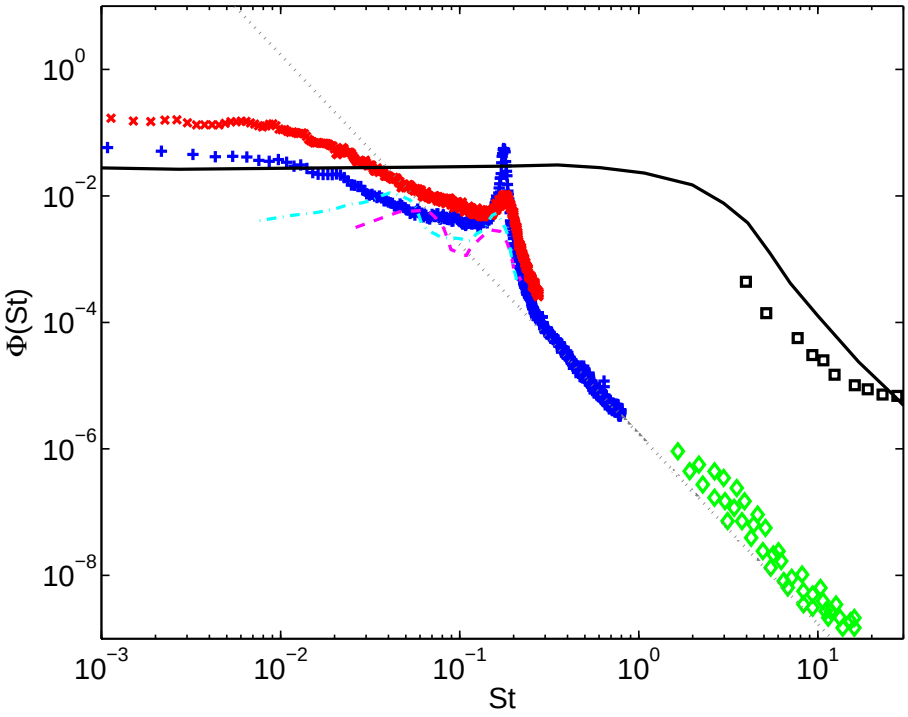

Figure 3.7: Normalized power spectral density of the subcritical lateral forces, compared with the literature. The lateral force spectra were averaged. Present results, $Re = 8 \times 10^4$ (+) and $Re = 2.3 \times 10^5$ (x); Constantinescu & Squires (2004) (−−), $Re = 10^4$; Yun *et al.* (2006) (−.−), $Re = 10^4$; Howe *et al.* (2001) model (–); Howe experiments (□), $7 \times 10^3 < Re < 1.7 \times 10^4$; Lauchle & Jones (1998) (◊), $7 \times 10^3 < Re < 3.5 \times 10^4$; St^{-3} (...).

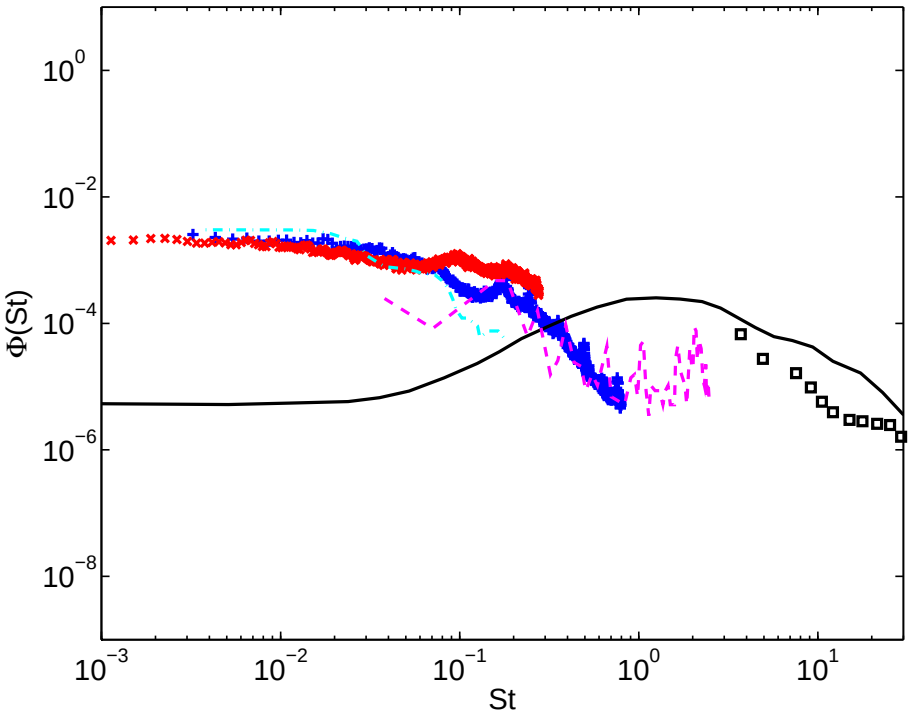

Figure 3.8: Normalized power spectral density of subcritical drag force, compared with the literature. Symbols as in figure 3.7.

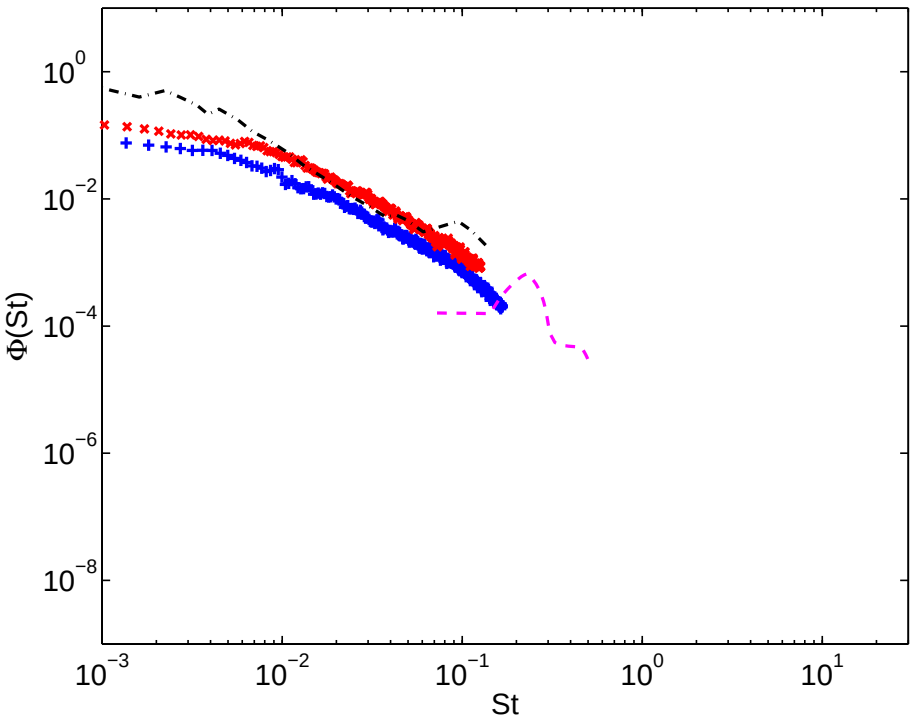

Figure 3.9: Normalized power spectral density of supercritical lateral force, compared with the literature. $Re = 3.8 \times 10^5$ (+); $Re = 5.0 \times 10^5$ (x); Willmarth & Enlow (1969) (−.−), $4.8 \times 10^5 < Re < 1.7 \times 10^6$; Constantinescu & Squires (2004) (−−), $Re = 1.1 \times 10^6$.

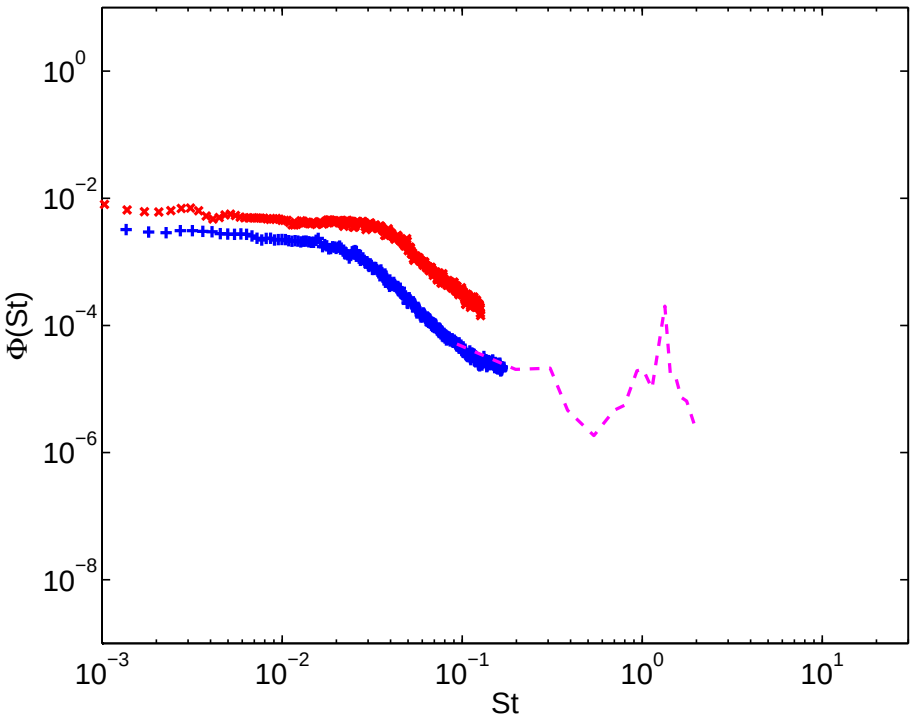

Figure 3.10: Normalized power spectral density of supercritical drag force, compared with the literature. Symbols as in figure 3.9.

This figure also shows results averaged over the two lateral force components from the DES of Constantinescu & Squires (2004) and the LES of Yun *et al.* (2006) for a subcritical Re of 10^4. Both confirm the peak near the vortex shedding frequency and also a lower frequency peak, with a lower mean squared lift. The model of Howe, Lauchle & Wang (2001), with a tilt of 10° to vortex rings being shed randomly from the sphere, leads to significantly larger force amplitudes at high St and a corresponding higher mean squared lift coefficient. The primary goal of the model was to simulate the high St decay rate of the spectrum, proportional to St^{-3}, which is in good agreement with the experimental data of Howe *et al.* (2001), with $7\times10^3 < Re < 1.7\times10^4$. However the power is four orders of magnitude larger than the present data. The model assumption of inviscid flow, namely a superposition of an array of vortices superimposed on potential flow, and matching of the drag coefficient to experimentally measured values likely leads to an overestimation of the vortex circulation to compensate for the contribution of the separated region to the drag, consequently leading to a higher value of mean squared lift relative to our data and the absence of a peak at the shedding frequency. However the earlier experimental results of Lauchle & Jones (1998) (subsequently suggested to have been an underestimate due to the sphere support mechanism) with $7\times10^3 < Re < 3.5\times10^4$ are in good agreement with the trend suggested by our data.

A low peak corresponding to the vortex shedding frequency is observed in the subcritical drag spectrum of figure 3.8 at low Re, though it is not nearly as prominent as it is for the lateral force, and it mostly disappears by $Re = 2.3\times10^5$. Once more, agreement with the simulations results is reasonable while there is significant

disagreement with the model of Howe *et al.* (2001).

The force spectra for supercritical *Re* in figures 3.9 and 3.10 do not exhibit a peak near the subcritical vortex shedding frequency (the measured frequency range shown barely reached $St = 0.2$, though lower supercritical *Re* data reaches $St = 0.24$ and also shows nothing). The lateral force data are in fairly good agreement with the results of Willmarth & Enlow (1969) for a rough sphere in the range $4.8 \times 10^5 < Re < 1.7 \times 10^6$. The simulations of Constantinescu *et al.* for a fully turbulent sphere boundary layer ($Re = 1.1 \times 10^6$) suggest that a noticeable but low amplitude peak might be observed close to $St = 0.2$ at higher *Re* than examined in this study, while the peak near $St = 1.3$ (figure 3.10) that those authors correlated with the shedding of hairpinlike structures was beyond the frequency range of our measurements.

3.6 Synchronous Velocity Field and Force Histories

In an effort to correlate the temporal force history with the structure of the wake, force measurements along with simultaneous high speed PIV of the near-wake (x-y plane) were examined over many vortex shedding cycles. Figure 3.11 shows a sample time trace of all three force components, and PIV images at instants corresponding to positive, near zero, and negative lateral forces in the direction that corresponds to the plane of the image (C_y). The PIV images show the clear imprint of the roll-up of the shear layer and a large scale oscillation. Reflection and resolution issues prevent any conclusions being drawn about the instantaneous location of separation. Examining the full time series, on average the recirculation region is smaller when the force is positive, and larger when it is negative. However, when the force is near zero, it is difficult to tell what the force should be just by looking at the velocity field. This is due to the flow being highly three-dimensional: there is a large azimuthal variation in the pressure distribution and the condition of the shear layer (Taneda, 1978; Yun *et al.*, 2006), and the force vector is rarely aligned in the x-y plane. Note though, that some of these issues can be overcome by imposing a deterministic perturbation to the flow, such as a discrete static or dynamic surface roughness element, as will be shown in chapters 4 and 5. A better correlation between the flow and the force would likely be obtained by comparing the velocity adjacent to the separation point to the forces, which Willmarth & Enlow (1969) found to have up to an 80% correlation in the supercritical regime, using hot wire anemometry.

3.7 A Simple Force Model

As shown in the previous sections, the side forces exerted on a sphere when fluid flows over it in the subcritical Reynolds number range appears to be mostly random with a dominant frequency component associated with vortex shedding. The lateral force history shown in figure 3.2a is reminiscent of the trajectory of a double spring system with some random forcing, which led to the following model.

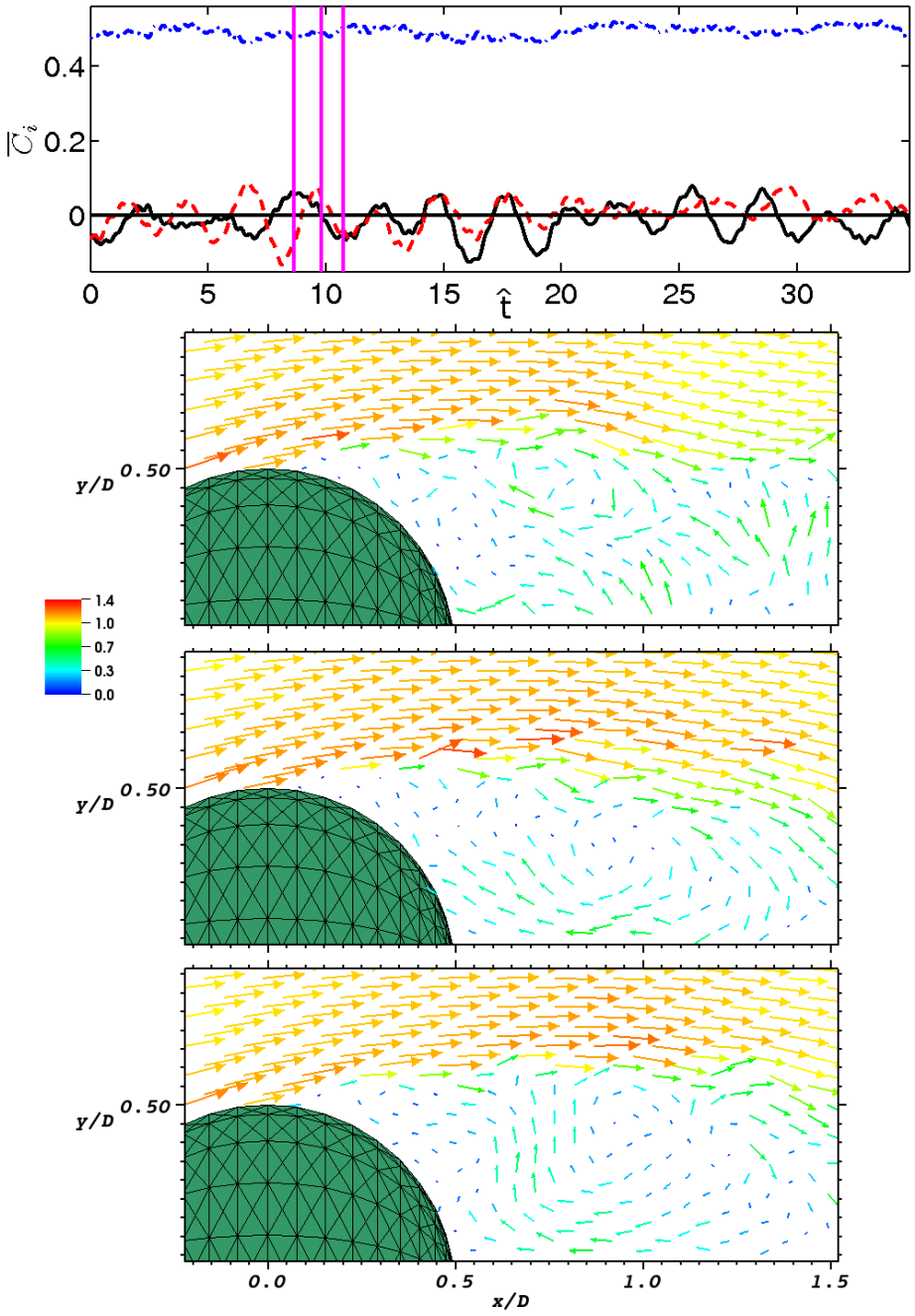

Figure 3.11: Simultaneous PIV and force data for C_y: (a) positive (b) zero and (c) negative. C_x (-··-); C_y (–); C_z (- -).

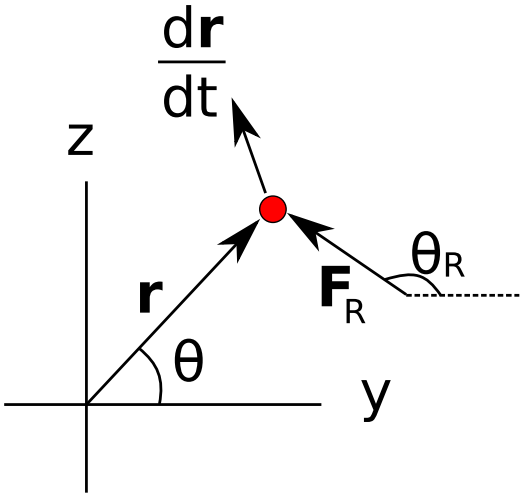

Figure 3.12: Schematic of a two-dimensional harmonic oscillator, with the restoring force being proportional to the distance from the origin.

The equations for a two-dimensional oscillator with a forcing and damping term are

$$\ddot{\mathbf{r}} + \frac{d}{m}\dot{\mathbf{r}} + \frac{k}{m}\mathbf{r} = \frac{\mathbf{F_R}(t)}{m}, \tag{3.7}$$

where m is the particle mass, d is the damping constant, k is the spring constant, $\mathbf{r} = \begin{pmatrix} y \\ z \end{pmatrix}$ is the position vector, and $\mathbf{F_R}(t)$ is a random forcing (figure 3.12). A random forcing is chosen since the probability density function (pdf) of the side forces is Gaussian. Assume that the applied force is constant, but that the direction of application changes with time. Define this direction in the y-z plane to be θ_R. Now, assume that θ_R gradually changes with time.

$$\theta_R(t_{n+1}) = \theta_R(t_n) + \theta_{step}G, \tag{3.8}$$

where θ_{step} is a constant and G is a random variable chosen from the unit Gaussian distribution. This leads to the equations

$$\begin{aligned} \ddot{y} + \frac{d}{m}\dot{y} + \frac{k}{m}y &= \frac{F_R}{m}cos(\theta_R(t)), \\ \ddot{z} + \frac{d}{m}\dot{z} + \frac{k}{m}z &= \frac{F_R}{m}sin(\theta_R(t)). \end{aligned} \tag{3.9}$$

These equations produce a particle motion similar to the forces on the sphere. Making a change of variables: $y \longrightarrow F_y$ and $z \longrightarrow F_z$ yields for the y-direction (and similarly for the z-direction),

$$\ddot{F}_y + \frac{d}{m}\dot{F}_y + \frac{k}{m}F_y = \frac{a}{m}cos(\theta_R(t)), \tag{3.10}$$

where $F_R \longrightarrow a$ because the units of the constant (and hence the physical interpretation) have changed.

The equations can be made dimensionless using the free stream velocity (U_∞), sphere diameter (D) and fluid density (ρ): $\hat{t} = \frac{tU_\infty}{D}$ and $C_y = \frac{F_y}{\frac{1}{2}\rho U_\infty^2(\pi\frac{D^2}{4})}$. This yields

$$\frac{d^2C_y}{d\hat{t}^2} + \frac{d/m}{U_\infty/D}\frac{dC_y}{d\hat{t}} + \frac{k/m}{U_\infty^2/D^2}C_y = \frac{a/m}{\frac{\pi}{8}\rho U_\infty^4}cos(\theta_R(\hat{t})). \tag{3.11}$$

For a lightly damped system, $\frac{k}{m} \simeq (2\pi f)^2$, where f is the frequency of oscillation. Inserting the dimensionless frequency, or Strouhal number ($St = \frac{fD}{U}$), and defining the constants $\zeta \equiv \frac{d}{m}$ and $\alpha = \frac{a/m}{\frac{\pi}{8}}$ gives

$$\frac{d^2C_x}{d\hat{t}^2} + \frac{\zeta}{U_\infty/D}\frac{dC_x}{d\hat{t}} + (2\pi St)^2C_x = \frac{\alpha}{\rho U_\infty^4}cos(\theta(\hat{t})). \tag{3.12}$$

Defining $\delta \equiv \frac{\zeta}{U_\infty/D}$ and $\beta = \frac{\alpha}{\rho U_\infty^4}$, yields the two equations:

$$\begin{aligned} \frac{d^2C_y}{d\hat{t}^2} + \delta\frac{dC_y}{d\hat{t}} + (2\pi St)^2C_y &= \beta cos(\theta_R(\hat{t})), \\ \frac{d^2C_z}{d\hat{t}^2} + \delta\frac{dC_z}{d\hat{t}} + (2\pi St)^2C_z &= \beta sin(\theta_R(\hat{t})). \end{aligned} \tag{3.13}$$

This leaves five adjustable constants: δ, St, β, θ_{step}, and the time step $\Delta\hat{t}$ between $\theta_n(\hat{t})$ and $\theta_{n+1}(\hat{t})$. The Strouhal number effects the location of the vortex shedding peak, and β changes the width of the pdf, so it can easily be set to achieve the experimentally determined standard deviation.

Comparing to the two-dimensional harmonic oscillator analogy, the net effect of the random forcing term is to add energy to the system. This energy addition must be balanced by energy loss, which is produced by the damping term. Hence, δ keeps the force coefficient finite. Thus, three adjustable parameters are left that need to be adjusted to achieve an optimal model.

For $\Delta\hat{t} = 0.001$, good agreement with the data is obtained by setting $\delta = 0.069$, $St = 0.173$, $\beta = 0.0546$, and $\theta_{step} = 0.0158$. Figure 3.13 shows a comparison between the model and data pdf, and figure 3.14 a comparison of the power spectrum. Varying both θ_{step} and δ produces a better agreement with either the power spectrum or with the probability distribution, but not both at the same time. The cited constants are a compromise. With these values, the standard deviation of the change of θ_R per vortex cycle is about 70°.

In figure 3.15 a time trace of one of the lateral force components is compared with the experimental measurements and the literature, where the width of the line indicates the uncertainty in reproducing the data. The model appears qualitatively similar to the measured data and the numerical simulations. On the other hand, the results are quite different than the potential flow model of Howe, which is to be expected based on the spectral density plots discussed earlier. An interesting result is that the forcing is quite distinct from that of a cylinder, which has much higher forcing amplitude, without significant low-frequency motion.

A model with so many adjustable parameters may possibly be useful for some sort of control approach, but from a theoretical standpoint it needs to be developed much further. Here a physical interpretation of the

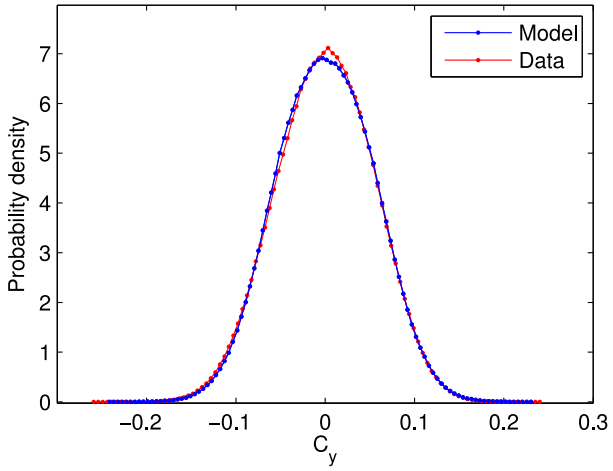

Figure 3.13: Probability density function of the side force, C_y, compared with measurements at $Re = 1 \times 10^5$.

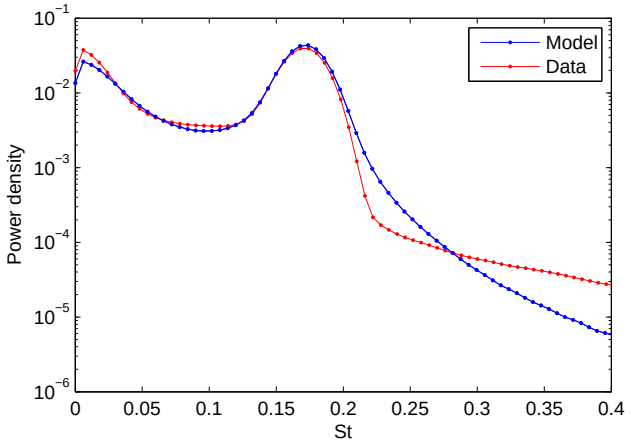

Figure 3.14: Power spectral density of the side force, C_y, compared with measurements at $Re = 1 \times 10^5$.

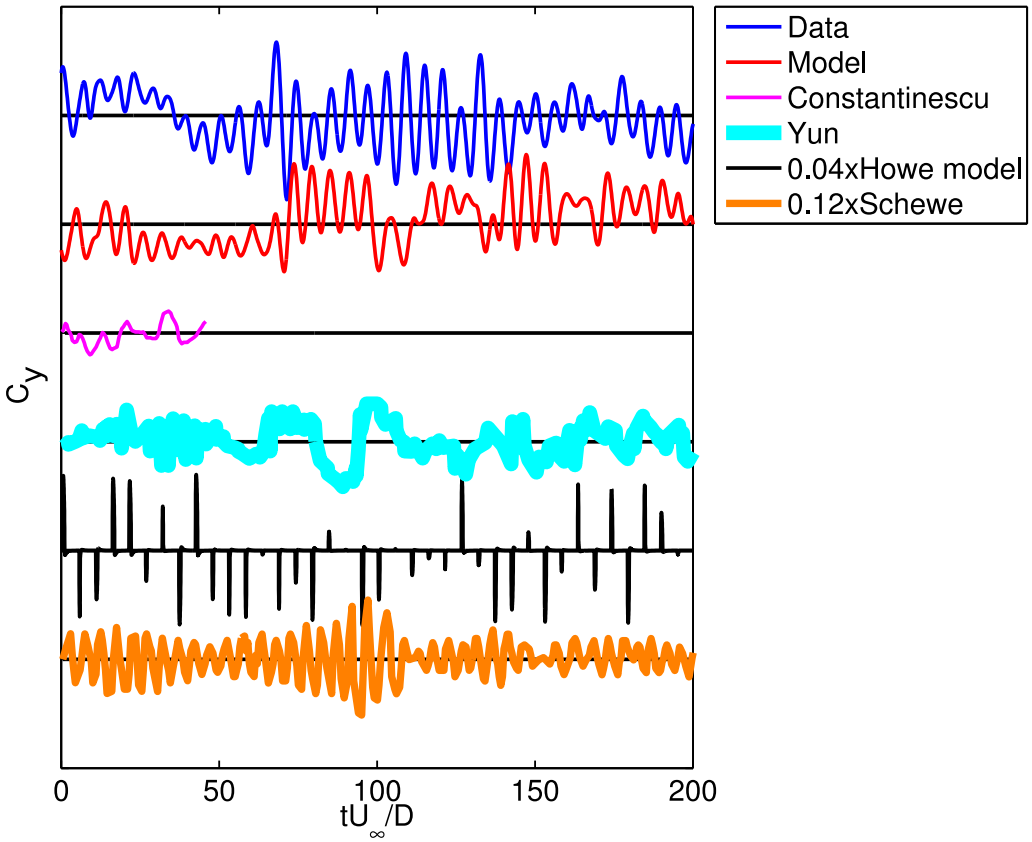

Figure 3.15: Comparison of model results and measured data and the literature.

model is presented, which may prove useful in improving it.

Consider the instantaneous near wake with positive circulation in a control volume surrounding the near wake, such that the wake is tilted down. The tilt produces a higher maximum fluid velocity on the top of the sphere. This enhances entrainment, and leads to higher vorticity addition in the top shear layer than on the bottom. Hence, a physical argument for the restoring force is that when $\Gamma > 0$ in the near wake, $\frac{d\Gamma}{dt} < 0$ and vice versa.

The random forcing comes into play when considering the local dynamics of the separation point. As is shown later in chapter 5, a dynamic stud introduces a disturbance into the boundary layer, which then alters the separation point and the rate of entrainment in the shear layer. The timescale associated with the disturbance is $\hat{t} \approx 4$ until the change in force due to the disturbance amplification reaches a maximum, which is similar to the period of vortex shedding. For the case of the smooth sphere, it is proposed that disturbances from the free stream interact with the boundary layer, and after amplification alter the forces based on the nonlinear dynamics of the flow separation. The proposed model takes into account the random forcing, though the details could be improved by, for example, allowing the magnitude of the random force to vary.

3.8 Discussion and Summary

3.8.1 Structure of the Sphere Wake

This study has corroborated and extended the findings in numerical simulations that there is significant low frequency forcing on the sphere in the subcritical Reynolds number regime. It was discovered that at low Reynolds numbers, the spectral energy is split nearly evenly between low frequencies and the vortex shedding frequency, but as the critical regime is approached, the energy is transferred solely to the low frequencies. A likely explanation for these observations is that the low frequency forcing is caused by the long timescales associated with the dynamics of separation (to be discussed in chapter 5), combined with the energizing of the separated shear layer as the Reynolds number is increased. Both the boundary layer and shear layer are unstable to a range of frequencies/amplitudes, leading to the amplification of the random forcing present in the free stream. As the critical Reynolds number is approached the free shear layer becomes unstable to shorter wavelengths, making it more likely that the roll-up will occur near the sphere and cause enough fluid to be entrained to keep the flow attached. This change to the base flow then likely interferes with the normal vortex shedding process.

An analogous phenomenon can explain the supercritical statistics, though in this case the instabilities would affect the separation bubble. It is likely that if there is a strong enough disturbance, it causes a local change to the wake that increases drag (due to locally breaking up the separation bubble) and produces a side force. This could cause the drag distribution to be skewed, if the strong disturbances are somewhat intermittent. Because the supercritical spectrum also has a low frequency motion, it is postulated that the

disturbances to the supercritical flow are also long lasting, though more data would be necessary to verify this.

3.8.2 Sampling Time for Statistical Convergence

Due to the low frequency motion, it is essential to examine the flow field for a relatively long amount of time in order to get converged statistics. There is significant energy at $\frac{1}{20}$th of the vortex shedding frequency, so to resolve just five of these low frequency oscillations would take $\Delta\hat{t} \approx 500$. The convergence study reveals that this should be a sufficient time to estimate the mean and standard deviation. However, it is better to integrate over $\Delta\hat{t} > 2000$ to fully understand the forcing distribution, which is encapsulated in the skewness and kurtosis.

The need to sample for a very long time may explain the mean supercritical side force found by Constantinescu & Squires (2004), who ran their simulation for a total of $\Delta\hat{t} \approx 50$. However, they found a fairly large mean side force, compared with our standard deviation measurements, so a more detailed explanation of the discrepancy may be required.

Chapter 4

The Effect of a Small Stationary Isolated Roughness Element

4.1 Overview

The effect of an isolated roughness element on the forces on a sphere was examined for a Reynolds number range of $5 \times 10^4 < Re < 5 \times 10^5$. The roughness element (or "stud") was a circular cylinder and its width and height was varied to be 1%, 2%, and 4% of the sphere diameter. It was found that the isolated roughness element has the largest effect on the lateral forces when it is located between a streamwise angle of about 40° and 80°. At subcritical *Re*, a lateral force is produced in the direction of the roughness, while at supercritical *Re*, the force is in the opposite direction. This is caused by asymmetric boundary layer separation, as is shown using particle image velocimetry (PIV). At supercritical *Re*, a roughness element that is only 1% the sphere diameter produces a lift to drag ratio of almost one. In addition to the mean forces, the unsteady forces were also measured. It was found that at subcritical *Re*, the vortex shedding is aligned to the plane of the roughness element. In addition, the probability distribution of the forces was nearly Gaussian for subcritical *Re*, but for supercritical *Re* the skewness and kurtosis deviates from Gaussian, and the details are dependent on the roughness size. These results form the basis of comparison for examining the effect of a dynamic isolated roughness element.

In order to form a complete picture as to the effect of an isolated roughness element, the parameter space, $C_i = f(Re, k/D, \phi_k)$ is examined in detail for each force component (see table 1.1), and the forces are correlated with the mean flow field by using PIV. For the unsteady force and PIV results the stud is placed between $\phi = 60°$ and 70°, because as will be seen, the stud has a large effect at these angles. This study aims to resolve some of the fundamental questions regarding the effect of an isolated roughness element, and it will also form the basis of comparison for examining the effect of a time-dependent surface morphology on the flow over a sphere.

4.2 Reynolds Number Dependence of the Mean Forces

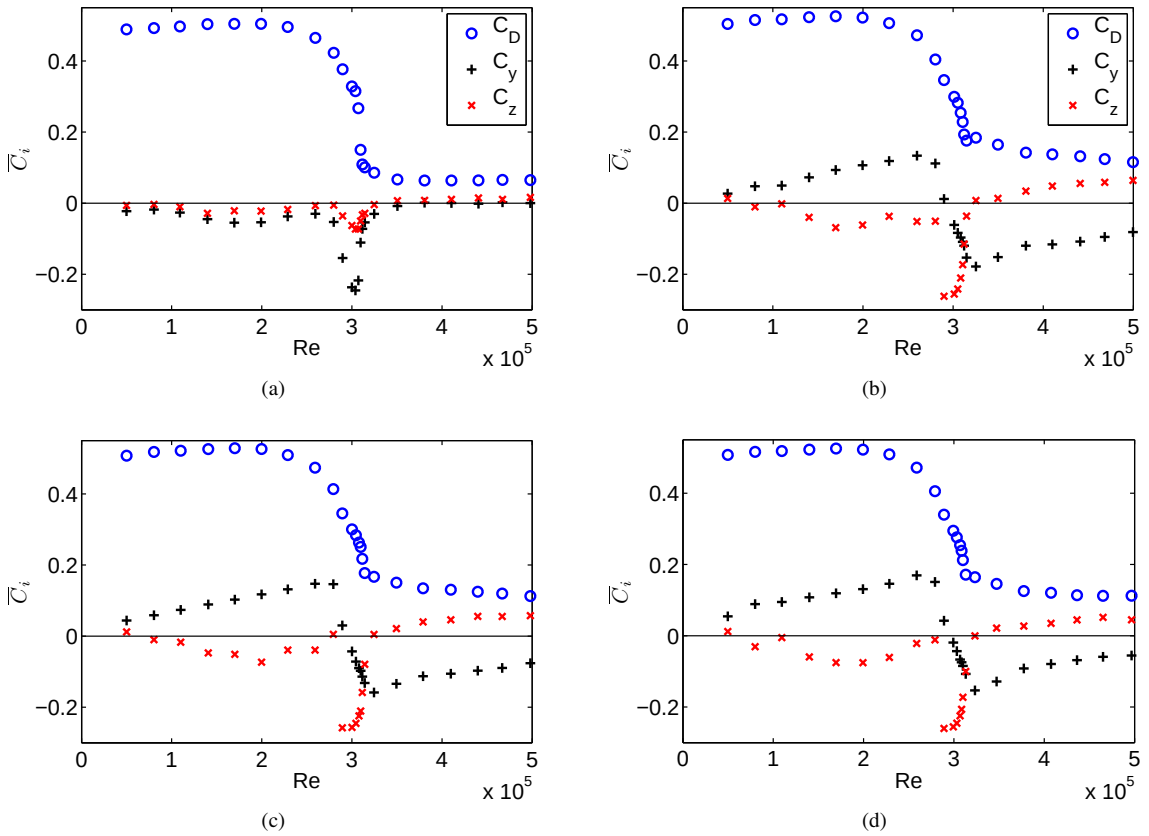

Figure 4.1: Mean force coefficients (C_i, where i represents the drag or one of the lateral force components) as a function of Re without a stud (a) and with a stud placed at $\theta_k = 0°$, $\phi_k = 70°$ with diameter (b) $0.01D$, (c) $0.02D$, and (d) $0.04D$.

The magnitude and direction of the mean force exerted on the sphere is dramatically changed when a stud of varying height is placed at a streamwise angle of $\phi_k = 70°$ (figure 4.1). In the absence of a stud, the mean lateral forces are close to zero away from the critical regime, as expected. The critical regime does not have well defined boundaries, but was classified by Achenbach (1972) to be the region in which the drag rapidly changes, with the minimum drag coefficient occurring at the upper limit of the regime, Re_{crit}. This definition requires refinement in the presence of a stud because there is not a well-defined minimum in the vicinity of the smooth sphere Re_{crit}. However, a similar Re definition of the critical regime can be determined by examining the lateral force with a stud in place. In the presence of a stud the lateral force in the symmetry plane (C_y) is positive at low Re and negative for supercritical Re. Hence the critical regime can be defined to be the Re range in which the derivative of $C_y(Re) < 0$. The lateral force in the plane normal to the plane of the stud, C_z, is close to zero except in the critical regime, where small sphere asymmetries become important and the force arises due to the combined effect of the stud and small imperfections on the sphere (see chapter

3). With the stud at this angle, the mean forces do not change significantly as the stud size is increased from $k/D = 0.01$ to 0.04, though this is not the case at other angles, as described later in this section.

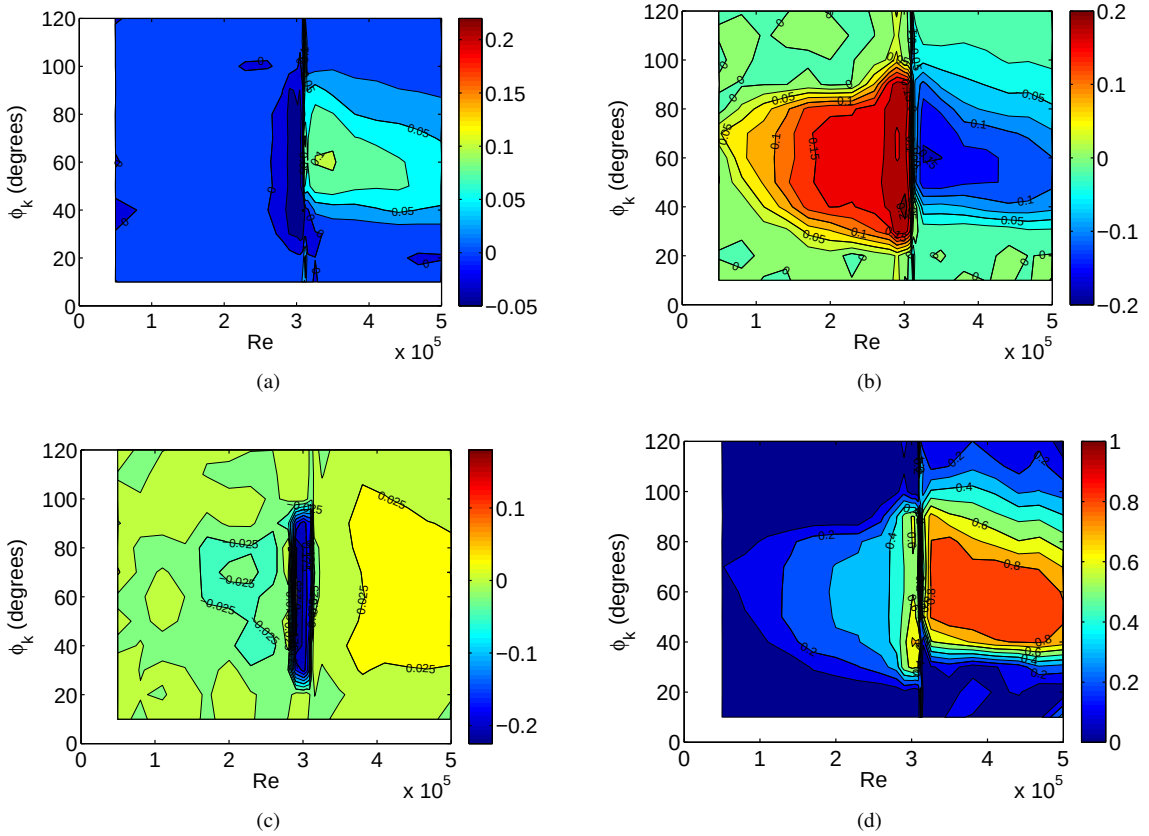

Figure 4.2: Contour plots showing the effect of the stud's streamwise angle, ϕ_k, and Re for a 1% stud: (a) ΔC_D, (b) ΔC_y, (c) ΔC_z, and (d) $|\Delta C_y/C_D|$.

4.2.1 Influence of Streamwise Location of the Roughness Element

Figure 4.2 shows the net change in the mean forces from the smooth sphere case in the presence of the smallest stud as a function of Re and ϕ_k, and figure 4.3 shows a cut of these plots at $\phi_k = 70^\circ$. The data for these plots were obtained by taking measurements every 10° in ϕ_k. The Re step was generally 3×10^4 and smaller in the critical regime.

Figures 4.2a and 4.3a show the change in the drag coefficient, $\Delta C_D = C_D - C_D(smooth)$. The stud has very little effect on subcritical drag, however, the drag is more than doubled in some of the supercritical regime, centered on $\phi = 60^\circ$. These results are similar to those found by Bacon & Reid (1924) when examining the effect of a support wire with diameter $0.2\%D$.

Unlike the drag, the lateral force in the plane of the stud (C_y) changes significantly for subcritical Re. Figures 4.2b and 4.3b show that there is a large positive change to the force over a wide range of Re and ϕ_k. For

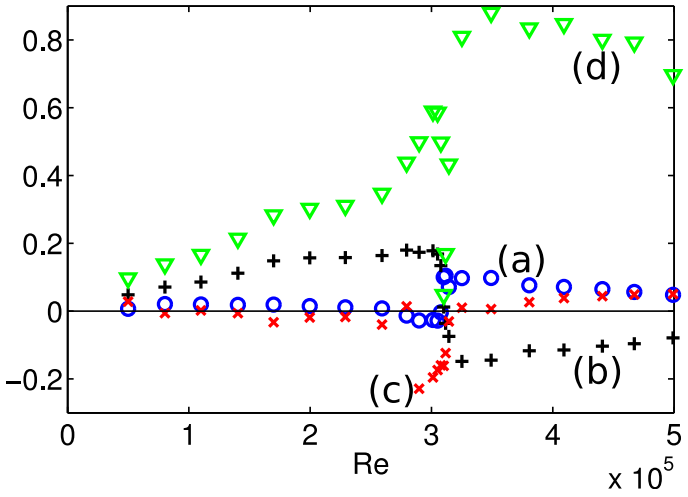

Figure 4.3: 70° cut: ΔC_D (o); ΔC_y (+); ΔC_z (×); $|\Delta C_y/C_D|$ (▽).

small ϕ_k the stud has little effect on C_y, which is expected because the local Reynolds number, Re_k, is small. This is also the case for larger ϕ_k at lower Re. As the stud is moved beyond the mean separation angle and into the recirculating region, it eventually has less and less of an effect. Note that even beyond the separation point a sufficiently large stud can still influence the shear layer and therefore the force development. In the supercritical regime there is a large negative force over a similar range of angles.

Examining the effect of the lateral force that is perpendicular to the streamwise plane of the stud (C_z) highlights the behavior of the critical regime (figures 4.2c and 4.3c). Here, there is essentially no change in the subcritical and supercritical forces, yet in the critical regime there is a large change. The exact flow pattern through the critical regime is difficult to determine, however note that figure 4.1 shows a large negative force in the y-direction for the smooth sphere. If the sphere is rotated, the direction of the lateral force vector, C_L, rotates accordingly, i.e. there is a bias to flow through the critical regime even for this extremely smooth sphere. Thus, since the flow is already strongly influenced by small sphere asymmetries in the critical regime, the full effect observed in figure 4.2c is a combination of the influence of the stud and the model bias. The exact details in the critical regime would clearly be dependent on the sphere being tested.

Figures 4.2d and 4.3d show the relative change in the lateral force from the smooth sphere case, i.e., $|\Delta C_y/C_D|$ where C_D is evaluated with the stud in place. Interestingly a roughness element with $k/D = 0.01$ produces a large lift to drag ratio of nearly one in the supercritical regime, over a broad range of Re and ϕ_k.

4.2.2 Associated Near-Wake Structure

Particle image velocimetry was used to quantify two-components of the velocity field in a planar cut of the near wake and permit correlation between measured forces and the flow structure in a streamwise-radial plane, at subcritical and supercritical Re of 2.0×10^5 (figure 4.4) and 4.1×10^5 (figure 4.5). Based on the contour plots of the mean force components, these conditions should be representative of the entire subcritical

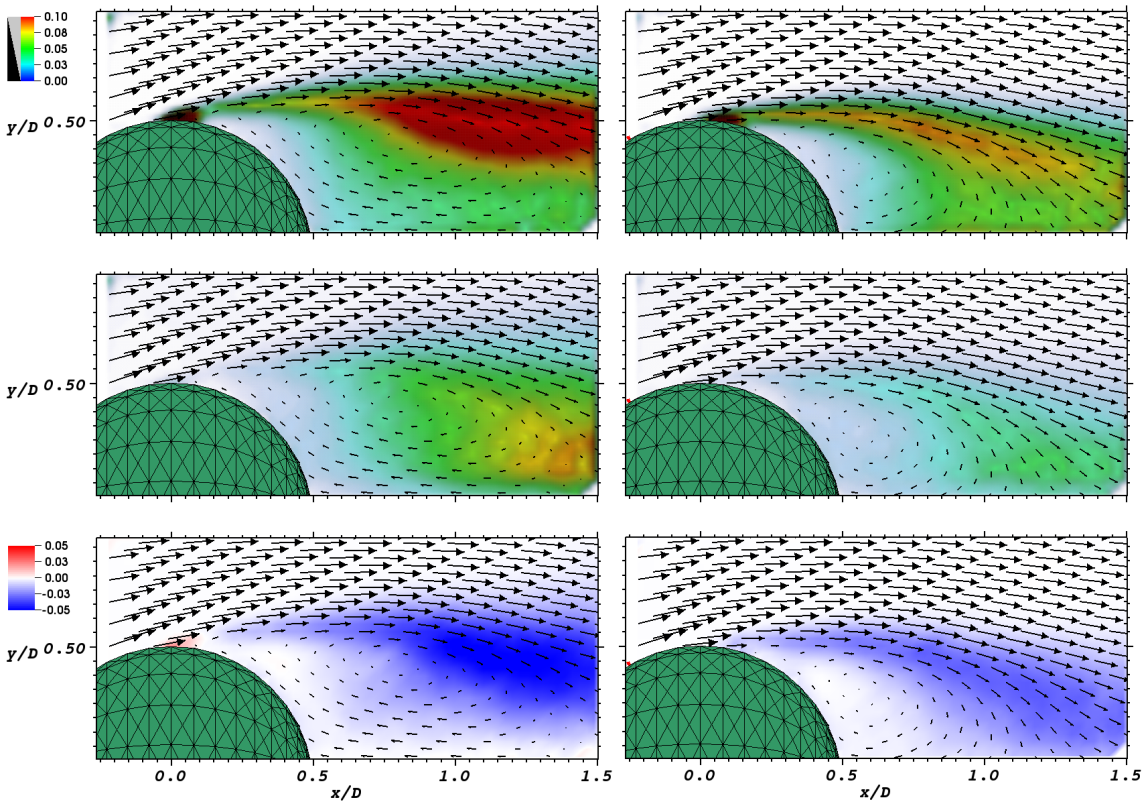

Figure 4.4: Mean velocity field and Reynolds stresses at a subcritical Re of 2.0×10^5 for (left) the smooth sphere and (right) with a $0.01D$ stud placed at $\phi = 60^\circ$ (shown in red) in the plane of the image ($\theta_k = 0^\circ$). Top to bottom: $\overline{u'u'}/U_\infty^2$, $\overline{v'v'}/U_\infty^2$, and $\overline{u'v'}/U_\infty^2$.

and supercritical regimes (all that will change is the magnitude of the effect). For example, the mean field at $Re = 50,000$ with a stud placed at 20° should look essentially similar to the smooth sphere case, because the influence of the stud on the mean forces is negligible. In these figures the vector field of the two-dimensional mean velocity is superimposed on isocontours of the mean Reynolds stresses, with the smooth sphere shown in the left-hand panels and the case of the stud placed at $\phi_k = 60°$ in the plane of the PIV laser sheet (visible on the left-hand side of the images) in the right-hand panels.

For the smooth sphere in the subcritical regime the boundary layer separates far upstream, close to the equator, producing a large recirculating wake. When the isolated roughness is added, the boundary layer appears to separate slightly further downstream, and the size of the near wake shrinks (figure 4.4). The center of the mean recirculation region moves from $x/D = 0.8$ to 0.6 and $y/D = 0.4$ to 0.3. In addition, the mean wake length, defined as the location near the sting where the mean streamwise velocity is zero, moves from an x/D of about 1.4 to 1.1.

A primary effect of the stud can be seen to be an increase in the level of Reynolds stresses in the shear layer close to the sphere (figure 4.4, near $x/D = 0.3$), accompanied by a reduction in the overall levels further downstream, both of which can be attributed to inducing earlier instability of the shear layer and a locally narrower wake due to the later separation of the boundary layer. A particularly interesting observation is that the effect of the stud on the mean velocity field is localized to the upper half plane. When the stud was placed at $\theta_k = 90°$ and 180° away from the PIV plane, the mean velocity field was very similar to the no-stud mean field.

These results suggest the physical mechanism that is responsible for the change in the mean force caused by the stud (figure 4.1). The positive lateral force is caused by the separation delay, which allows the fluid to reach a higher maximum speed before separation, corresponding to lower integrated pressure acting on the upper hemisphere. In addition, the curvature of the shear layer is increased, indicating more fluid entrainment in the near-wake, which would contribute to the decrease in pressure. Combining this with the fact that the mean wake is barely influenced 180° from the stud indicates that on the hemisphere opposite the stud the pressure is likely approximately equal to the smooth sphere case, while on the stud side there is reduced pressure, producing a net positive force.

The supercritical mean velocity field for the smooth sphere (left column of figure 4.5) shows a separation point of about 140°, based on the location of initial increase in the Reynolds shear stress. This is only a rough estimate, ±10°, because the PIV field of view is large. In addition, the Reynolds stresses are likely small immediately downstream of the separation point, so the angle is likely over-estimated. In contrast, Achenbach (1972) directly measured the shear stress and found turbulent separation at $\phi = 120°$, while Taneda (1978) observed an average turbulent separation at about $\phi = 135°$. A rapid downstream reattachment of the separated flow to the sting occurs, corresponding to a narrower wake, with mean reattachment occurring at $x/D = 0.6$. This late separation and subsequent reduction in wake diameter results in an increased importance of the relative size of the sting on the flow field (since the total volume of fluid in the recirculating region

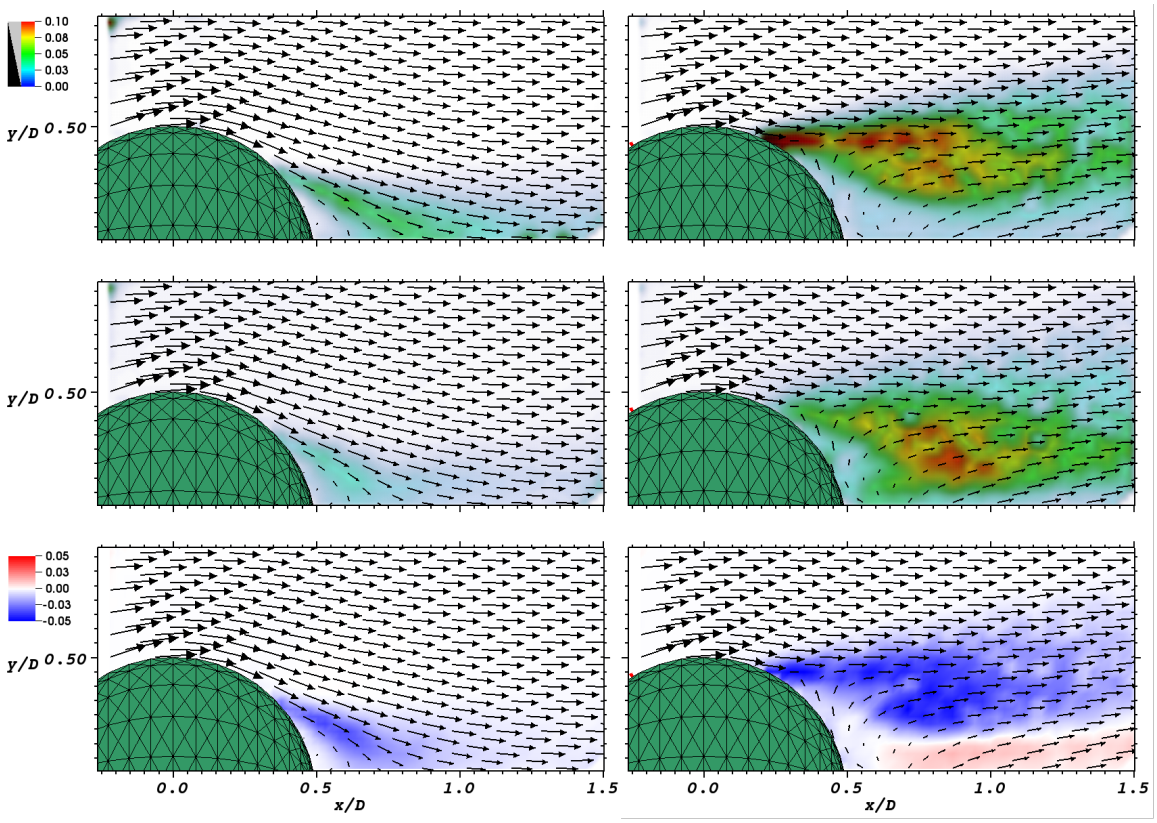

Figure 4.5: Mean velocity field and Reynolds stresses at a supercritical Re of 4.1×10^5 for (left) the smooth sphere and (right) with a $0.01D$ stud placed at $\phi = 60^\circ$ (shown in red) in the plane of the image ($\theta_k = 0^\circ$). Top to bottom: $\overline{u'u'}/U_\infty^2$, $\overline{v'v'}/U_\infty^2$, and $\overline{u'v'}/U_\infty^2$.

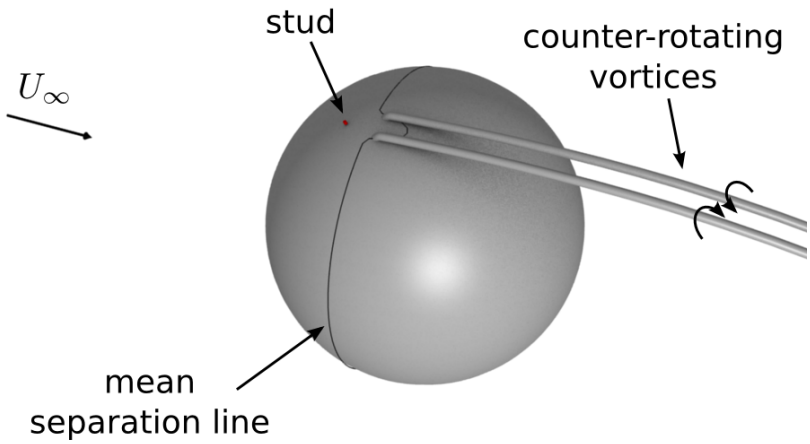

Figure 4.6: The stationary stud locally delays separation in the subcritical regime, likely leading to the production of weak counter-rotating vortices.

is greatly reduced when compared to the subcritical case), in agreement with the observations of Hoerner (1935) of a decreasing supercritical drag with increasing dimensionless sting size. From the mean velocity field it is clear that as the sting size is increased, the sphere and sting will very quickly resemble a streamlined body.

When the small stud is in place, the mean wake is dramatically changed (right column of figure 4.5). The separation point moves from about 140° to 125°, and locally the wake has a large mean radius. Either the stud directly causes the boundary layer to separate on encounter or it influences the transition process. In agreement with this latter hypothesis, Achenbach (1972) found boundary layer transition to turbulent to occur for supercritical flow at almost 100°, while in the higher drag transcritical regime it naturally transitioned earlier on the sphere. Note also that the wake appears to be tilted toward $+y$, in the direction of the perturbed surface of the sphere. As in the subcritical regime, the mean flow is mostly unchanged when the stud is 90° and 180° away from the PIV plane. Near the equator of the base supercritical flow, the velocity is similar to the potential flow solution, whereas the local velocity at the equator behind the stud is reduced due to the early separation and large wake. This indicates that the local pressure near the stud is higher than the base case, which would contribute to the downward force. Thus the combination of earlier separation and larger wake radius associated with the top hemisphere produces a mean downward force, in a reversal of the trend associated with subcritical flow. An increased mean wake diameter leads to a significant supercritical increase in drag coefficient.

The mean flow field slices at 90° azimuthal intervals in the presence of the stud (not shown) are in good agreement with the oil flow visualizations of Taneda (1978), which revealed a horseshoe pattern on the downstream side of the sphere at supercritical Re. While this pattern arose with the same orientation for a nominally smooth sphere, it was noted that the pattern could be aligned using a small surface stud. Given

the sensitivity of the flow to small surface perturbations, it is likely that the primary result arose because of an intrinsic asymmetry in either model or experimental setup. With this in mind, figure 2 in Taneda's paper shows that the asymmetry is localized, with strong similarity in the oil patterns at 90° and 180° away from the large separated region.

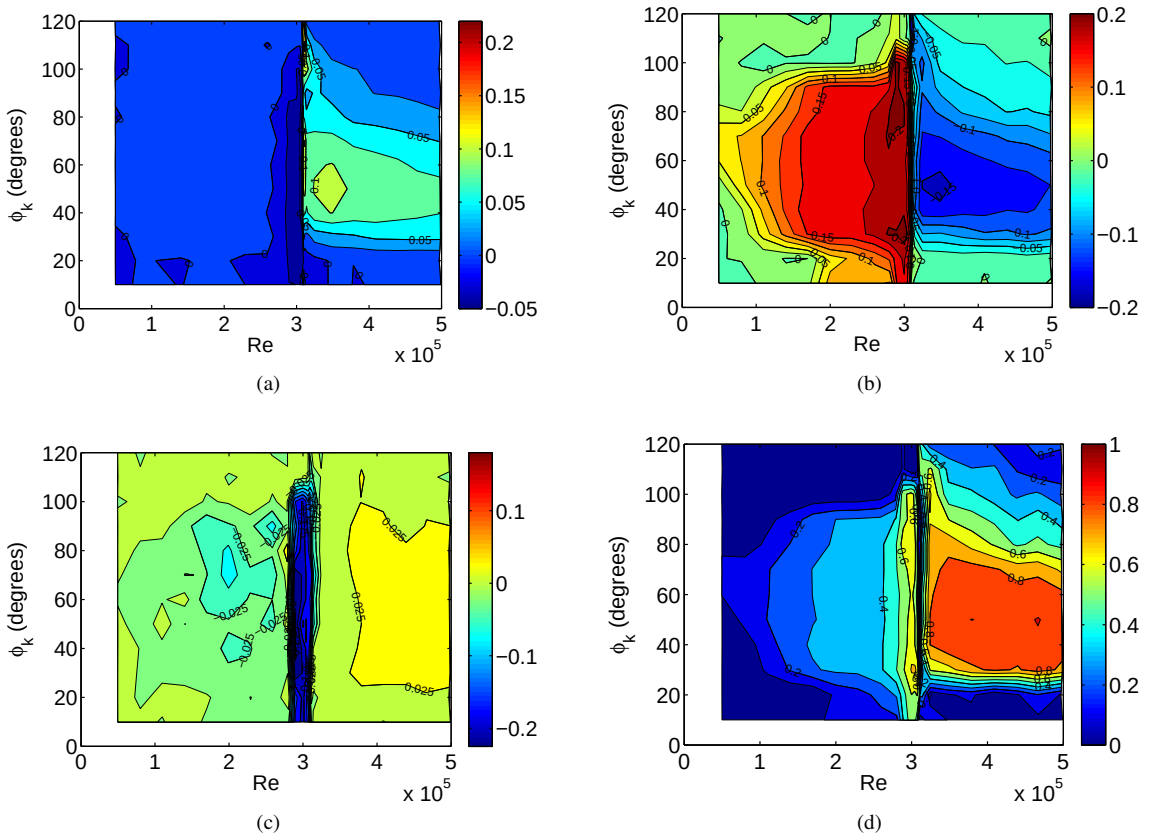

Figure 4.7: Effect of 2% stud: (a) ΔC_D, (b) ΔC_y, (c) ΔC_z, and (d) $|\Delta C_y/C_D|$.

Our essentially zero mean force measurements confirm that our smooth sphere setup does not induce a noticeable asymmetry in the flow (away from the critical regime). However there is good agreement between Taneda's inference of two counter-rotating vortices dominating a tilted wake and our measurements of force and velocity field in the presence of the stud. A mean asymmetry in the angular location of the separation line, in our case induced by the stud, would cause a local roll-up of the shear layer into a counter-rotating vortex pair, with the sense of rotation determined by the perturbation to the mean separation. In the supercritical regime the self-induced vortex motion is away from the sting. It is likely that in the subcritical regime the presence of a stud also leads to the development of counter-rotating vortices, but in the opposite sense to the supercritical case because the local separation is closer to the equator, indicating a reduced pressure compared with the base flow. The hypothesized mean separation line and counter-rotating vortices are sketched in figure 4.6. The mutual interaction of these vortices would push the pair toward the sting, a mechanism that may

play a part in locally forming the shorter recirculation region

4.2.3 Effect of Stud Size

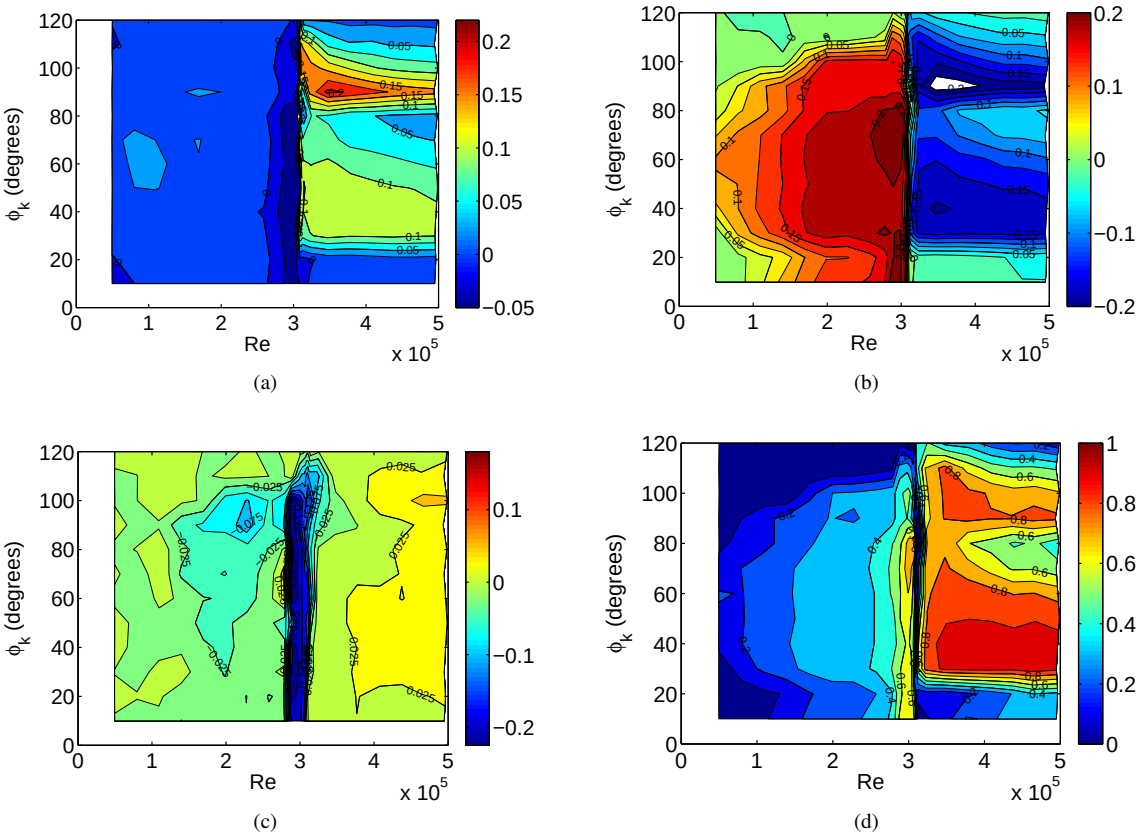

Figure 4.8: Effect of 4% stud: (a) ΔC_D, (b) ΔC_y, (c) ΔC_z, and (d) $|\Delta C_y/C_D|$.

Stud sizes of $k/D = 0.02$ and 0.04 were also considered. As would be expected, a stud that is twice the size affects the mean forces over a larger range of streamwise angles (figure 4.7). For smaller angles, a doubling of the local stud Reynolds number means that the perturbation to the boundary layer is larger, while at angles beyond the separation point the larger stud height means that it protrudes into and influences the separated shear layer over an extended range.

When the stud size is increased to $4\%D$ a secondary ridge occurs in the force contour plots in the supercritical regime (figure 4.8). The peak of this ridge occurs at about $\phi_k = 90^\circ$, and the magnitude of the drag and lateral force changes are larger than the original peak occurring at lower ϕ_k. A likely cause for this second peak is the interaction of the stud with the separation bubble initiating at close to 100° (Taneda, 1978). For increasingly large studs, the induced flow disturbances become big enough to induce premature azimuthally local separation with associated dramatic changes in the mean forces.

4.3 Spectral Density

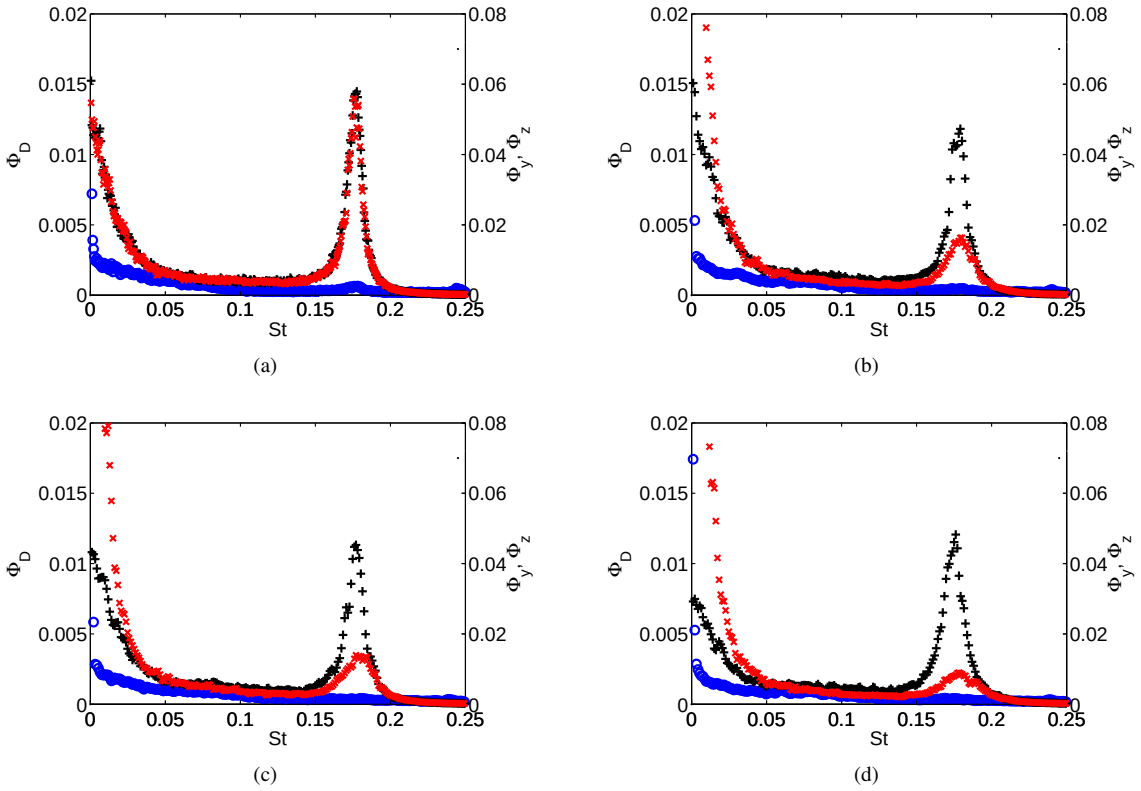

Figure 4.9: Subcritical *Re* of 8.0×10^4 showing the normalized spectral density of the dynamic forces without a stud (a) and with a stud placed at $\theta_k = 0°$, $\phi_k = 70°$ with $k =$ (b) $0.01D$, (c) $0.02D$, and (d) $0.04D$.

Here, the power spectral density of the forces, Φ_i, as a function of *Re* and stud size are examined. A representative low *Re* example is shown in figure 4.9, where the spectral density was normalized as in chapter 3 (Eqn. 3.6).

The spectral power of C_D has been plotted on a different scale to make it visible. For the smooth sphere lateral force (both components), there is a distinct peak at the vortex shedding frequency, and there is also significant broadband power at lower frequencies (figure 4.9a). The data for the lateral forces match almost exactly, which should be the case for a symmetric object. The drag force fluctuations have significantly less power than the lateral fluctuations, but do exhibit a small peak at the vortex shedding frequency. When a roughness element is added (figure 4.9b), the strong lateral force vortex shedding peak remains in the plane of the stud ($y-x$), but almost disappears in the opposite lateral plane. This can be interpreted as a preferential alignment of the orientation of vortex shedding associated with the mean asymmetry in the separation caused by the influence of the stud on the boundary layer development. The effect on the opposite lateral plane is to produce more broadband low frequency fluctuations, perhaps associated with slow dynamics of the separation. Increasing the size of the stud slightly decreases the power levels associated with vortex shedding

in the C_z direction.

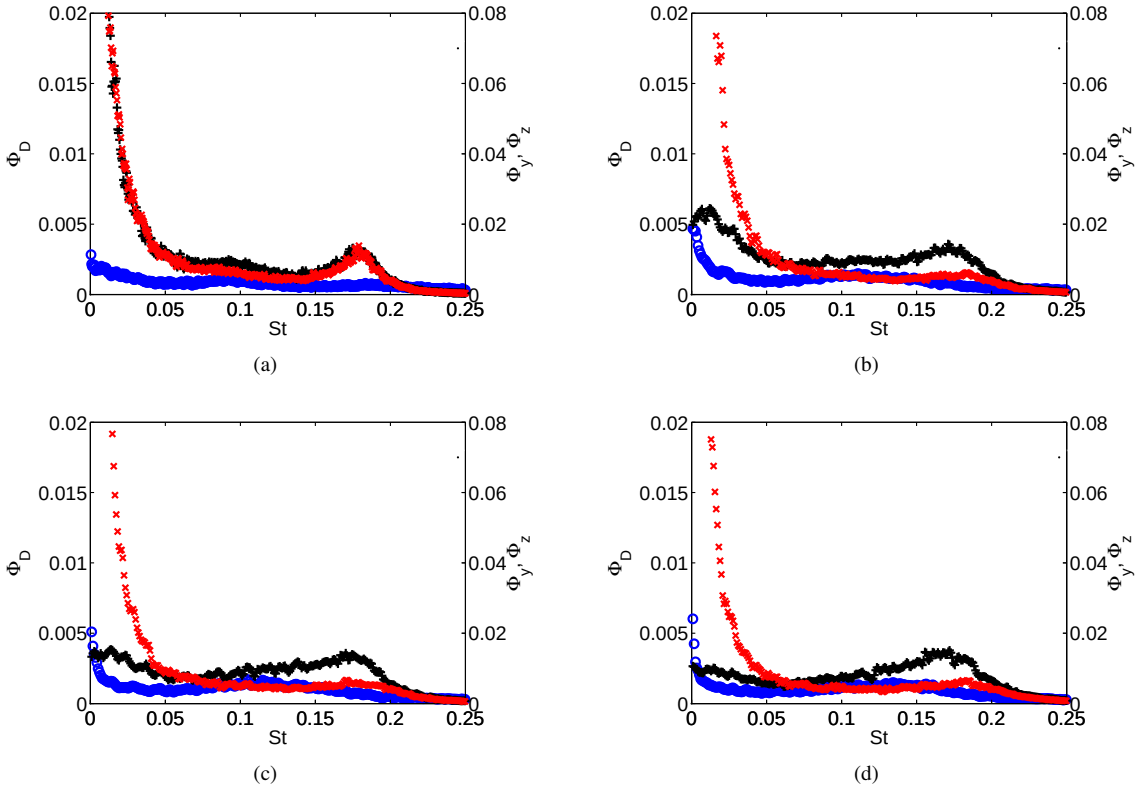

Figure 4.10: Subcritical Re of 2.0×10^5 showing the normalized spectral density of the dynamic forces without a stud (a) and with a stud placed at $\theta_k = 0^\circ$, $\phi_k = 70^\circ$ with $k =$ (b) $0.01D$, (c) $0.02D$, and (d) $0.04D$.

As the Reynolds number is increased, the contribution to the fluctuating forces associated with vortex shedding decreases, until it disappears near Re_{crit}. At an intermediate subcritical Re of 2.0×10^5, the vortex shedding is very weak, and most of the power is concentrated in a broadband low frequency range (figure 4.10a). The presence of a small stud at $\phi_k = 70^\circ$ dramatically alters the force distribution (figure 4.10b). The low frequency content is significantly decreased in the C_y direction (which is in the plane of the stud), while in the C_z direction the vortex shedding peak is essentially gone. As the stud size is increased, the low frequency content in the C_y direction continues to decrease, and the fluctuations become fairly evenly distributed below a Strouhal number of about 0.2. These changes appear to confirm that this low frequency activity, observed also in earlier studies, is a real feature of sphere flow rather than an artifact of the experimental method.

In the supercritical regime there is no vortex shedding detected near the subcritical vortex shedding frequency of $St \cong 0.18$. As the Reynolds number is increased, the dimensionless minimum natural frequency of the supporting structure decreases, so the maximum St that is detectable also decreases. At an Re of 4.4×10^5, this limits the maximum St to about 0.18, making it impossible to detect the vortex shedding that is likely occurring at a higher St in the supercritical regime (see, e.g., Constantinescu & Squires, 2004). However there is a clear change in the spectral shape associated with a surface stud. For the smooth sphere the spectrum has

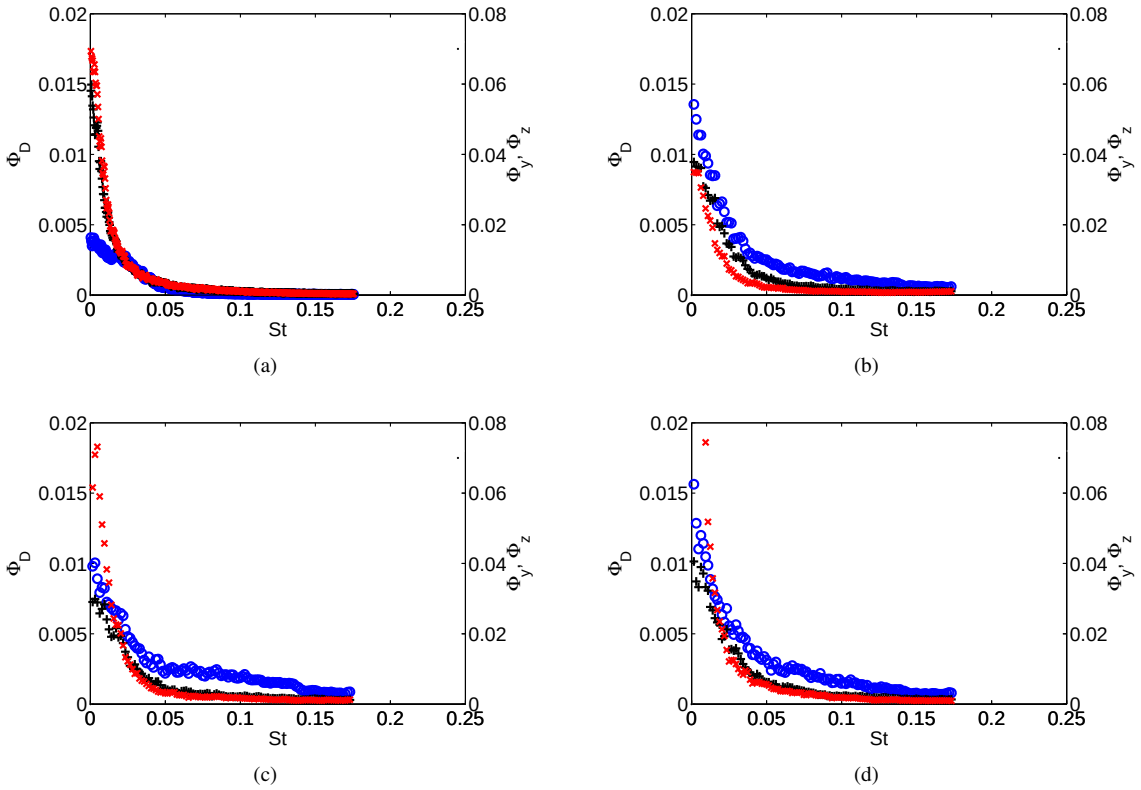

Figure 4.11: Supercritical Re of 4.4×10^5 showing the normalized spectral density of the dynamic forces without a stud (a) and with a stud placed at $\theta_k = 0^\circ$, $\phi_k = 70^\circ$ with $k =$ (b) $0.01D$, (c) $0.02D$, and (d) $0.04D$.

significant power at low frequencies (figure 4.11a). When the small stud is added, the fluctuations become more broadband, and the fluctuating drag levels significantly increase. As the stud size is increased, the lateral force spectra begin to diverge, accompanied by further increases in drag fluctuations. It would be interesting to see the effect on the supercritical vortex shedding, however, it was not possible in these experiments to make a sufficiently rigid structure without requiring a sting large enough to change the dynamics of the base flow.

4.4 Moments

The higher-order moments of the forces as a function of *Re* were previously described for the case of a smooth sphere (section 3.4), and here are extended to examine the effect of an isolated roughness element.

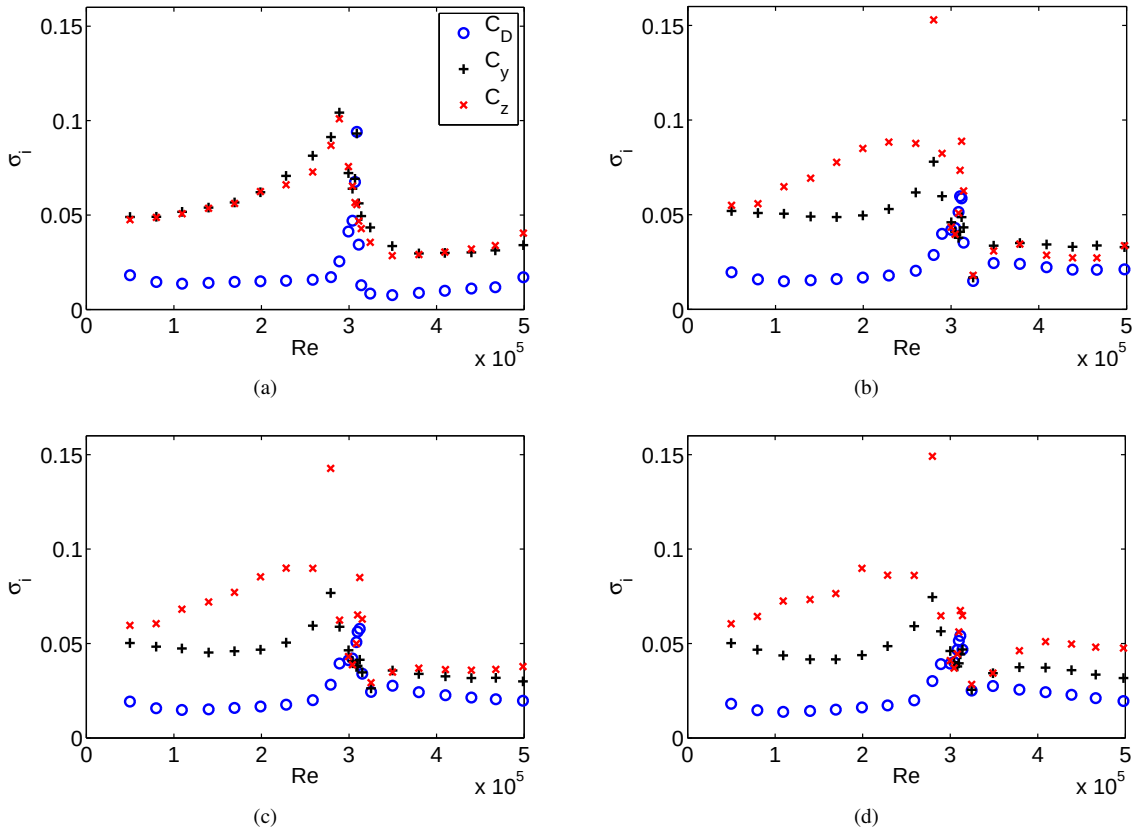

Figure 4.12: Standard deviation of the force coefficients as a function of *Re* without a stud (a) and with a stud placed at $\theta_k = 0^\circ$, $\phi_k = 70^\circ$ with $k =$ (b) $0.01D$, (c) $0.02D$, and (d) $0.04D$.

In the subcritical regime a stud placed at $\phi_k = 70^\circ$ affects the moments, with the stud size playing only a small role, as would be expected from the preceding figures. The standard deviation in the plane of the stud (figure 4.12) decreases, while it increases in the opposite lateral direction. This is explained by the spectral density plots in section 4.3 which suggested that in the plane of the stud the vortex shedding was aligned

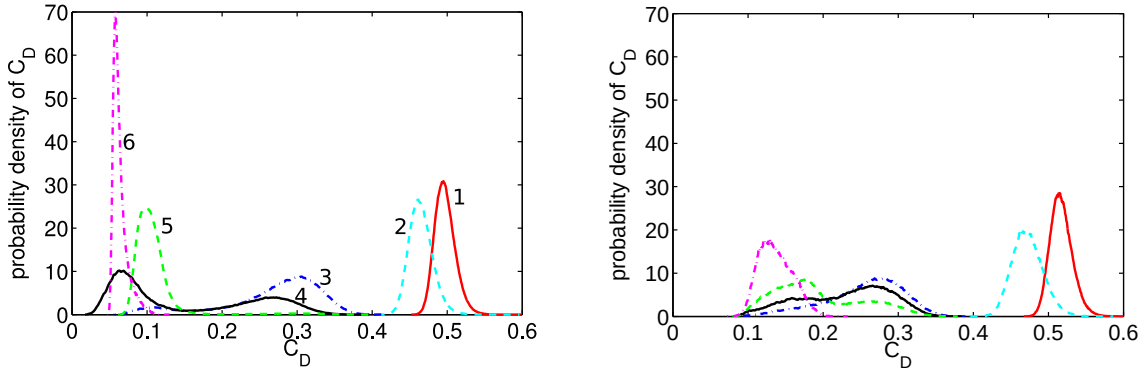

Figure 4.13: Probability density for: subcritical Reynolds numbers (1) 1.1×10^5, (2) 2.6×10^5; critical *Re* (3) 3.07×10^5, (4) 3.09×10^5, (5) 3.11×10^5; and supercritical *Re* (6) 4.1×10^5. (a) no stud, (b) $0.01D$ stud.

and the lower frequency motion decreased, while there was more irregular motion in the opposite plane. The combined effect of the change to the lateral forces is to increase the standard deviation of the lateral force vector magnitude by about 15% in the subcritical regime, and 30% in the supercritical regime (not shown).

In the critical regime, the smooth sphere peak in the drag fluctuations (due to the drag transitioning from the subcritical to the supercritical state (chapter 3.4)) is also associated with a peak in the C_y fluctuations. This is likely caused by the large mean force in the y-direction (see figure 4.1) at this Reynolds number, indicating a tilted wake. With a stud in place, the mean force at this *Re* becomes more associated with the z-direction, and likewise the fluctuating force increases in the same direction. This reason for the change in the mean force is given in section 4.2.1: the exact details of the critical regime are dependent on the interaction of the sphere asymmetries and the stud.

In the supercritical regime, the most noticeable change associated with surface asymmetry is an increased standard deviation of the drag component and higher levels of lateral fluctuations in the plane perpendicular to the plane containing the stud for $k = 0.04D$. Note, however, that these supercritical results represent a lower bound on the true values of standard deviation, since oscillations above $St \approx 0.2$ cannot be detected with our setup.

The statistics are more easily understood by comparing the probability density functions (pdfs) for no stud and small stud data sets (figure 4.13). More details of the smooth sphere case can be found in section 3. The subcritical pdfs are not significantly changed by the addition of a stud, and while the critical regime shows a bimodal distribution similar to the smooth case, the spacing between the different modes has decreased. The most notable change is a shift to a broader supercritical distribution centered at higher C_D, which is supported by the drastic change to the wake structure illuminated by the PIV results. Once again the effect of stud size does not appear to be significant over the range considered.

In the subcritical regime the skewness (figure 4.14) and kurtosis (figure 4.15) show that the statistics of the distribution are approximately Gaussian, even when the stud is in place. In the critical regime, both the

skewness and the kurtosis have extreme peaks, which are associated with the bimodal drag distribution which was described earlier. In the supercritical regime, the smooth sphere drag distribution is highly skewed, while when the stud is added, the drag becomes less skewed and the C_z force component becomes negatively skewed. The kurtosis shows a similar trend: without the stud the drag has a high kurtosis, and with the stud C_z has a high kurtosis. This odd behavior of C_z comes from a very lopsided bimodal distribution when the stud is in place (not shown), where most of the energy is centered on $C_z = 0.05$, while there is a very small secondary peak at $C_z = -0.04$. As the stud size is increased the kurtosis becomes more Gaussian, due to the energy becoming more evenly distributed between the peaks. The effect of the stud on the lateral distributions seems to mainly be that it brings more order to the plane in which the stud is located, while it brings less to the opposite plane (not shown).

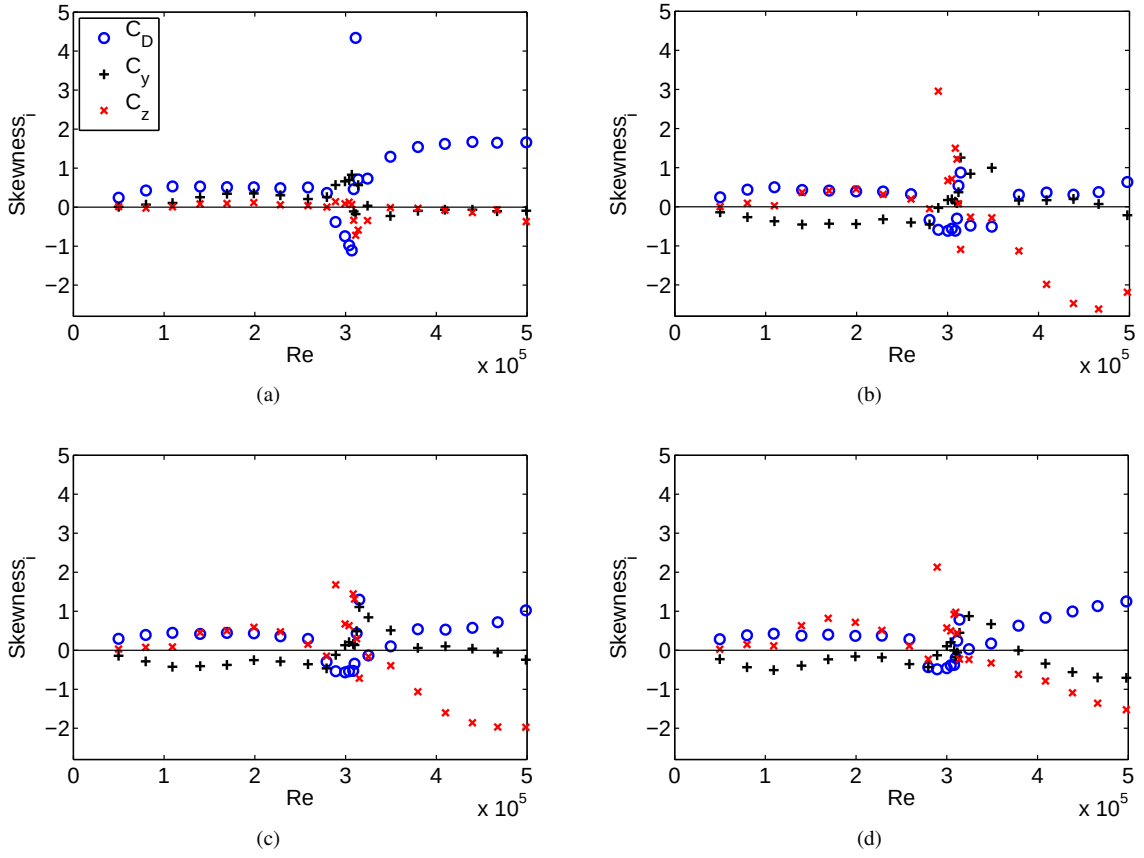

Figure 4.14: Skewness of the force coefficients as a function of *Re* without a stud (a) and with a stud placed at $\theta_k = 0°$, $\phi_k = 70°$ with $k =$ (b) $0.01D$, (c) $0.02D$, and (d) $0.04D$.

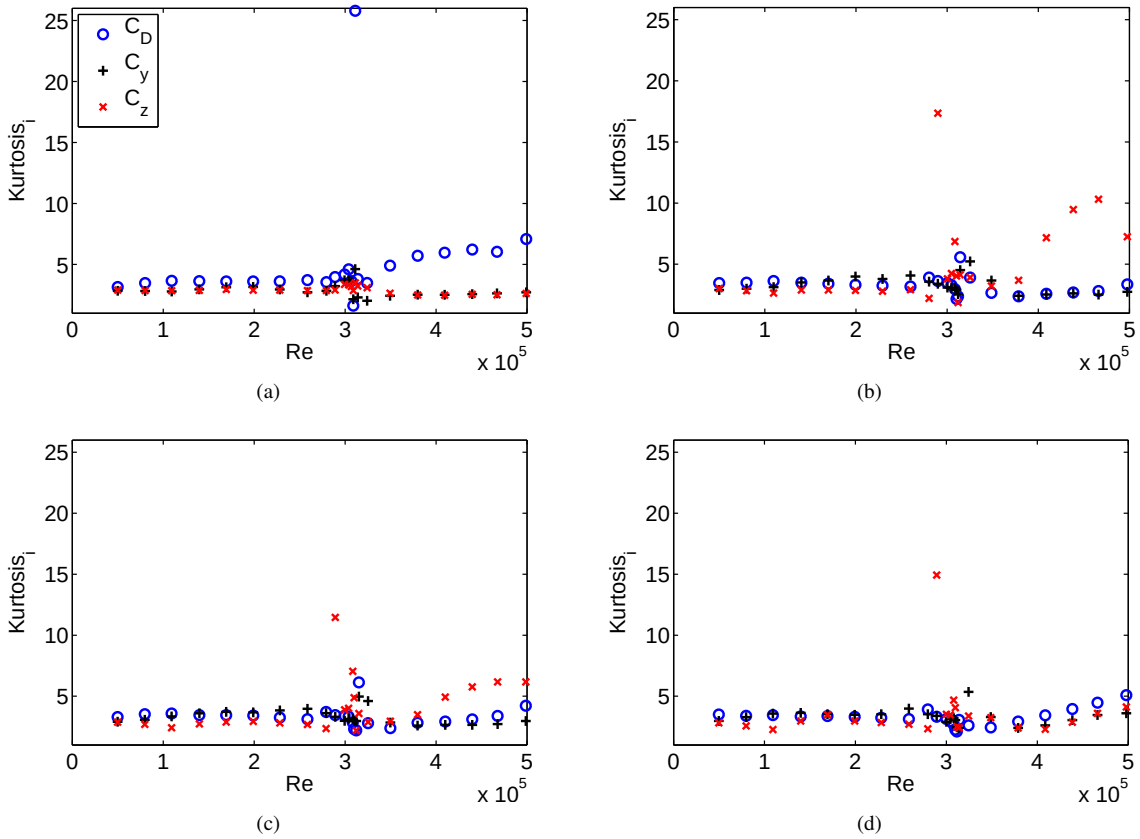

Figure 4.15: Kurtosis of the force coefficients as a function of *Re* without a stud (a) and with a stud placed at $\theta_k = 0^\circ$, $\phi_k = 70^\circ$ with $k =$ (b) $0.01D$, (c) $0.02D$, and (d) $0.04D$.

4.5 Summary

The effect of an isolated stationary roughness element on the flow over a sphere has been examined over a broad range of Reynolds numbers, and the results are in good agreement with and extend the relatively sparse literature. A piezoelectric force sensor was used to obtain precise force measurements, which were correlated with the behavior of the flow using particle image velocimetry. The flow is significantly affected when a stud with $k/D = 0.01 - 0.04$ is placed over a large range of streamwise angles from the front stagnation point, from about $40^\circ < \phi_k < 80^\circ$.

In the subcritical regime, it was found that the stud caused a local delay in separation, leading to a positive mean force in the $+y$ direction while having little effect on the drag. It is argued that the roll-up of the shear layer produces a pair of streamwise vortices, with mutual induction toward the sting. At lower *Re*, there is a distinct peak in the spectral density associated with large-scale vortex shedding, along with broadband lower frequency motion. When a stud is placed on the sphere, the vortex shedding aligns with the plane of the stud. As *Re* approaches Re_{crit}, the force contribution near the vortex shedding frequency gradually decreases until the peak is gone. The statistics of the subcritical regime are found to be nearly Gaussian, even in the presence

of a stud.

The behavior in the critical regime will always be highly dependent on small asymmetries of the sphere, even though steps were taken to ensure an accurate sphere model. However, this is not surprising since the boundary layer is transitioning from laminar to turbulent, and is thus highly sensitive to imperfections. If the sphere was rotated, the mean side force in the critical regime rotated accordingly (but note that the mean side force was essentially zero either side of this regime). When a stud was in place, the forces were dependent on some combination of the effect of the stud and the effect of other small asymmetries. The statistics were far from Gaussian during the transition, especially when the drag was in a bimodal state, changing from the high drag subcritical state to the low drag supercritical state.

In the supercritical regime, the stud caused a premature, rather than delayed, separation of the boundary layer, leading to a negative force. In the absence of a stud, the flow very quickly attaches to the sting, leaving a very narrow mean wake, while the early separation caused by the stud produces a locally large wake and a significant increase in drag. Over a large range of Re and ϕ_k, the lift to drag ratio is nearly 1, even when the stud dimensions are only 1% the sphere diameter. As the stud size is increased to $4\%D$, a secondary mean force peak occurs at about $\phi_k = 90^\circ$. This is attributed to the stud being near the beginning of the separation bubble. The statistics in the critical regime are not Gaussian, and vary depending on the size of the stud.

The variation of the forces acting on the sphere with a surface perturbation that is only a few percent of the sphere diameter underline the extreme complexity of this flow. Through this study the wake structure associated with the presence of a local asymmetry imposed by a stud has been suggested, namely a pair of counter-rotating vortices that trail the stud on a scale much larger than the stud diameter, and it is proposed that this may be a useful concept for understanding the behavior of the flow over a smooth sphere.

Chapter 5

The Effect of Small-Amplitude Time-Dependent Changes to Surface Morphology

5.1 Overview

Typical approaches to manipulation of flow separation employ passive means or active techniques such as blowing and suction or plasma acceleration. Here it is demonstrated that the flow can be significantly altered by making small changes to the shape of the surface. A proof of concept experiment is performed using a very simple time-dependent surface perturbation: a roughness element of only 1% of the sphere diameter is moved azimuthally around the sphere surface upstream of the uncontrolled laminar separation point, with a rotational frequency as large as the vortex shedding frequency. A key finding is that the nondimensional time to observe a large effect on the lateral force due to the perturbation produced in the sphere boundary layers as the roughness moves along the surface is $\hat{t} = tU_\infty/D \approx 4$. This slow development allows the moving element to produce a tripped boundary layer over an extended region. It is shown that a lateral force can be produced that is as large as the drag. In addition, simultaneous particle image velocimetry and force measurements reveal a pair of counter-rotating helical vortices are produced in the wake, which have a significant effect on the forces, and greatly increase the Reynolds stresses in the wake. In addition, it is shown that oscillating the roughness element, or shaping its trajectory, can produce a mean lateral force.

5.2 Roughness Element Moving at Constant Speed

The forces on the Teflon coated sphere used in the dynamic stud experiments (which is different than the one used previously) and the effect of a stationary stud as a function of Reynolds number are shown in figure 5.1. The results are similar to those for the sphere which was examined in chapter 4, though the critical Reynolds number is higher (indicating that the effective roughness is lower), in good agreement with the smooth sphere

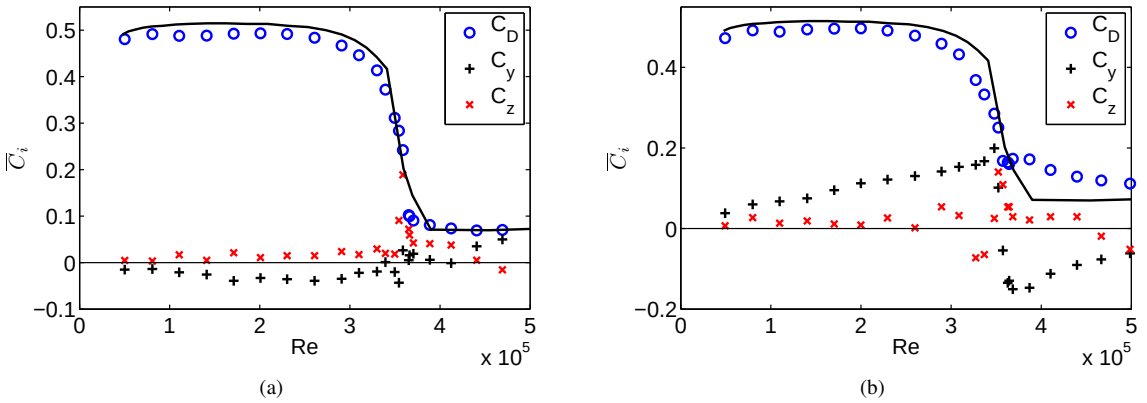

Figure 5.1: Static forces and a comparison with the smooth (−) sphere results from Achenbach (1974*a*): (a) smooth sphere results and (b) the same sphere with a $0.01D$ stud placed at $\phi_k = 60^\circ$.

results of Achenbach (1974*a*).

Figure 5.2 shows a time trace of the lateral forces for a total time of $\hat{t} = 100$ without a stud and with a dynamic stud moving at two different constant angular frequencies, expressed as the dimensionless quantity

$$\omega^* \equiv \dot{\theta}_k D/U_\infty. \tag{5.1}$$

The forces due to a stationary stud are very similar to the no stud case, except with a small mean offset (chapter 4). By adding time-dependence to the stud's position, the lateral forces are completely altered, with most of the spectral energy centered on the frequency of stud rotation. Though the mean force is not altered (see section 2.2.1 for notation), the fluctuating forces increase substantially. At any given instant the magnitude of the lateral force is approximately $|\vec{C}_L(\hat{t})| = 0.46$ for $\omega^* = 0.52$, an order of magnitude larger than the mean lateral force due to a stationary stud. This is surprisingly large considering that the effect is caused by a very small perturbation to the sphere morphology, yet when an entire golf ball spins about an axis perpendicular to its direction of motion at $\dot{\phi}D/U_\infty = 0.52$, it has a mean lateral force of about 0.2 (Bearman & Harvey, 1976), due to the Magnus effect. Not apparent in figure 5.2 is that the angle to the lateral force vector (θ) lags behind the stud angle, where the phase difference, $\theta - \theta_k$ is dependent on the angular frequency.

5.2.1 Effect of Reynolds Number

The mean phase difference between the direction of the lateral force and the azimuthal location of the stud is plotted along with the mean of the lateral force magnitude in figure 5.3 for a large range of Reynolds numbers, showing that ω^* provides very good collapse of the data for subcritical Reynolds numbers. These calculation are based on the mean force in the stud reference frame, and are described in section 2.5.3.

As the stud speed is increased, the lateral force first increases from its stationary zero-speed value until it reaches a maximum near $\omega^* = 0.5$, after which point it begins to gradually decrease. Note that the magnitude

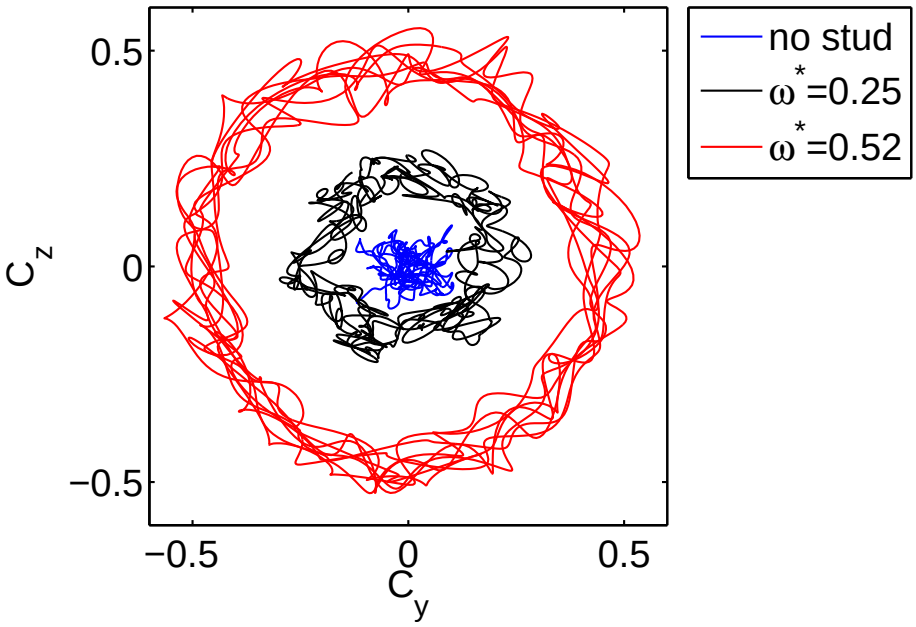

Figure 5.2: Time trace of the lateral force coefficients for $Re = 5 \times 10^4$, showing that the dynamic stud completely changes the force characteristics. The mean of the lateral force magnitude of the moving stud is up to seven times larger than that of the stationary stud.

of the lateral force is dependent on the magnitude of the stationary stud force ($\omega^* = 0$). The stud makes one revolution during an average vortex shedding cycle when $\omega^* = 1.1$. Near this angular frequency there is not an amplification of the lateral forces (compared with adjacent frequencies), as might be expected if the dramatic effects were caused by a direct interaction with the wake instability. However, the peak is close to a subharmonic, and Chomaz *et al.* (2006) interpreted the wake instability as a helical instability, so there may be some connection.

The phase difference between the force vector and stud exhibits three distinct regimes (figure 5.3). First there is a sudden decrease in the phase with increasing ω^*. This levels off near $\theta - \theta_k = -90^\circ$, and then the phase difference begins to decrease nearly linearly beyond $\omega^* = 0.35$. These results are extremely independent of Reynolds number in the subcritical regime, and are not dependent on the magnitude of the stationary stud force, as is the case for the mean lateral force.

The effect of the dynamic stud is quite different in the supercritical regime, as is to be expected because the flow separates turbulently, further downstream. Figure 5.3 shows the results for $Re = 4.1 \times 10^5$, indicating that in the supercritical regime the mean lateral force and phase do not change significantly over the range of angular frequencies examined. Note also that the phase is approximately -180°, which is the same phase that a stationary supercritical stud would produce, due to the lateral force vector pointing away from the stud.

The focus of this chapter will be on $Re = 5 \times 10^4$, because the stud has the highest dimensionless speed at this Re. However, figure 5.3 reveals that the physics appear to be essentially the same over the entire subcritical Reynolds number regime examined here, at least from $5 \times 10^4 < Re < 3.1 \times 10^5$. Thus, the results

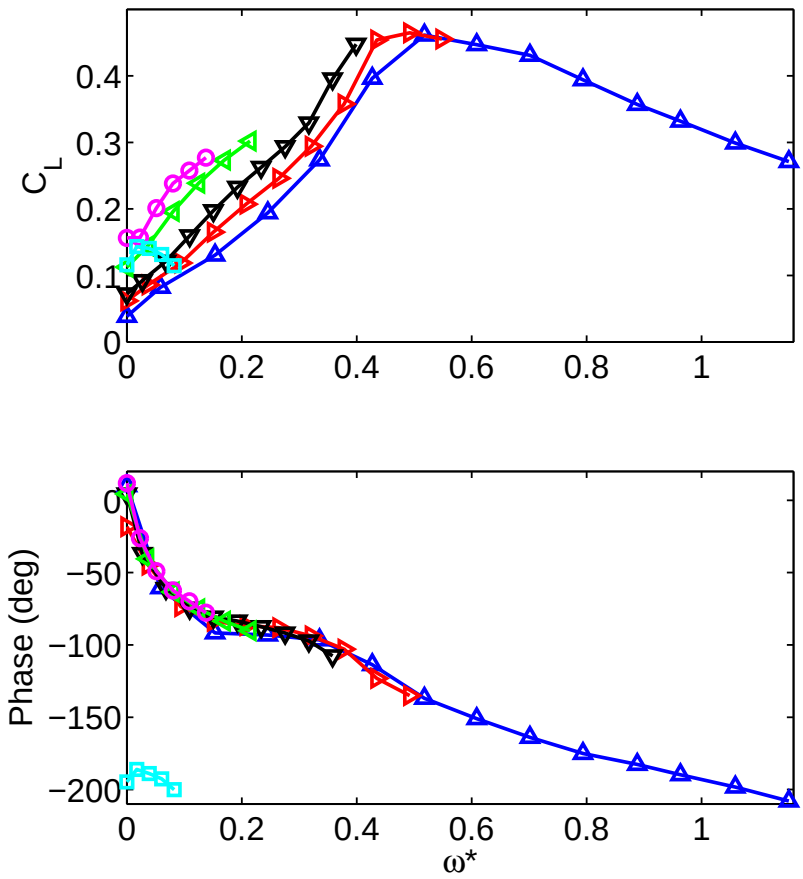

Figure 5.3: Mean C_L and phase $(\theta - \theta_k)$ (in stud reference frame) vs. dimensionless angular frequency. $Re = 0.5 \times 10^5$ ($\triangle$); $Re = 0.8 \times 10^5$ ($\triangleright$); $Re = 1.1 \times 10^5$ ($\triangledown$); $Re = 2.0 \times 10^5$ ($\triangleleft$); $Re = 3.1 \times 10^5$ (o); $Re = 4.1 \times 10^5$ ($\square$).

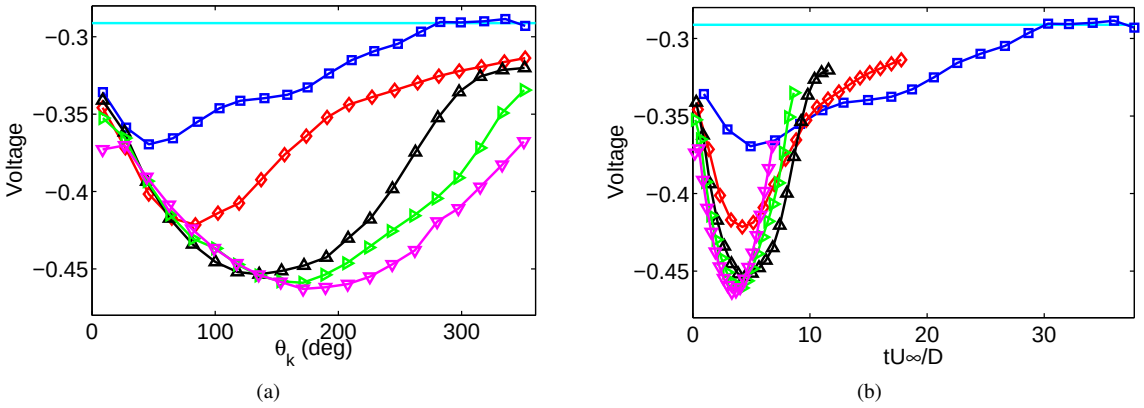

Figure 5.4: (a) Uncalibrated hot-film voltage: lower voltage indicates greater heat transfer. Results are for $Re = 5.0 \times 10^4$ and are averaged over 100 revolutions, as a function of the stud angle, in order to suppress voltage oscillations caused by vortex shedding. (b) Normalized with respect to time since the stud passed. No stud mean (-); $\omega^* = 0.15$ (□); 0.34 (◊); 0.52 (△); 0.70 (▷); 0.89 (▽).

presented below are applicable to the subcritical regime, and more generally, it may be possible to draw conclusions for other bodies that have a variable, laminar separation point.

5.2.2 Flow Response Time

Hot-film measurements at $\phi = 70^\circ$ reveal the phase relationship between the location of the stud and the response of the boundary layer (figure 5.4). The vertical axis shows the uncalibrated voltage signal, with lower voltage indicating greater heat transfer and thus higher velocity/shear stress. The horizontal line shows the mean voltage produced without a stud, and the other data are the phase-averaged voltage over many stud revolutions as a function of stud position, with varying angular frequencies. The boundary layer and free shear layer are receptive to disturbances, and it is likely that the passing stud locally triggers these instabilities, which then grow and convect downstream, gradually entraining more fluid and delaying the separation, which would change the velocity near the hot-film. At the lowest frequency, it is seen that the local velocity has time to readjust to the smooth sphere value before the stud makes a full revolution. However, with all of the other speeds the flow does not have time to fully readjust.

In figure 5.4b the x-axis was rescaled to show the nondimensional time since the stud passed instead of the position of the stud, revealing that the flow does not fully respond until $\hat{t} = tU_\infty/D \approx 4$ after the stud has passed. This is similar to the response time of a stalled airfoil to a perturbation of the boundary layer upstream of separation (Williams *et al.*, 2009). As will be seen in the flow visualization results presented in the next sections, this time delay is associated with a large-scale change of both the location of flow separation and the wake.

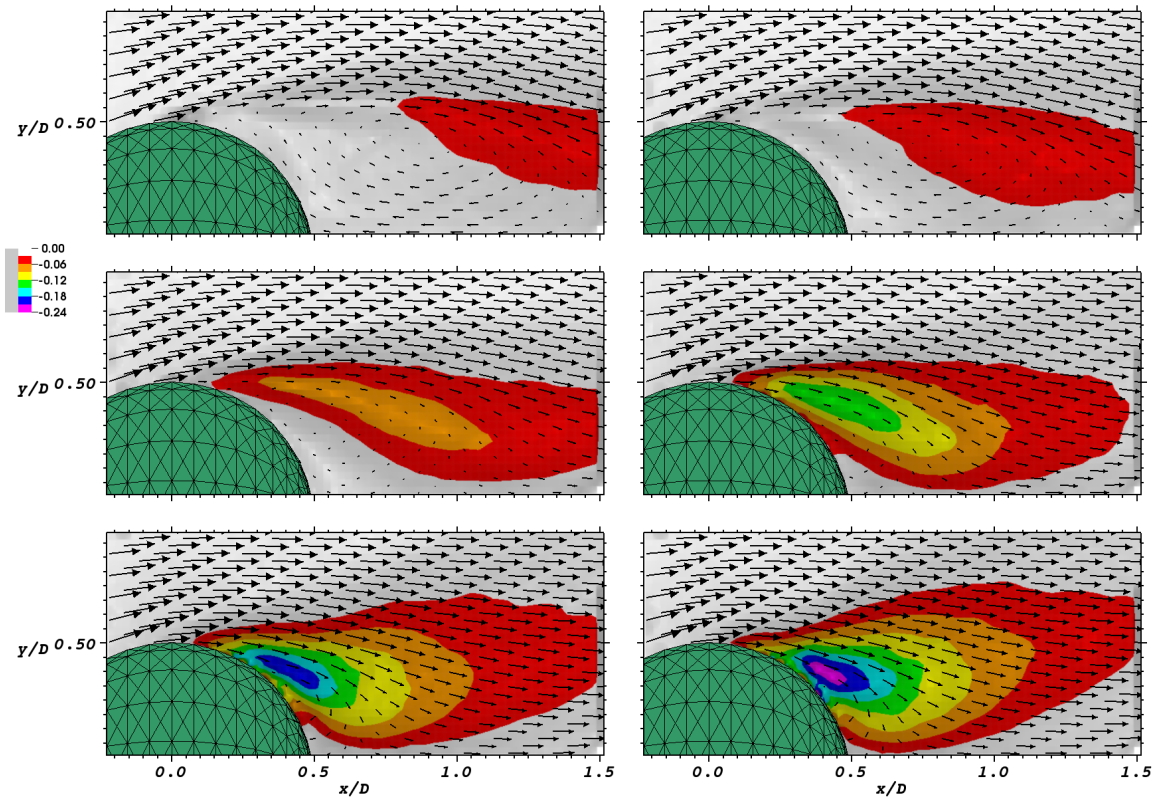

Figure 5.5: Mean velocity field and mean Reynolds shear stress for (left to right then top to bottom): no stud, $\omega^* = 0.15$, 0.34, 0.52, 0.70, and 0.89.

5.2.3 Effect on Mean Flow

The dramatic change to the mean wake due to a moving stud is shown in figure 5.5, with the color contours indicating the mean Reynolds shear stress, $\overline{u'v'}/U_\infty^2$. The top left image corresponds to the smooth sphere base flow, which is very similar to the no-stud higher subcritical *Re* results shown in chapter 4. With the stud moving at $\omega^* = 0.15$ (which corresponds to 1Hz at this *Re*), there is very little change to the wake structure. As the speed is increased the mean separation point moves further downstream and the mean wake gradually shrinks, and at $\omega^* = 0.89$ the mean velocity field looks more similar to the supercritical wake than the subcritical wake (chapter 4), though the Reynolds stresses have dramatically changed, with the maximum value being more than a factor of four larger than the supercritical case. Note also that as the stud speed is increased, the position of the maximum Reynolds shear stress moves closer to the sphere. This holds for the streamwise and radial Reynolds stresses as well (not shown).

5.2.4 Instantaneous Velocity Field

A better understanding of what causes the significant changes to the flow can be found by examining the instantaneous velocity field. Synchronous force and particle image velocimetry measurements were taken in the top half of the x-y plane (i.e. the streamwise plane with $\theta = 0^\circ$) for five different stud speeds, three of which are shown in figures 5.6 – 5.8. Image pairs were acquired at a frequency which allowed at least 100 vector fields to be calculated per stud revolution. Results for the smooth sphere, which reveal a large and slowly varying wake, can be found in chapter 3.

For the lower speed run ($\omega^* = 0.15$, figure 5.6), there is a clear effect of the stud in the force history, and the force can be related to a change in the flow field. Four velocity fields which cover one full rotation of the stud are plotted, with the first one corresponding to the time when C_y was close to a maximum, with the stud at $\theta_k = 81^\circ$. This first velocity field has a small recirculation region, compared with the other three, indicating enhanced entrainment in the shear layer. This pattern repeats itself with each oscillation of the stud, with random force variations superimposed on top of the stud frequency, as can be seen by examining the adjacent maxima on the force plot. The overriding impact of the stud allows for a phase-averaged force and flow field to be calculated, which will be described in the next section.

At a higher stud speed of $\omega^* = 0.52$, the magnitude of the lateral force becomes as large as the drag, and the wake structure is strongly modified (figure 5.7). Once again, when the lateral force in the PIV plane is a maximum (with the stud at $\theta_k = 123^\circ$), the flow remains attached much further downstream, and there is a very small recirculation region. The second and fourth vector fields are quite distinct, yet the mean in-plane lateral force is near zero on both, showing that there is a clear asymmetry in the wake. This also highlights the difficulty of correlating the velocity field with the forces for smooth sphere case with random forcing: the streamwise cut of the vector field is not only dependent on the in-plane force, but also the out-of-plane force. Even so, the general trend for the smooth sphere case is the same, with a smaller wake when the in-plane

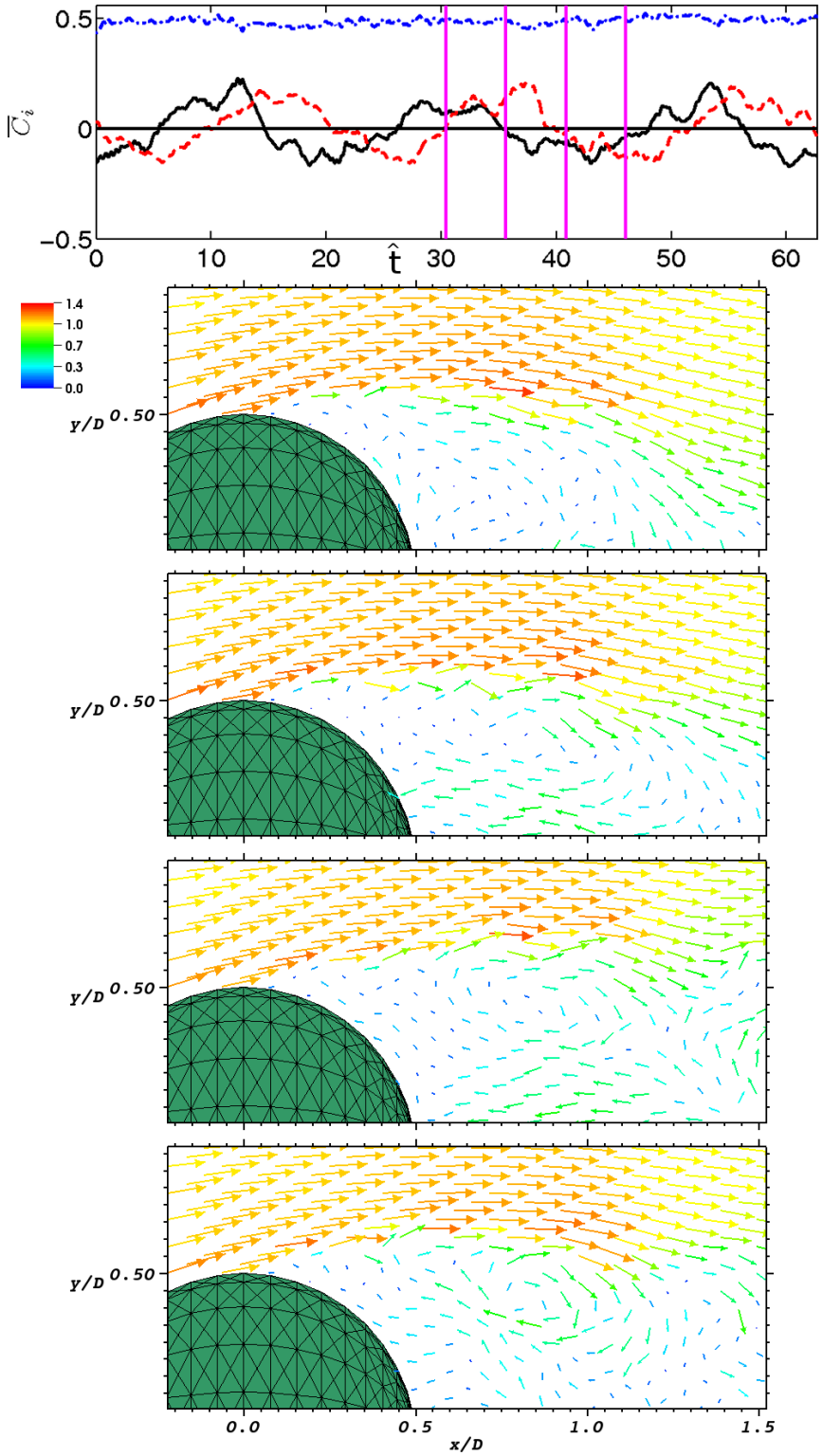

Figure 5.6: Time trace of the forces along with four instantaneous velocity fields equally spaced over one stud revolution (indicated by vertical line on force history), with the stud moving at $\omega^* = 0.15$. The vector field is in the x-y plane, and the forces are marked as C_x (-·-); C_y (–); C_z (- -).

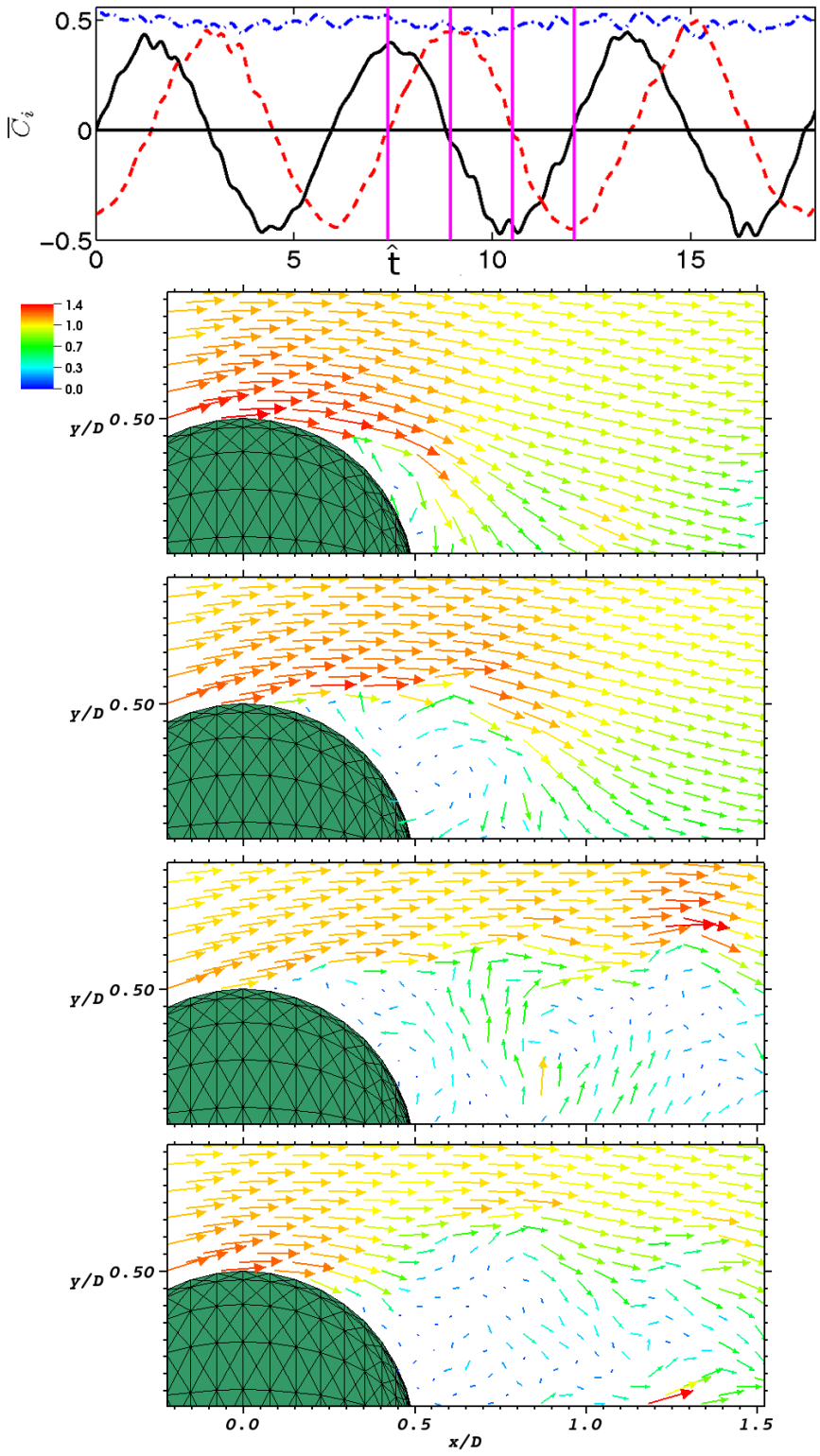

Figure 5.7: Same as figure 5.6, except with $\omega^* = 0.52$.

force is large (chapter 3).

When the angular frequency of the stud is increased to $\omega^* = 0.89$ (figure 5.8), the lateral forces decrease, but at the same time the mean Reynolds stresses are increased (as was seen in figure 5.5). At this speed the recirculation region is essentially gone when the in-plane force reaches a maximum. This is not to say that the flow does not separate; with the wide field of view this cannot be precisely determined. Another feature is that the stud is almost on the opposite side of the sphere ($\theta_k = 162^\circ$) when the in-plane force is a maximum.

The instantaneous velocity fields suggest the physical mechanism which is responsible for both the variation in the mean lateral force (figure 5.3) and the hot-film results (figure 5.4a). Examining a full time series (not shown), it was found that the hot-film reading was highly correlated with the local position of separation. This holds for all of the stud speeds examined, with small variations in the predicted and actual azimuthal angle of the smallest wake, indicating that three-dimensional effects in the wake do not need to be taken into account when interpreting the hot-film data. As an example, consider the $\omega^* = 0.15$ hot-film result in figure 5.4a, which could be interpreted in the following manner: immediately after the stud passes, the separation point begins to move downstream, reaching a maximum streamwise angle when the hot-film voltage is a minimum, and then very gradually returning to the initial separation angle. Note that the separation angle is not being measured, though the trends in the PIV data are clear.

The variation in the magnitude of the mean lateral force (in the stud reference frame, figure 5.3) has an analogous interpretation as that of the hot-film results. At low speeds, the wake is only slightly altered by the passing stud. As the speed is increased, the minimum size of the wake continues to decrease, and at the same time the azimuthal extent is increased. When the maximum lateral force is produced, there is a local region where there is no detectable wake. As the speed is increased further, the azimuthal extent continues to increase, but at the same time the wake on the opposite side begins to decrease in size due to increased fluid entrainment (as is evident in figure 5.4a, or from the progression of the velocity fields, which are not shown), thus partially canceling out the effect.

Although a planar cut of the flow field yields significant insight into the forcing, it will be shown in the next section that the position of the separation is inextricably linked to vortical structure in the wake.

5.2.5 Phase-Averaged Flow Field

Since the flow field is dominated by the position of the moving stud, it is possible to find a phase-averaged flow field. The azimuthal angle was divided into 100 bins, and each velocity field was placed in one of the bins based on the simultaneous measurement of the stud position. In order to average over the random variations in the wake that were not associated with the stud, time resolved PIV images were acquired for at least 12 stud revolutions per stud speed. Averaging over the velocity fields in each bin yielded 100 velocity fields, each corresponding to a different azimuthal distance from the stud.

Figure 5.9 shows two of these phase-averaged plots for the faster $\omega^* = 0.89$ run, $\hat{t} = 1$ and 1.6 after the stud has passed, with the separation point just beginning to move downstream. To highlight the structure in

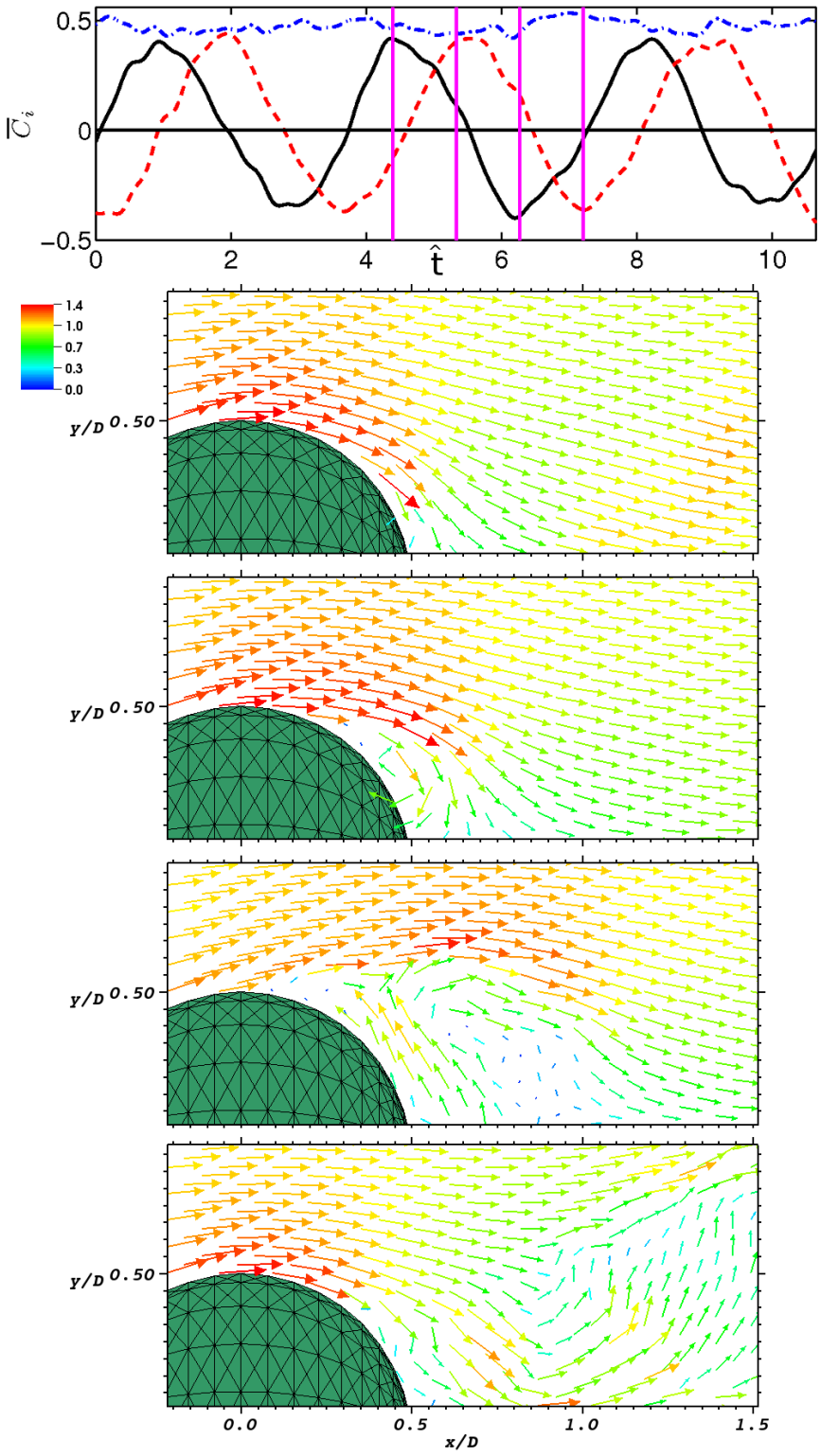

Figure 5.8: Same as figure 5.6, except with $\omega^* = 0.89$.

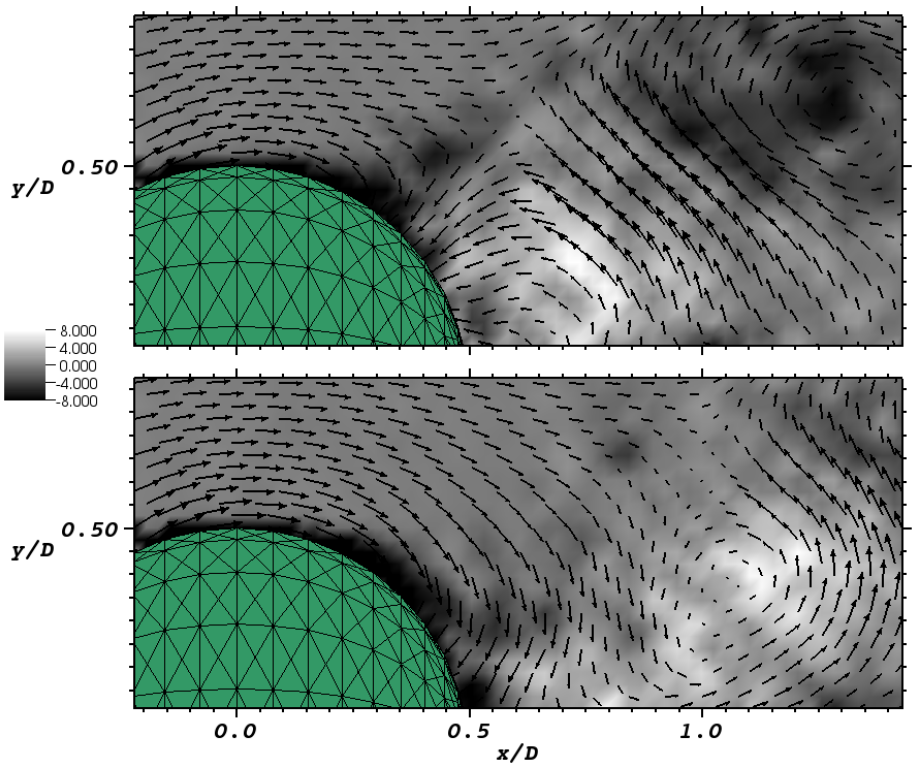

Figure 5.9: Phase averaged velocity fields with $0.6U_\infty$ subtracted off, with roughness element moving at $\omega^* = 0.89$. Grayscale shading indicates value of dimensionless vorticity. The stud is at 65° in the top image and shows a negative vortex on the top right, and a positive vortex forming behind the sphere. In the bottom image the stud is at 100° and the positive vortex is now fully formed.

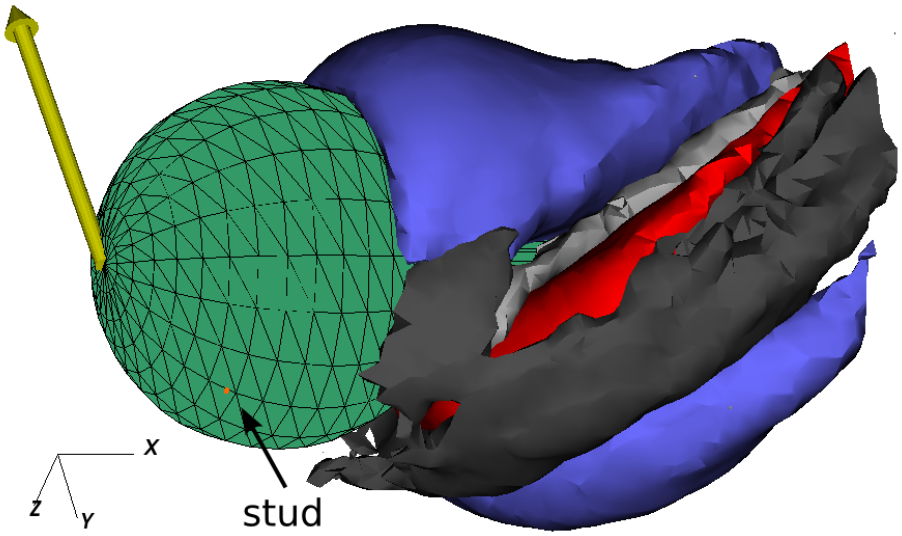

Figure 5.10: Three-dimensional phase-averaged flow field, with roughness element moving at $\omega^* = 0.89$. Azimuthal vorticity contours are -3 (dark gray) and $+3$ (light gray). Radial velocity contours are -0.2 (blue) and $+0.4$ (red). The lateral force vector is attached to the front of the sphere.

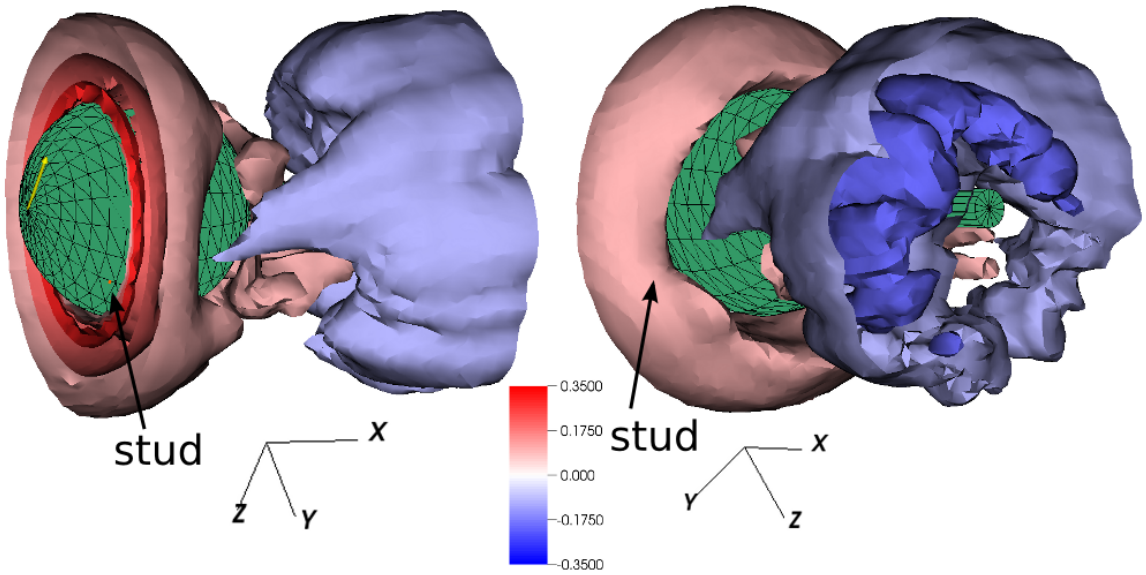

Figure 5.11: Angled views showing the radial component of the phase-averaged wake, with $\omega^* = 0.15$. Contours are of the normalized radial velocity: -0.2, -0.1, 0.1, 0.2, 0.3, 0.4.

the wake, $0.6U_\infty$ was subtracted from the streamwise velocity, and the vorticity that is normal to the image is indicated using grayscale shading. This shows a pair of very clear counter-rotating vortices, and hints at some very rich structure in the wake. In terms of the radial velocity, U_r (where r is in the lateral force plane, and is the distance from the sting), there is a large positive U_r in between the two vortices, with negative U_r on either side. This radial velocity will be used to help interpret the structure in the wake.

To gain a better understanding of the wake structure, the phase-averaged three-dimensional wake was reconstructed out of the U_r and U_x velocity components (U_θ is not available from the planar data). This was possible because the sphere is symmetric, with the only important variable being the position of the PIV plane (always at $\theta = 0°$) compared with the position of the stud. Thus, when the phase-averaged stud position is located at 20°, the phase-averaged velocity field is $-20°$ from the stud. In this way the three-dimensional phase-averaged wake was constructed, with the stud chosen to be at $\theta = 0°$.

Figure 5.10 shows both contours of radial velocity (in red and blue) and azimuthal vorticity (grayscale). The vorticity contours lie in between the positive and negative velocity contours, indicating that the radial velocity provides a reasonable indication as to the location and shape of the counter-rotating vortices. The azimuthal vorticity does not provide a good indication of the structure in the wake at lower stud speeds, because the vorticity is then mostly aligned with the streamwise direction. Thus, the radial velocity will be used to highlight the structure in the wake as a function of stud speed.

Figures 5.11 – 5.15 show contours of the phase-averaged radial velocity for several different stud speeds. Both a front and a back angled view are shown, with the approximate position of the stud indicated. The orientation and contour levels are the same for all plots, and were chosen in an attempt to highlight the

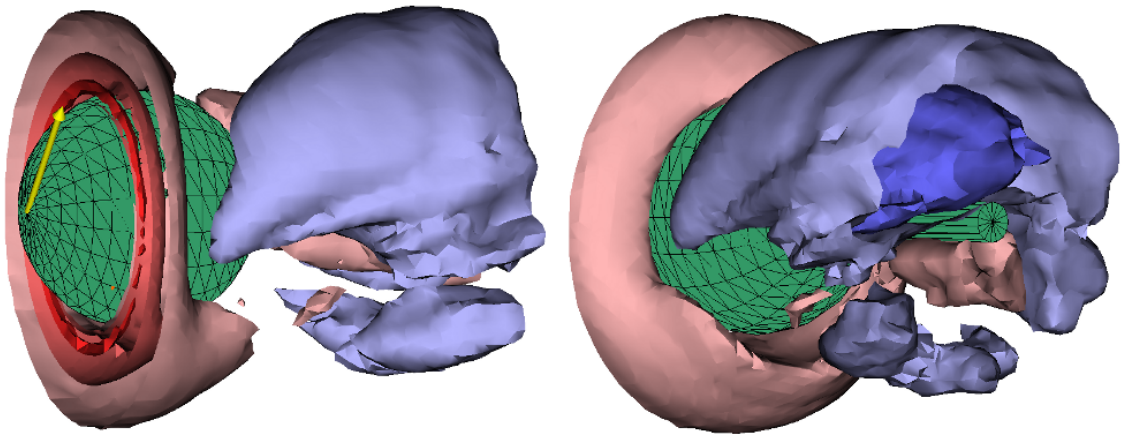

Figure 5.12: Same as in figure 5.11, with $\omega^* = 0.34$.

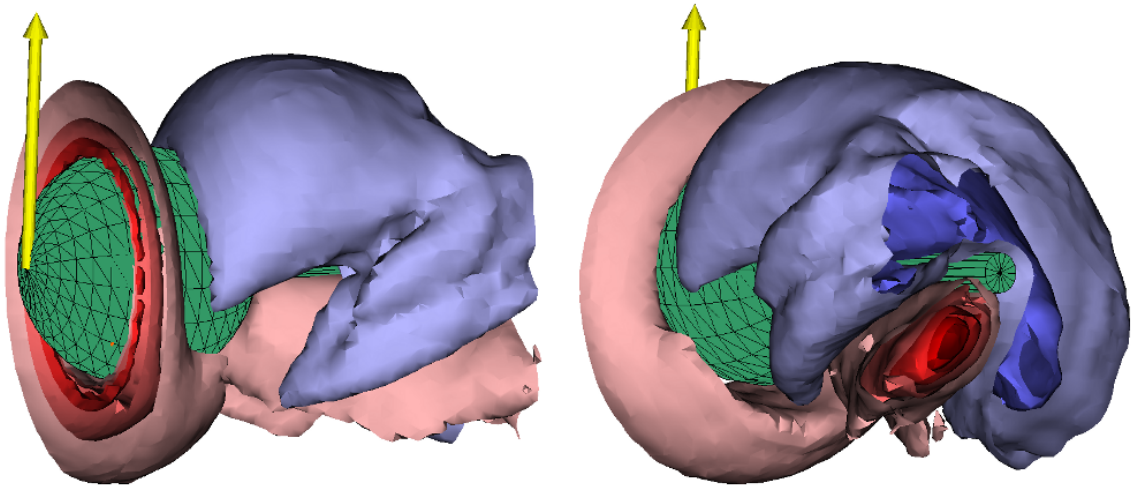

Figure 5.13: Same as in figure 5.11, with $\omega^* = 0.52$.

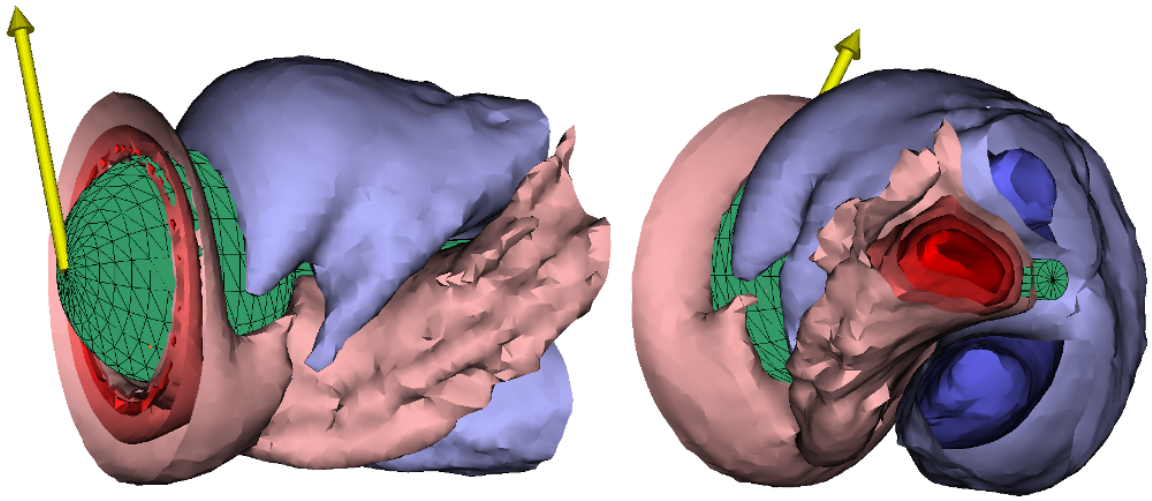

Figure 5.14: Same as in figure 5.11, with $\omega^* = 0.70$. Note the high speed positive velocity fluid, with negative U_r fluid on either side, indicating counter-rotating vortices in the shape of a helix.

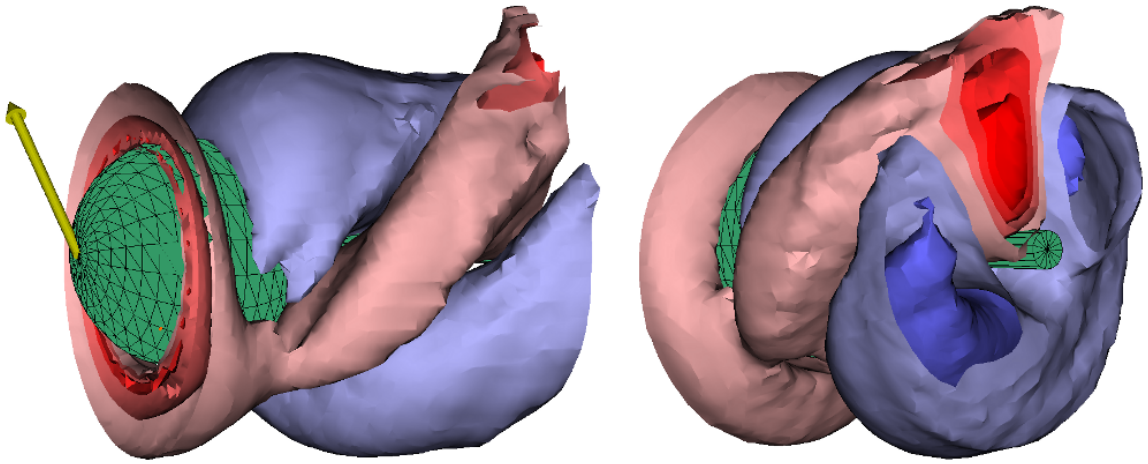

Figure 5.15: Same as in figure 5.11, with $\omega^* = 0.89$.

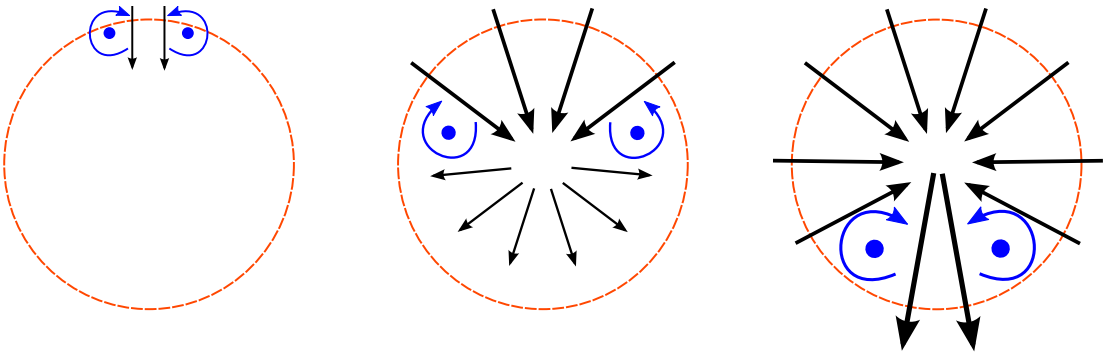

Figure 5.16: Schematic simplification of a spanwise cut of the near wake, showing the progression of the counter-rotating vortices as the region of influence of the stud increases: (a) the stationary stud produces vortices which push each other toward the center, (b) vortices move away from each other and (c) meet on the opposite side, now pushing each other away from the center.

vortical structure. In addition the lateral force vector (which corresponds to the phase-averaged force when the stud is at $\theta = 0^\circ$) is shown on the front of the sphere, and has the same scale between figures.

The average wake for the lowest speed (figure 5.11) is mostly symmetric, with a small change in the wake due to the passing of the stud (which is moving clockwise as viewed from upstream) indicated by the streak of negative U_r and also by the decrease of positive U_r near the equator, both due to a local change in the position of separation and the size of the wake.

When the angular frequency is increased to $\omega^* = 0.34$ (figure 5.12), the extent of the affected area is increased, and from the downstream view some of the fluid has a negative velocity of greater than $0.2U_\infty$ directly next to the sting, indicating that the fluid passes from the upper to the lower plane, with the sign of its velocity changing.

In figures 5.13 – 5.15 the stud frequency is greater than $\omega^* = 0.52$ and there is a clear signature of the counter-rotating vortices, following a helical path. As the stud moves faster, the streamwise period of the helices gets shorter. Note that in all cases the orientation of the structure in the wake is well correlated with the position of the stud.

The orientation of this helical vortex pair is such that it would induce a velocity field (due to the azimuthal vorticity) that would contribute to locally keeping the sphere boundary layer attached further downstream. For comparison, the effect of a trip wire in the subcritical regime is to keep the flow attached until about 120°, leaving a recirculating region behind the sphere (Bakić, 2004). Thus it is possible that tripping the boundary layer alone would keep the flow attached to about 120°, while the addition of the large scale vortices in the wake locally cause the flow to not even separate (as in figure 5.8).

A simplified two-dimensional schematic is shown in figure 5.16 to illustrate a possible mechanism that leads to the production of the counter-rotating vortices. The views are of a spanwise cut of the near wake, ignoring three-dimensionality. The dashed circle represents the center of the shear layer for the base flow,

and the arrows represent the change in the shear layer caused by the stud, with each view oriented such that the force is in the +y direction. For a stationary stud (figure 5.16a), it was argued in chapter 4 that increased entrainment locally causes the flow to stay attached slightly further downstream than for the rest of the flow, producing weak counter-rotating vortices, such that they push each other toward the sting. As the stud begins to move at low speeds (figure 5.16b), an extended region of the flow becomes tripped, causing the flow to remain attached over a larger portion of the sphere, with the inward moving fluid being forced into the un-tripped region, again producing two counter-rotating vortices, that are stronger and further apart. Finally, as the stud is moving fast compared with the timescale associated with the movement of the separation location (figure 5.16c), most of the flow remains attached to the sphere, causing fast moving fluid to be forced into the only region that has not been tripped, producing two very strong counter-rotating vortices with mutual induction away from the center (similar to supercritical flow with a stationary stud), as opposed to toward the center. This is of course a very simplified explanation, because the flow not only moves out of plane, but the time-dependence of the disturbance also produces the helical shape, which influences the dynamics of the separation.

5.3 Shaped Trajectories

In order to gain further insight into the flow, the following sections briefly examine the effect of an oscillating stud, the effect of shaping the stud trajectory, and the step response of the flow to a change in the stud's angular frequency.

5.3.1 Oscillating Roughness Element

To demonstrate that it is possible to produce a mean lateral force, the stud was oscillated about the y-axis ($\theta = 0^\circ$), with varying frequency and amplitude (figure 5.17). The general trend is that as the frequency or amplitude of the oscillations increase, so does the mean side force, providing more evidence that the stud locally alters the separation point. The low amplitude, low speed oscillations of the stud produced a mean side force of about 1.8 times larger than what was produced by a stationary stud, whereas the high amplitude, high speed mean oscillations caused a side force that was about 4.6 times larger. However, when a trip-wire was placed over half of the sphere a mean side force of $C_y = 0.38$ was produced, which indicates that there is still a large margin for improvement, especially considering that a dynamic surface was shown to produce structure in the wake, which could possibly be taken advantage of to produce an even greater side force.

5.3.2 Velocity Profile Shaping

Figure 5.18 shows the effect of shaping the trajectory of the stud such that ω^* depends only on θ, with the intent of producing a mean side force without changing the direction of rotation. For the constant frequency

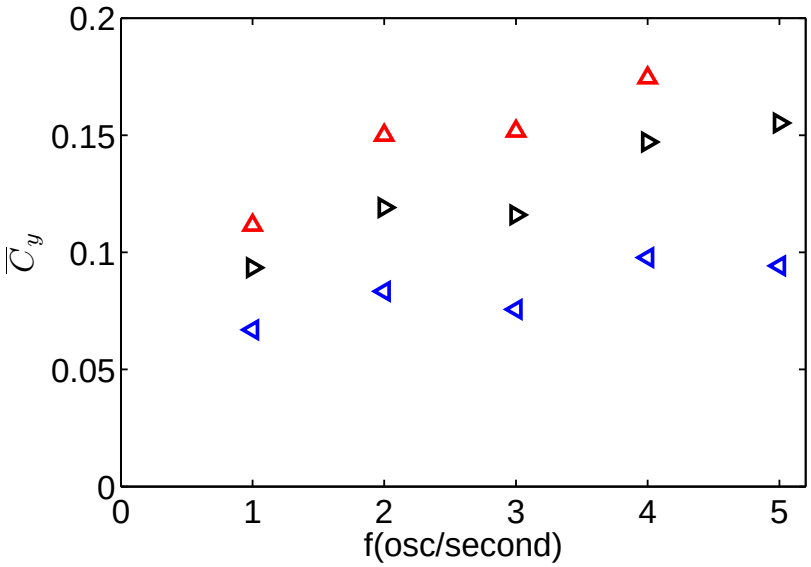

Figure 5.17: Mean lateral force ($\overline{C}_y$), with stud oscillating about $\theta = 0°$, with amplitude: $\pm 40°$ ($\triangleleft$); $\pm 60°$ ($\triangleright$);$\pm 80°$ ($\triangle$). $\overline{C}_x$ and $\overline{C}_z$ were not notably changed.

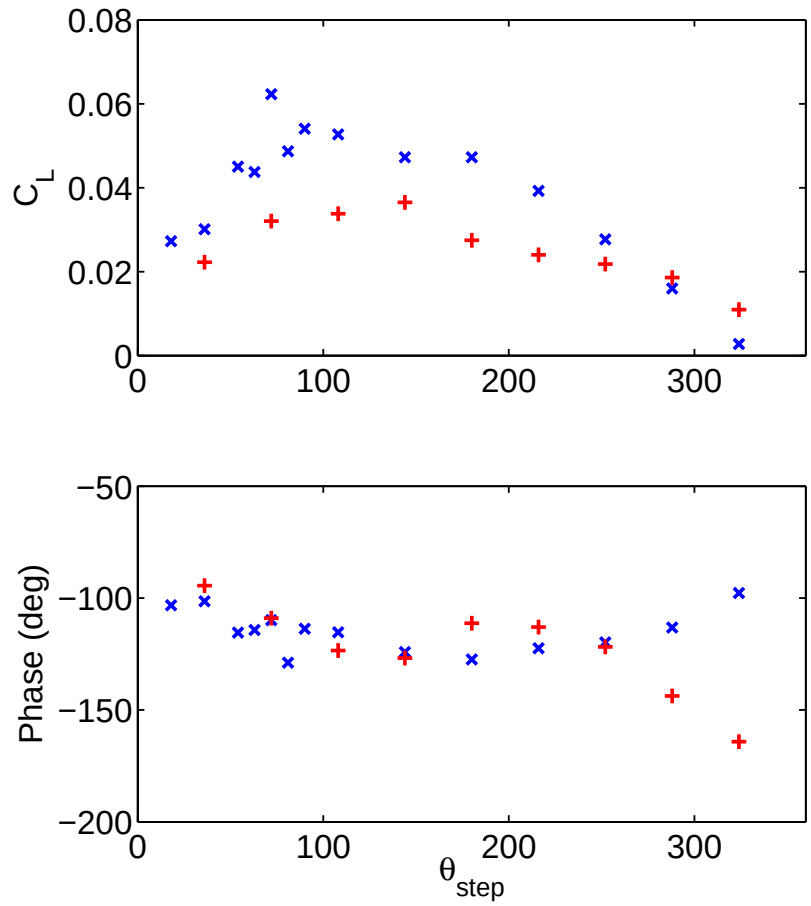

Figure 5.18: Shaped trajectories, with a step up in angular frequency at θ_{step}, and a step back down at $\theta = 0°$: ω^* =0.17-0.55(x); 0.34-0.55(+).

case a fast moving stud produces a large lateral force, while a slow-moving stud produces a small lateral force. This indicates that it should be possible to obtain a mean lateral force with the stud moving in just one direction, by varying its speed. To verify this, the stud frequency was set to a constant, small value ($\omega^* = 0.17$ or 0.34) at $\theta = 0^\circ$, then at θ_{step} it was increased to $\omega^* = 0.55$ (figure 5.18). The step response of the motor was not instantaneous, so the LQR preview controller was used to smooth out the step and produce an optimal transition without overshoot. The mean lateral force and phase are plotted, where the phase is taken to be the angle between the center of the low frequency region ($\theta_{step}/2$) and the mean lateral force vector.

The largest mean lateral force occurs approximately when the stud is moving slowly for a 90° span, and quickly for the rest. When it is moving slowly the local separation point is not significantly changed. However, if too much time is spent on the low speed side, the delayed separation begins to move back upstream on the high speed side of the sphere. The magnitude of the mean lateral force is similar to that of the oscillating stud that has a frequency of 1Hz and covers a span of $\pm 40^\circ$. This is not very large, but the non-constant angular frequency gives insight into the dynamics. Note that the significant scatter in the data is due to the forces being very small ($C_L = 0.01$ corresponds to 3mN). This has a big effect on estimating the angle to the mean force, when the force is small.

The angle to the mean force generally points about -120° away from the center of the low frequency region (figure 5.18). This clearly points to an effect of three-dimensionality, as the direction of rotation is important.

One example of a shaped trajectory is shown in figure 5.19a, corresponding to a step from $\omega^* = 0.17$ to 0.55 at 90°, and a step back down at $360^\circ/0^\circ$. Both the phase-averaged force and the angular frequency (scaled by a factor of two) are plotted against the position of the stud, demonstrating precise control of the stud trajectory, and a difference in the orientation of the force trajectory and the stud frequency, due in part to the time delay associated with the movement of the separation location.

The lateral force and phase as a function of stud speed are compared with the constant frequency results in figure 5.19b. The range of the phase for the constant frequency case, between $\omega^* = 0.17$ and 0.55, is not very large, and neither is the range for the shaped trajectory. On the other hand, the lateral force for the constant frequency case changes significantly, and so does that of the shaped trajectory. The large open symbols are the same in figures 5.19a and 5.19b, and show the direction of the hysteresis. Starting at the bottom left of the rectangle (adjacent to the open circle in figure 5.19b): the force is small when the stud speed quickly increases. When the stud has reached the higher speed, the force gradually increases. While the stud slows down there is little change to the force, and then at the low speed the lateral force gradually decreases again. This is explained by the dynamics of the attachment region: the stud produces a local disturbance that excites the instabilities in the flow, which gradually locally change the location of separation. It is this time delay which causes the hysteresis.

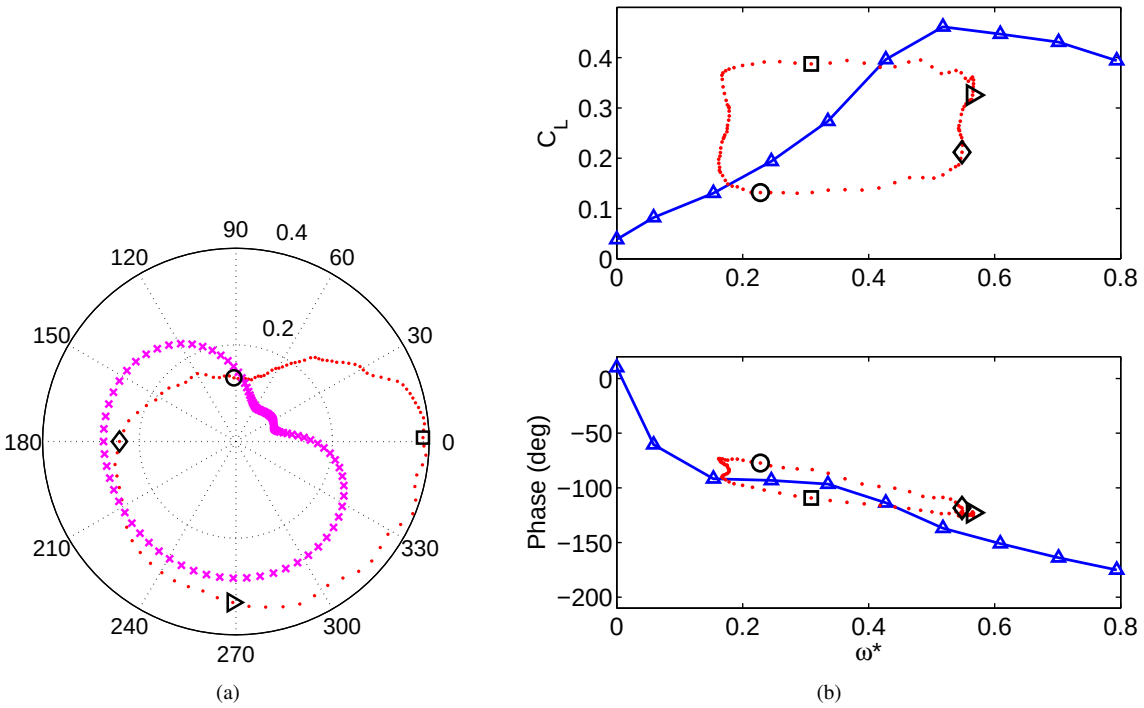

Figure 5.19: Shaped trajectory corresponding to a step from $\omega^* = 0.17$ to 0.55 at 90°. (a) The angular coordinate is the stud position, with the stud moving counter-clockwise: Phase-averaged force (...); $\omega^*/2$ (x). (b) Mean C_L and phase $(\theta - \theta_k)$ vs. constant frequency ω^* results for $Re = 0.5 \times 10^5$ (△), compared with the current trajectory.

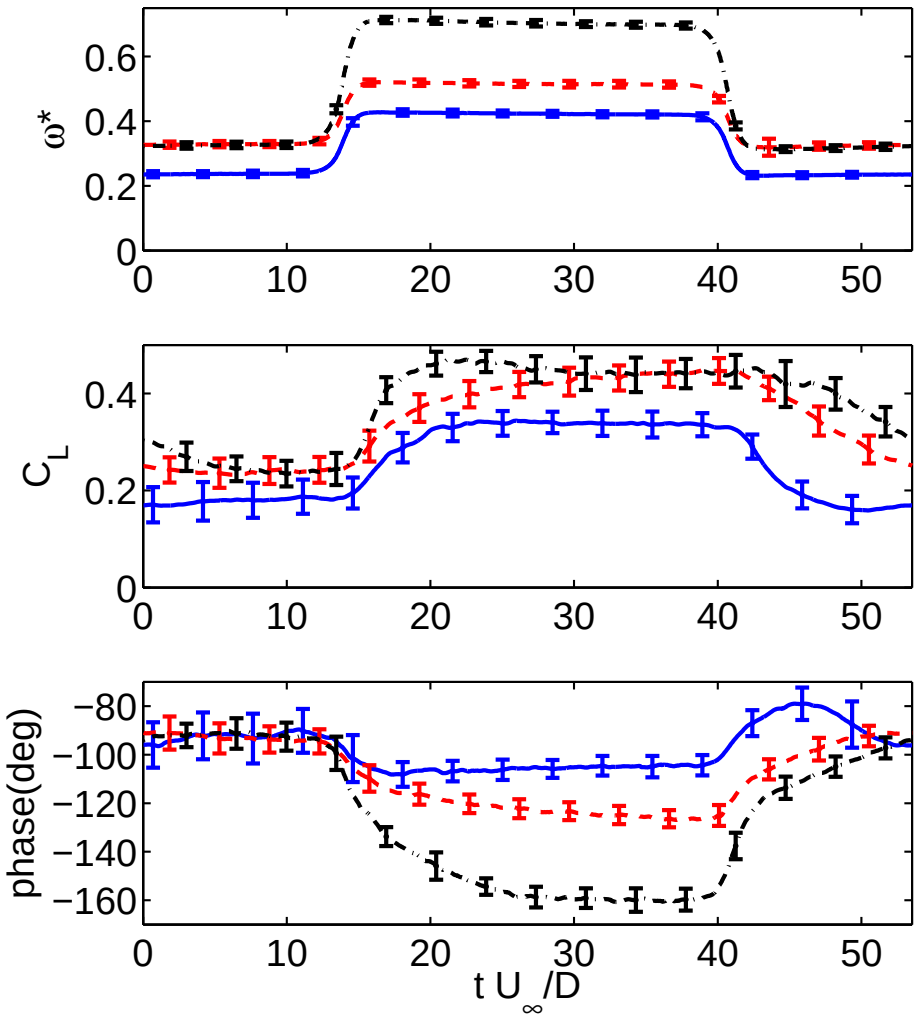

Figure 5.20: Three mean step responses, each averaged over 120 periods, with the error bars indicating $\pm\sigma$.

5.3.3 Effect of a Step in Angular Frequency

Figure 5.20 shows a preliminary investigation of the step response, which is useful in examining the time response of the system due to a step change in the actuation frequency. Here, the motor "step" in frequency takes about $\hat{t} = 3$, where the frequency step is a function of time, as opposed to θ as in the previous section. This is slightly faster than the $\hat{t} \approx 4$ for the separation point to move to its furthest downstream position after the stud passes. The results are an average over 120 periods, with the error bars indicating $\pm\sigma$. The variation of the motor speed from one period to the next is very small, while that of the lateral force and phase are large. This standard deviation of the forces is close to that for the no-stud case ($\sigma = 0.5$, chapter 3), indicating that they are of similar origin, with the random fluctuations of the wake superimposed on top of the effect due to the stud. Thus, for control purposes, it is not possible to say what force a certain stud trajectory will produce, only what force it will produce on average.

This plot indicates some of the interesting dynamics that could be exploited with a control scheme. For example, the response time of the wake to an increase in frequency is much faster than the response time to a decrease, for all three steps. This is explained by the hot-film results (figure 5.4) for the lowest stud speed, which showed a peak response to the passing of the stud after $\hat{t} \approx 5$, while the decay back to the base flow took $\hat{t} \approx 30$. Another interesting feature is the overshoot of the phase lag for the smallest step down, and also the slow change in the phase for the largest step up. This rich behavior not only opens up a lot of possibilities for a control scheme, but also makes the problem very challenging.

5.4 Summary

The effect of a time-dependent perturbation to the surface of a sphere was examined by varying the position of a roughness element in real time. It was found that this produced a significant change in the flow field, much larger than that caused by a stationary stud. This was linked to the long timescale associated with the dynamics of a changing separation line. Hot-film and particle image velocimetry results revealed that after the stud passed by the streamwise measurement plane, the local position of flow separation gradually moved downstream, reaching a maximum downstream position after about $\hat{t} = 4$, and then slowly returning back to the initial position of separation. This timescale was nearly independent of stud speed, and the effect was attributed to an excitement of the boundary and shear layer instabilities, which increases fluid entrainment and keeps the flow attached, with the azimuthal extent at any given time being dependent on the speed of the stud.

It was found that an instantaneous lateral force as large as the drag was produced when the dimensionless angular stud frequency was $\omega^* \approx 0.5$. This is close to a subharmonic of the wake instability, which Chomaz *et al.* (2006) referred to as the helical instability. PIV and hot-film revealed that this maximum force was produced when the flow separated near the back of the sphere in the streamwise plane associated with the force direction (the "first" side), and near the equator on the opposite side (the "second" side). At lower stud speeds, the flow does not remain attached as far downstream on the first side, yet it still separates near the equator on the second side, leading to a smaller force. At higher speeds, the local separation point cannot move any further downstream on the first side, and on the second side the separation near the equator begins to move downstream, canceling the effect.

The time-dependence of the stud position produces a coherent structure in the wake, which is dependent on the stud speed. A planar PIV velocity field in the streamwise/radial plane revealed two counter-rotating vortices with a mutual induction that moved them away from the sting. Because the flow field is strongly dependent on the stud motion, it was possible to construct a phase-averaged velocity field based on the angle between the stud and the PIV plane. Only two of the three velocity components were measured, but the structure of the wake can be visualized using just the radial (distance from the sting) velocity component. By relating the three-dimensional radial velocity contours to the counter-rotating vortices, it was determined that

these vortices form a helical shape. The orientation of these vortices was such that the induced velocity field would help to locally keep the flow attached to the sphere.

The production of the counter-rotating vortices was described using a simplified two-dimensional schematic, showing that at near zero speed the vortices are formed with mutual induction toward the sting. As the extent of the boundary layer trip is increased, these vortices move away from each other and meet on the opposite side of the sphere, with the mutual induction now away from the sting.

Finally, the effect of non-constant stud trajectories were briefly explored. It was demonstrated that a mean side force could be obtained by oscillating the stud about a point, in the azimuthal direction. A mean side force of almost five times that of a stationary stud was achieved by moving the stud between $\pm 80^{\circ}$ at a frequency of 4Hz. The mean force due to a trip wire being placed over half of the sphere was almost twice as large, indicating that a larger mean side force would be achieved by oscillating the stud at a higher frequency. In addition, it was also shown that it is possible to get a small mean side force by preferentially changing the speed of the stud depending on its position, without completely changing directions as with the oscillating stud.

Chapter 6

Conclusion

An experimental apparatus was designed which allowed for the examination of the effect of small amplitude time-dependent changes to the morphology of a sphere. A true morphing surface was approximated by moving a small roughness element (a "stud"), which was only 1% of the sphere diameter, along the surface in the azimuthal direction. The trajectory of the stud was controlled with a motor located inside the sphere, which had a magnet attached to the end of an arm, pulling the stud along the sphere surface as the motor shaft rotated. In addition to surface actuation, simultaneous three-component force measurements and particle image velocimetry were utilized to understand the effect of the actuation on the flow. Due to the limited amount of data in the literature on the unsteady forces on a sphere, both the nature of the forcing on a smooth sphere and the effect of an isolated roughness element were studied before performing the dynamic stud tests, in order to have a base for comparison.

6.1 Summary and Major Findings

The flow over a smooth sphere was examined both in the subcritical and supercritical regimes. It was found that the spectra had significant energy at frequencies well below the vortex shedding frequency, which corroborated the numerical findings of Yun *et al.* (2006) and Constantinescu & Squires (2004). Based on the observation from the dynamic stud runs that there is a relatively long timescale associated with the separation dynamics, it was proposed that a similar mechanism is responsible for the smooth sphere low-frequency forcing. In addition, long data sets were recorded that allowed for the examination of the convergence of the statistical properties of the forces. It was found that the flow must be investigated for at least $\hat{t} = 500$ to get converged results of the mean and standard deviation, and longer for higher-order statistics. Based on the observation that the unsteady lateral forcing had a Gaussian distribution, a simple model was developed to mimic the lateral forces, using an analogy with a two-dimensional harmonic oscillator.

The effect of an isolated roughness element was examined over the same Reynolds number range, and it was found that in general, the stud produced a maximum lateral force when it was position between a streamwise angle of 40° and 80°. In addition, the subcritical lateral force vector pointed in the direction of

the stud, while in the supercritical regime the sign of the force changed. PIV was used to understand the physical mechanism behind this change, and as hypothesized the stud caused the subcritical wake to separate further downstream (locally), and the supercritical wake further upstream. In the supercritical regime the small stud produced a tilted and much larger wake, leading to a lift-to-drag ratio of almost one. It was proposed that for the subcritical regime, the stud produces a pair of streamwise counter-rotating vortices in the near wake, with mutual induction toward the sting. This mechanism may also form an important part of the dynamics for flow over a smooth sphere, but on a smaller scale.

Moving the stud along the surface of the sphere in the subcritical Reynolds number regime produced dramatic results, quite different from the findings for the stationary stud. The reason for the large effect was due to the long timescale associated with the dynamics of the separation line. It was proposed that the passing stud locally perturbed the boundary layer and free shear layer, exciting instabilities and causing enhanced entrainment, which lead to delayed separation. Hot-film and PIV measurements revealed that the dimensionless time until the advancement of the separation point stopped after the stud had passed was about $\hat{t} = 4$. This was fairly independent of the angular frequency of the stud, with the retreating separation point taking longer to return to the base separation location. This long timescale allowed the moving stud to influence a large azimuthal extent of the boundary layer. This lead to instantaneous lateral forces as large as the drag, due to the boundary layer separating asymmetrically. A simplified schematic was proposed to illustrate the progression of the wake structure as the dimensionless angular stud speed was increased, arguing that counter-rotating vortices, with mutual induction similar to that of the supercritical case, were formed at the higher speeds. Due to the time-dependence of the stud, the vortices formed a helix in the wake, oriented such that the induced velocity field helped keep the flow attached further downstream. Additionally, by oscillating the stud about a point it was demonstrated that a mean side force could be produced, which was about 5 times larger than that caused by a stationary roughness element.

6.2 Future Research

The new experimental apparatus proved to be an ideal setup for testing the effect of small amplitude changes to a surface. Therefore, it is suggested that morphing surfaces be tested using the same setup. However, because the flow is so sensitive to small changes in the sphere surface, extreme care must be taken to mount the actuator such that it forms a continuous, smooth surface in the unactuated state.

Further investigations using the present setup would be useful. Particularly, well-resolved stereo PIV of the separation region could yield insight into the dynamics of separation. Smoke visualization could also help verify the role-up. Additionally, hot wire measurements of the perturbed boundary layer at different streamwise locations would provide a more detailed understanding of the amplification of the perturbation from the stud.

If a morphing surface can be produced that covers the azimuthal extent of the sphere near a streamwise

angle of 60°, it would be useful to compare the effect of both uniform and asymmetric perturbations of the boundary layer with the present results. In particular, it may be possible to introduce an actuation pattern (both spatially and temporally) that optimizes the vortical structure in the wake, such that a mean lateral force could be achieved that is larger than that produced by simple periodic actuation of one side of the sphere. This observation comes from noting the significant effect caused by the helical vortices in the present experiments.

Finally, the effectiveness of perturbations produced using a morphing surface near the separation of a stalled airfoil should be compared with other methods, such as blowing and suction, to verify similar performance, with a view to developing a simple, cost effective actuation method for the control of separation and the shaping of the force trajectory.

Appendix A

Effect of Sting Size at Subcritical Reynolds Numbers

This material was presented at the 2008 AIAA Fluid Dynamics Conference (Norman & McKeon, 2008).

A.1 Overview

Vortex shedding and turbulent motion in the wake of a sphere that is supported using a streamwise-aligned cylindrical sting are investigated at a subcritical Reynolds number of Re=3800, using high speed particle image velocimetry. The mechanism by which the presence of a sting of increasing diameter relative to the diameter of the sphere influences the wake, in terms of both the small-scale shear instability and the larger wake instability, is explored and briefly compared with the two-dimensional analog of the splitter plate introduced into a cylinder wake. The difficulties associated with obtaining converged statistics, along with the effect of free stream turbulence and sphere vibrations are detailed. An understanding of the mechanism by which the blockage, or interference, arising from the presence of the sting influences cross-wake communication and downstream development is a necessary precursor to studies of active control of the wake using surface actuation on a sting-mounted sphere.

A.2 Introduction

Whereas there have been numerous investigations on the effect of an obstructing, or splitter, plate on the development of the wake behind a cylinder, there has been less study of the weak analog for a three-dimensional axisymmetric bluff body, namely the influence of a cylindrical support sting on the development of the wake behind a sphere. While an interesting problem in its own right, identification of the effect of a finite-sized sting on both the shear layer that is shed from the sphere and the downstream wake is a necessary precursor to detailed studies of active control of the sphere boundary layer (i.e., experiments in which a tether mount is less desirable than a rear sting), with a view to manipulating the magnitude and direction of the resultant

forces on the sphere.

For sphere Reynolds numbers (where $Re = \rho U_\infty D/\mu$ is based on sphere diameter D, free stream velocity U_∞, density ρ, and dynamic viscosity μ) above approximately 800 and below the critical Reynolds number for transition of the sphere boundary layer, $Re \approx 3 \times 10^5$, frequencies corresponding to both a small-scale shear layer instability and a larger wake instability are present in the wake, while below this lower limit only the larger scale is observed (Sakamoto & Haniu, 1990; Kim & Durbin, 1988; Bakić & Perić, 2005; Achenbach, 1974*b*). With increasing Reynolds number the Strouhal number ($St = fD/U_\infty$, where f is the frequency) of the shear instability increases as Re^n, with $0.5 \leq n < 1$ for $10^3 < Re_D < 10^5$ (Kim & Durbin, 1988), while the large-scale Strouhal number remains approximately equal to 0.2, typical of vortex shedding. In the subcritical regime, computational studies (Yun *et al.*, 2006; Constantinescu & Squires, 2003) have also found a low frequency motion of the wake, below that of the large-scale vortex shedding frequency.

The ratio of sting diameter to sphere diameter, $\chi = D_S/D$ (figure A.1), in the cited experimental studies ranges from 0.055 to 0.15, indicating an unwritten rule of thumb for the size of the sting for minimal interference on the wake. However, Hoerner (1935) investigated the effect of χ on the drag coefficient and found a negligible effect on the subcritical drag and on the Reynolds number of transition, whereas the drag decreased with increasing χ in the supercritical regime where the size of the wake is greatly reduced due to the boundary layer becoming turbulent before separation.

Flow over a cylinder has been heavily investigated, and here we review only a few examples of obstructing the wake of a cylinder. Roshko (1955) investigated the effect of a splitter plate, placed on the wake centerline and with varying length and distance from the downstream separation point on the cylinder, and found that for a length of 4-5D, communication between the opposing separated shear layers could be prevented and large scale, organized vortex shedding completely suppressed, with an accompanying decrease in cylinder drag. Unal & Rockwell (1988*a*,*b*) further investigated the wake formation region in the presence of a long plate placed a varying distance downstream of the cylinder, while Anderson & Szewczyk (1997) incorporated the effect of mild three-dimensionality, and Gerrard (1966) investigated the controlling effect of a plate that was normal to the flow.

In the case of the sphere, the mechanism by which obstructions affect the wake is less clear. On the one hand, a large sting may reduce cross-wake communication for the axisymmetric shear layer, but in order to do this the sting must present a large reduction in wake area. In this study, we seek to investigate the mechanism by which a sting affects the wake development.

A.3 Experimental Setup

The experiments were performed in the NOAH free surface water tunnel at the California Institute of Technology, which has a test section width of 0.46m, depth of 0.50m, and length of 1.6m. Uniform flow is achieved by employing honeycomb flow straighteners, turbulence-suppressing screens, and a four-to-one fifth-order

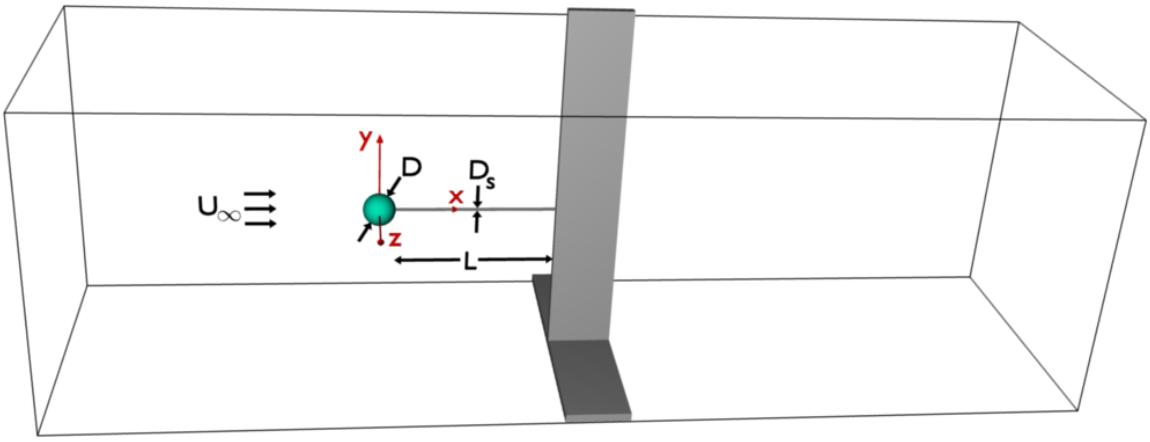

Figure A.1: Experimental setup showing test section, notation, and coordinate system

polynomial contraction (Gharib, 1983). The test section velocity range is between 0.03 and 0.40m/s and the sphere is centered in the test section, approximately 0.5m downstream from the end of the contraction.

The spheres were fabricated from polycarbonate, with a diameter tolerance of better than $\pm 0.0032D$, and a sphericity of better than $0.0025D$. The roughness height, k, is estimated to be less than 5μm, or a maximum $k/D < 2 \times 10^{-4}$, and the maximum area blockage ratio was less than 1%. Both blockage and roughness are expected to have negligible effect on the sphere boundary layer and wake development at the Reynolds numbers being investigated (Achenbach, 1974*a*), such that the influence of the sting size is effectively isolated.

The stings consisted of stainless steel rods with a straightness tolerance of better than 0.05%, and a diameter tolerance of better than $-0.0016D_S$. The minimum allowable rod diameter due to structural constraints was determined by estimating the angular misalignment of the sting to the oncoming flow due to deflections caused by gravity and unsteady fluid forcing using linear beam theory. The sting length was a minimum of eight times the diameter of the spheres under test (for comparison, Strouhal numbers in the wake of a cylinder were influenced by the splitter plate up to six diameters downstream (Roshko, 1955)).

High speed particle image velocimetry (PIV) was used to investigate planar cuts of unsteady flow over an axisymmetric body. A LaVision system consisting of a pulsed ND-YLF laser, a high speed camera with a 1-megapixel CCD and 10 bit depth, and a computer with a precision timing unit was used. The laser sheet was split and directed to enter the test section from the top and bottom. The laser sheets were aligned to the flow to within $\sim 1^\circ$, and to each other within 0.3°. This allowed illumination of the entire field of view even with the opaque sting, which was necessary for structural stability. Saturation of the CCD due to reflections was avoided by spray painting the spheres and stings black and carefully aligning the stings with the laser sheet.

The high frame rate elucidates the temporal evolution of the wake vortex dynamics, but it limits the amount of data that can be taken on the relatively slow large-scale wake shedding, due to memory limitations.

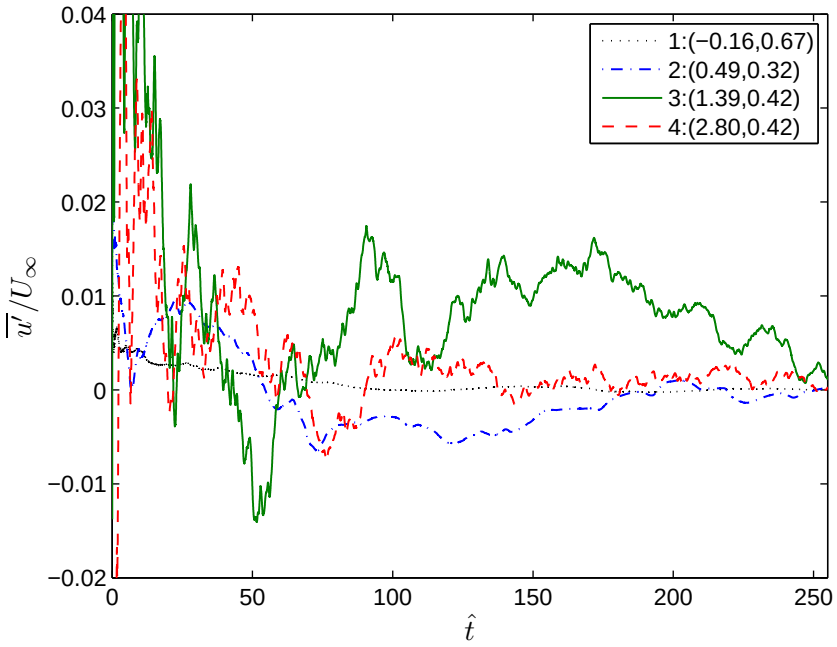

Figure A.2: Convergence of the streamwise velocity (1) outside wake, (2) behind sphere, (3) near max $\overline{u'u'}$, and (4) downstream in wake, for $D = 0.016$m and $\chi = 0.50$, with position indicated by (x/D,y/D)

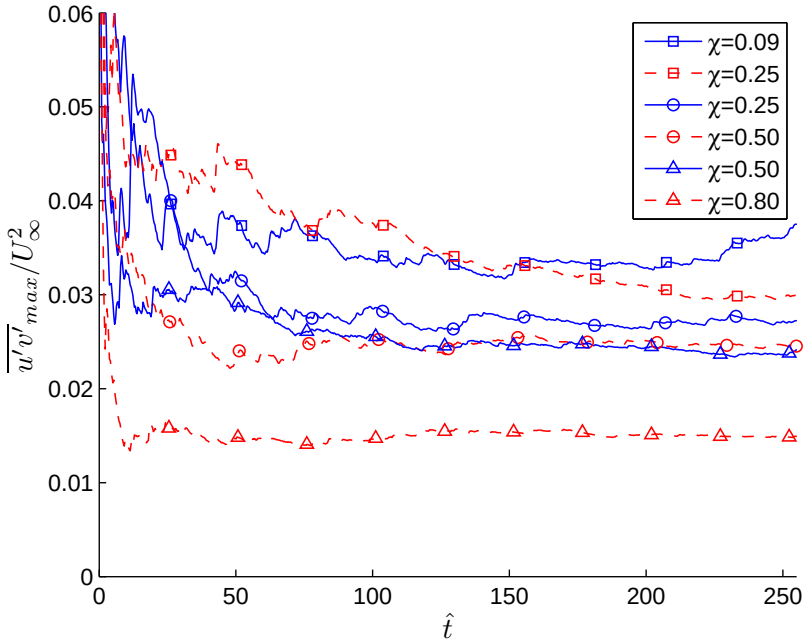

Figure A.3: Convergence of the maximum Reynolds shear stress in the wake, $\overline{u'v'}_{max}/U_\infty^2$. See table A.1 for symbols

Table A.1: Run conditions

$D(m)$	$U_\infty(m/s)$	χ	symbol
0.051	0.070	$0.09, 0.13, 0.16, 0.19, 0.25$	□
0.026	0.139	$0.25, 0.31, 0.39, 0.50$	○
0.016	0.223	$0.50, 0.60, 0.80$	△

In order to increase the total time of data collection, the laser pulse separation was increased as large as possible, to the point where further increase would lead to bad correlations due to out-of-plane velocity and a strong shear layer. This corresponds to a nondimensional pulse separation of approximately $\Delta\hat{t} = \frac{1}{St} = 0.016$, which will vary depending on laser sheet thickness and post-processing techniques. In comparison, the timescales of interest for $Re = 3800$ are approximately $\Delta\hat{t} = 0.9$ for the shear layer instability and $\Delta\hat{t} = 5$ for the wake instability. By minimizing the resolution of our images, we were able to collect continuous data for $\Delta\hat{t} = 260$.

The parameter space for this investigation included three different sphere sizes and five different sting sizes, which, taking into account the structural integrity of the stings, allowed for the range of χ shown in table A.1. The free stream turbulence, $\sqrt{\overline{u'u'}}/U_\infty$, was measured using PIV and found to be 1.7% for the smaller two spheres and 2.6% for the larger sphere, where $u'(t) = u(t) - \bar{u}$ is the fluctuating velocity at a point, and $\bar{u} = \frac{1}{N}\sum_{i=1}^{N} u_i$ is the mean at a point over all N samples. The larger free stream turbulence for the biggest sphere is likely due to flow unsteadiness at the low free stream velocity. The smallest sphere had low amplitude vibrations of less than $0.002D$, due to slight vibrations of the supporting mount at the higher speed. This was determined from the time series of images, and no vibrations were detected for the larger spheres. Previous researchers have shown that free stream turbulence (Bakić, 2004) and acoustic excitation (Kim & Durbin, 1988) can alter the wake development, so it is not expected that the results for the different sphere sizes will completely collapse for a given χ.

A.4 Results

A.4.1 Convergence

Taneda (1978) suggested that the wake of a sphere oscillates in a streamwise-aligned plane that rotates slowly and randomly about the sphere center. Hence, in order to obtain converged statistics using PIV, a significant number of wake oscillations must be averaged over such that the variations in the averaged wake quantities due to the random orientation of the plane tend toward a constant value. As shown in figure A.2, in areas of low turbulence, such as the outer flow and right behind the sphere, convergence is obtained rapidly, whereas in areas of high turbulence there are still significant fluctuations even though averages were taken over approximately 50 wake oscillations. Though it is difficult to determine using just a planar cut, it appears that there is a movement of the wake with a frequency lower than that of the wake instability. This was confirmed

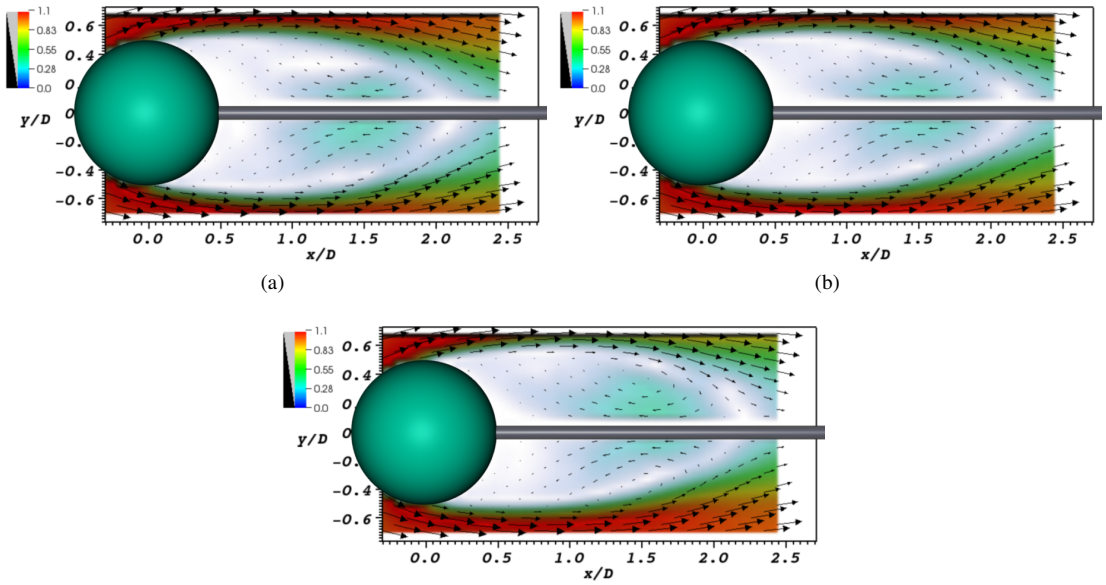

(a) (b)

(c)

Figure A.4: Consecutive averages over $\hat{t} = 50$ showing large scale movement of the wake for $\chi = 0.09$, with color indicating nondimensional velocity magnitude, (a) $100 < \hat{t} < 150$, (b) $150 < \hat{t} < 200$, and (c) $200 < \hat{t} < 250$.

by examining the temporal data for $\chi = 0.09$, which revealed that the orientation of the entire wake seems to move slowly. Figure A.4 shows three consecutive averages over a dimensionless time of $\hat{t} = 50$ (~ 10 wake oscillations), in which the mean wake is seen to move from being oriented slightly below the sting to significantly above it. It would not have been obvious that the entire wake was moving if only half of the plane had been imaged. This movement was seen to varying degrees for the different χ, likely because we are only examining a planar cut, and motion normal to the field of view would not be easily detected. The relation of the large-scale wake motion and the wake instability warrants further investigation. A low frequency motion was also found in the computational study of Yun *et al.* (2006) in the analysis of drag and lift. For $Re = 3700$, they found the frequency of the large scale lift motion to be $St \approx 0.025$ ($\Delta\hat{t} \approx 40$). This makes it difficult to obtain converged data, especially if attempting to simultaneously resolve the high frequency shear roll-up. Not shown here, we found that at $Re = 12,000$ convergence took even longer, as indicated by Yun *et al.* (2006) for $Re = 10,000$.

Figure A.3 shows the convergence of the maximum Reynolds shear stress (average of maximum from the top and bottom wake), $\overline{u'v'}_{max}/U_\infty^2$, for a representative sample of different χ. A similar trend is seen for $\overline{v'v'}$, but convergence is worse for $\overline{u'u'}$ due to the large-scale motion of the wake in the radial direction, and the steep gradient of the streamwise velocity in the shear layer.

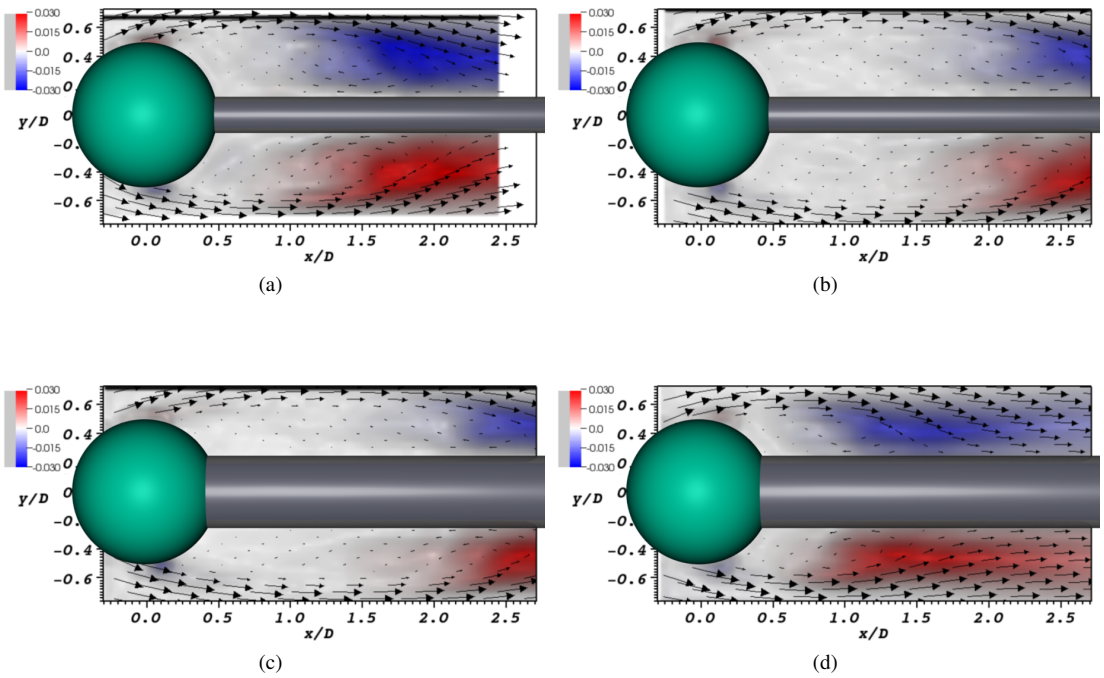

Figure A.5: Mean velocity field overlaid with the mean Reynolds shear stresses $\overline{u'v'}/U_\infty^2$ (a),(b) $\chi = 0.25$: left has higher free stream turbulence (c),(d) $\chi = 0.50$: right sphere has low amplitude vibrations.

A.4.2 Mean Wake

As observed by previous researchers (Bakić, 2004; Kim & Durbin, 1988), we have also found that the length of the mean recirculation region reduces due to both higher free stream turbulence and disturbances near the natural frequency of the shear layer instability. Figure A.5 shows the average velocity field overlaid with the dimensionless Reynolds shear stress. In figures A.5a and A.5b the same χ is shown, but the free stream turbulence is higher in the former case, which causes a more rapid growth of the shear layer instability, leading to a shorter wake length, which is here defined as the location along the sting at which the streamwise velocity changes directions (which could be considered a mean stagnation point). In figures A.5c and A.5d a larger χ is shown, with the difference between the two being that the latter has disturbances in the boundary conditions which have a frequency peak that lies within the St range measured by others for the shear layer instability, as will be detailed in subsection A.4.3.

Even with these differences in wake length, it is still possible to examine the effect of χ by comparing the χ for each sphere size. To examine the shape of the average velocity magnitude, a cubic spline curve was fit to each column of data to find the position of the maximum and minimum velocity to subpixel accuracy. The velocity contour $u = U_\infty/2$, was also determined as it is useful for comparing the mean wake shape for the different sphere sizes. Here we will focus on the smallest sphere (largest χ), as no differences were found for the smaller χ, within the scatter of the data. Figure A.6a shows representative paths of the mean wake

for the three different χ of the smallest sphere. Within the scatter of the data, the mean path of the wake does not change with χ, except for perhaps between a χ of 0.6 and 0.8. This indicates that the mean path of the wake is largely determined by the energetic outer flow. Along these minimum and maximum paths, the velocity magnitude is similar for the different χ, up to approximately $\chi = 0.50$ (not shown). For larger χ (figure A.6b) there are deviations in the downstream maximum, and significant changes in the shape of the minimum, indicating a change in how fluid is transferred to and from the mean recirculation region. However, more data is necessary to determine how the wake length and χ interact, as it is possible that $\chi < 0.50$ also produce deviations in the mean velocity magnitude for the case of the short wake.

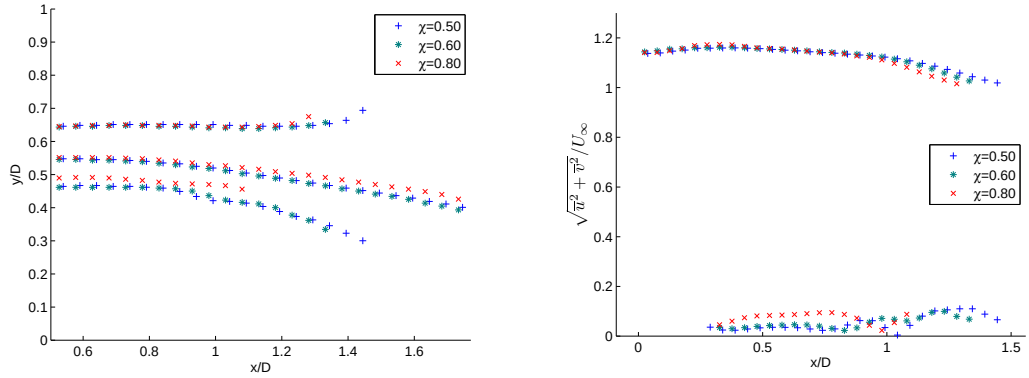

Figure A.6: Shape of the mean wake for $D = 0.016$m: (a) paths of maximum (top), minimum (bottom), and constant $U_\infty/2$ (center) velocity magnitude. (b) Velocity magnitude along the maximum and minimum paths.

To compare the effect of free stream turbulence and vibrations, the $U_\infty/2$ contour is shown in figure A.7 for all χ. This demonstrates that the importance of χ on the path of the mean wake is almost insignificant compared with these other effects. This trend would need to be examined for different flow regimes, such as higher Reynolds numbers where the shear layer transitions further upstream (Yun *et al.*, 2006) and the Strouhal number of the shear layer becomes much larger than that of the wake instability (Sakamoto & Haniu, 1990).

An example of the mean Reynolds stress fields are shown in figures A.8 and A.5d, for the small sphere with $\chi = 0.50$. The average of the top and bottom maximum of the Reynolds stresses are shown in figure A.9, along with those obtained in the computational study of Yun *et al.* (2006) (for a Reynolds number of 3700). The data is noisy for smaller χ due to convergence issues, but a general trend of decreasing stresses with increasing χ is observed. The error bars are meant to give a sense of the convergence, and indicate the maximum and minimum values from the convergence plots (see, e.g., figure A.3) for $\hat{t} > 125$. Particularly noteworthy is the rapid drop in $\overline{v'v'}$ between $\chi = 0.60$ and 0.80, because the sting is growing in the y-direction. Here the area blockage ratio, χ^2, jumps from 0.36 to 0.64. It would be useful to fill in χ around 0.80 to verify

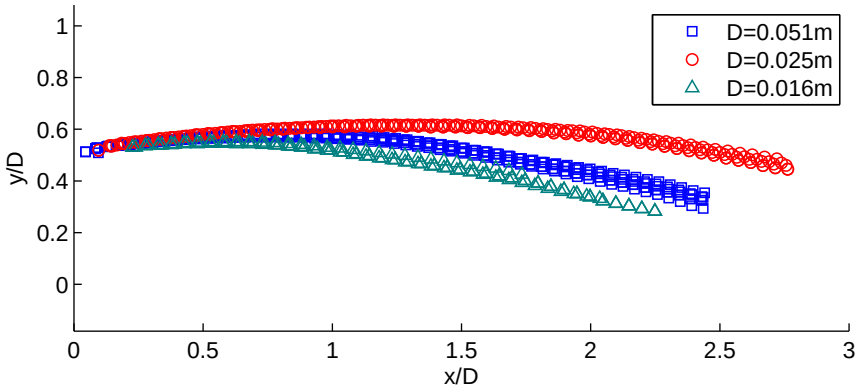

Figure A.7: Paths of constant $U_\infty/2$ for each sphere size, showing influence of free stream turbulence and vibrations.

and better understand this trend. It should also be noted that, within the scatter of the data, the higher free stream turbulence and the vibrations simply caused an earlier growth of the shear instability and did not significantly affect the maximum Reynolds stresses.

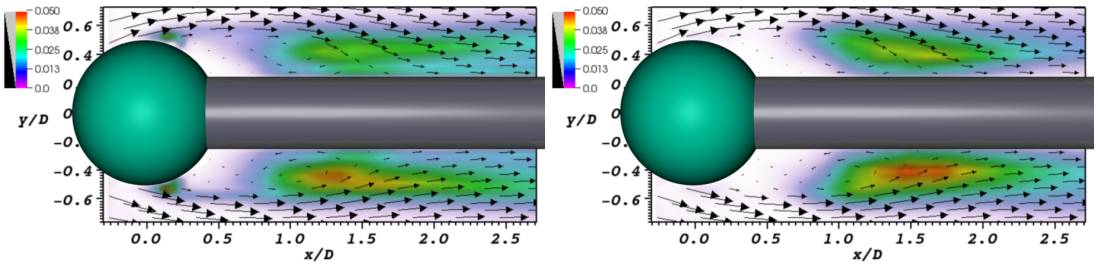

(a) (b)

Figure A.8: Mean Reynolds stresses for $\chi = 0.50$, $D = 0.016$m (a) $\overline{u'u'}$, (b) $\overline{v'v'}$.

A.4.3 Periodic Behavior

Strong frequency peaks corresponding to the wake instability were not detected in this study, possibly because the magnitude of the oscillations are small in the near wake, and also the Reynolds number of the current experiments lies in the range in which Sakamoto & Haniu (1990) labeled a transitional region because no distinct frequency peaks were detected. In addition, no frequency peaks corresponding to the shear layer instability were found for the two sphere sizes which had longer wakes, likely due to the slow roll-up of the shear layer. However, for the short wake the shear instability was detected easily by taking a fast Fourier transform of the time-resolved PIV vector fields.

Figure A.10 shows a map of the wake with color indicating the strength of the shear layer peak, normalized by the maximum value in each image. The left side shows the streamwise (u) component, while the right shows the radial (v) component. These patterns are to be expected for vortices rolling up along a shear layer.

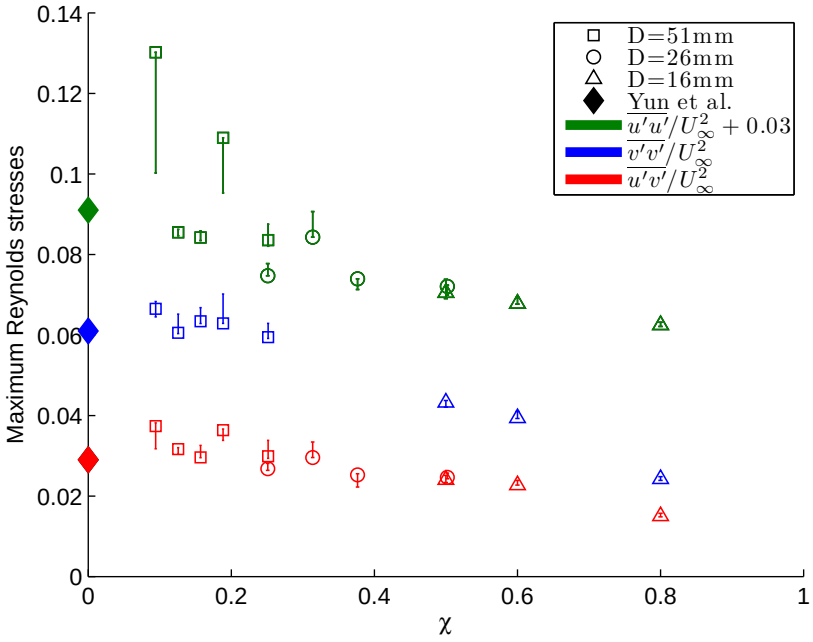

Figure A.9: Maximum of mean Reynolds stresses as a function of χ, with error bars based on convergence. Computational results from Yun *et al.* (2006) shown for comparison

Comparing the top ($\chi = 0.50$) and bottom ($\chi = 0.80$) parts of figure A.10, it is seen that the larger sting significantly encroaches on the vortex paths of the smaller sting case. Also, the maximum peak for the larger sting is 65% as strong as that of the smaller sting for the u-component and 58% for the v-component (whereas the strength of the maximum peaks for $\chi = 0.60$ is diminished by less than 10%). Thus the roll-up of the shear layer is damped, which matches well with the Reynolds stresses decreasing with increasing χ.

As shown in figure A.11, the peaks of the shear layer frequency in the wake agree well with the low amplitude frequency of the sphere vibrations. It appears that the facility noise, in the form of acoustic excitation and/or sphere vibrations, enhanced the instability of the shear layer. For comparison, Sakamoto & Haniu (1990) found the frequency of shear layer roll-up to range from $1.0 < St < 1.3$ for Re near 3800. For $\chi = 0.80$ both the vibration peak and the wake peak are slightly broader.

A.5 Conclusion

Investigations have been performed examining the effect of the sting size on flow over a sphere using high speed PIV. Due to the low frequency wake oscillations, and an apparent lower frequency wake motion, data needs to be taken over many wake oscillations to achieve convergence. Here integration was performed over a nondimensional time of 250, which was sufficient to draw general conclusions. However, acquiring data over a longer time would be preferred. It was also noted that it appears to be more difficult to obtain converged

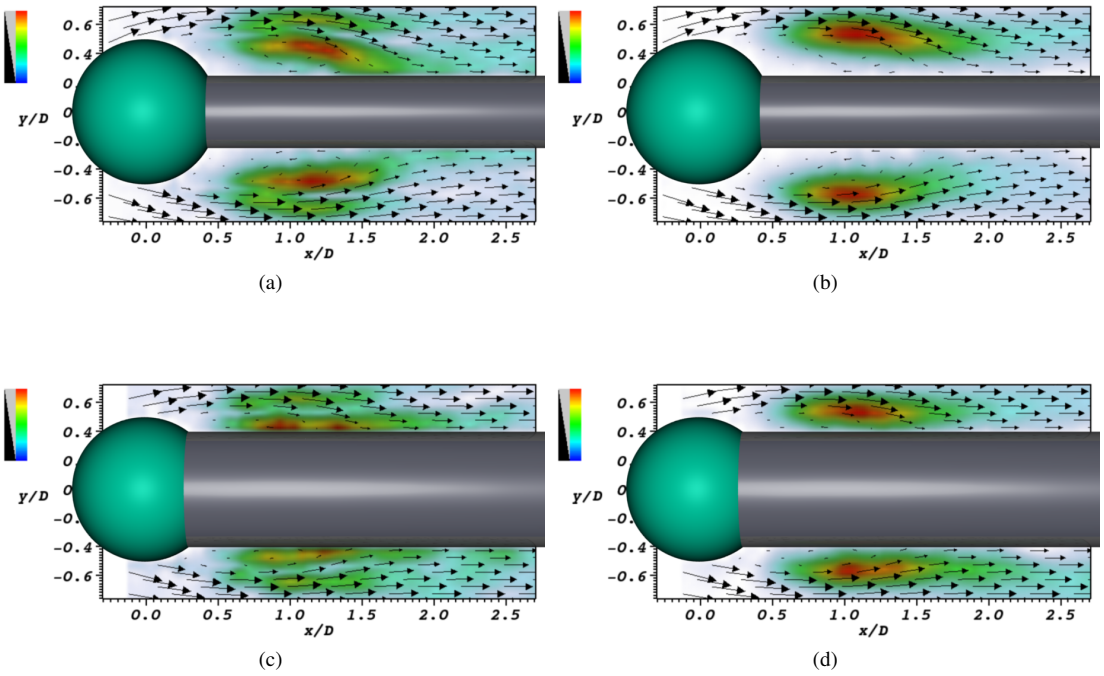

Figure A.10: Magnitude of frequency spectrum peak (streamwise on the left and radial on the right) as a function of position, normalized by the maximum value for each image, where the maximum peak in (c) is 65% as strong as in (a), and the maximum peak in (d) is 58% as strong as in (b). (a),(b) $\chi = 0.50$, $St = 1.085$ (c),(d) $\chi = 0.80$, $St = 1.081$.

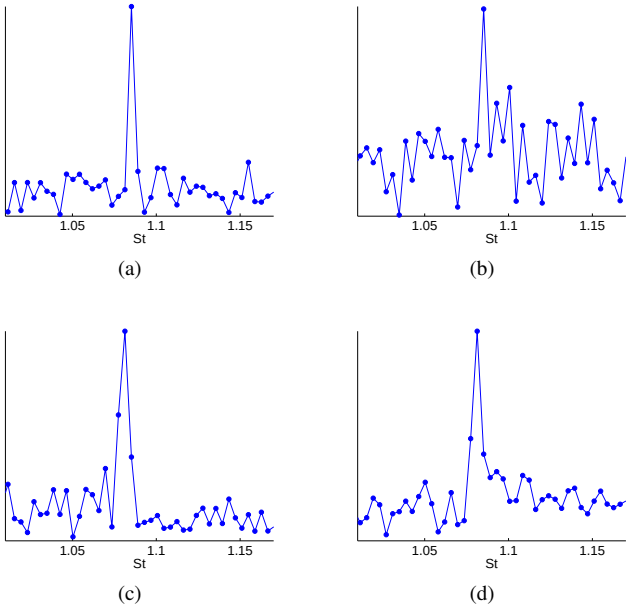

Figure A.11: (a),(c) Representative frequency spectrum of u-velocity and (b),(d) vibration frequency of spheres, for $\chi = 0.50$ on the top and $\chi = 0.80$ on the bottom.

statistics at higher subcritical Reynolds numbers.

As expected, the effect of a a sting behind a sphere is a weak analogy to the splitter plate behind a cylinder, due to the three-dimensional nature of the sting.

The mean wake was shown to not change significantly for $\chi < 0.50$, and the Reynolds stresses decrease with increasing χ. It was also shown that both increased free stream turbulence and excitation at a naturally unstable frequency have a larger impact on the shape of the mean wake than χ, at least for $\chi < 0.80$.

Disturbing the flow at a frequency within the range of naturally unstable shear layer frequencies was shown to produce early transition of the shear layer, causing the vortices to roll-up at the same frequency as the acoustic noise and/or sphere vibrations. The energy associated with this frequency drops dramatically when χ is increased from 0.60 to 0.80.

Thus, taking into account the shape of the mean wake, the maximum mean Reynolds stresses, and the shear layer instability, it appears that even with $\chi = 0.50$ the properties of the mean wake are only slightly changed from that of a sphere with a negligible diameter support. Of course, it would be best to use the smallest sting possible, however, using a χ up to ~ 0.25 seems appropriate if needed. This would need to be verified for other Reynolds numbers, and the effect on the wake instability should also be investigated. These conclusions may change if the interest lies in examining unsteady forces or instantaneous fields.

Bibliography

ACHENBACH, E. 1972 Experiments on the flow past spheres at very high Reynolds numbers. *Journal of Fluid Mechanics* **54** (03), 565–575.

ACHENBACH, E. 1974*a* The effects of surface roughness and tunnel blockage on the flow past spheres. *Journal of Fluid Mechanics* **65** (01), 113–125.

ACHENBACH, E. 1974*b* Vortex shedding from spheres. *Journal of Fluid Mechanics* **62** (02), 209–221.

ANDERSON, E. A. & SZEWCZYK, A. A. 1997 Effects of a splitter plate on the near wake of a circular cylinder in 2 and 3-dimensional flow configurations. *Experiments in Fluids* **23** (2), 161–174.

ÅSTRÖM, K. J. & MURRAY, R. M. 2008 *Feedback Systems: An Introduction for Scientists and Engineers*. Princeton Univ Pr.

BACON, D. L. & REID, E. G. 1924 The resistance of spheres in wind tunnels and in air. *Tech. Rep.* 185. Langley Memorial Aeronautical Laboratory.

BAKIĆ, V. 2004 Experimental investigation of a flow around a sphere. *Original Sciences Paper* **1**, 63–81.

BAKIĆ, V. & PERIĆ, M. 2005 Visualization of flow around sphere for Reynolds numbers between 22000 and 400000. *Thermophysics and Aeromechanics* **12** (3), 307–315.

BEARMAN, P. W. & HARVEY, J. K. 1976 Golf ball aerodynamics. *Aeronautical Quarterley* **May**, 112–122.

CHOI, J., JEON, W. P. & CHOI, H. 2006 Mechanism of drag reduction by dimples on a sphere. *Physics of Fluids* **18**, 041702.

CHOMAZ, J. M., BONNETON, P. & HOPFINGER, E. J. 2006 The structure of the near wake of a sphere moving horizontally in a stratified fluid. *Journal of Fluid Mechanics* **254**, 1–21.

CONSTANTINESCU, G. S. & SQUIRES, K. D. 2003 LES and DES investigations of turbulent flow over a sphere at Re = 10,000. *Flow, Turbulence and Combustion* **70** (1), 267–298.

CONSTANTINESCU, G. S. & SQUIRES, K. D. 2004 Numerical investigations of flow over a sphere in the subcritical and supercritical regimes. *Physics of Fluids* **16** (5), 1449.

DARABI, A. & WYGNANSKI, I. 2004*a* Active management of naturally separated flow over a solid surface. Part 1. The forced reattachment process. *Journal of Fluid Mechanics* **510**, 105–129.

DARABI, A. & WYGNANSKI, I. 2004*b* Active management of naturally separated flow over a solid surface. Part 2. The separation process. *Journal of Fluid Mechanics* **510**, 131–144.

FAGE, A. 1937 Experiments on a sphere at critical Reynolds numbers. *Rep. Mem. Aero. Res. Counc. London* **1766**, 108.

GERRARD, J. H. 1966 The mechanics of the formation region of vortices behind bluff bodies. *Journal of Fluid Mechanics* **25** (02), 401–413.

GHARIB, M. 1983 The effect of flow oscillations on cavity drag, and a technique for their control. PhD thesis, California Institute of Technology.

HOERNER, S. 1935 Tests of spheres with reference to Reynolds number, turbulence, and surface roughness. technical memoradum no. 777. *National Advisory Committee for Aeronautics, Langley, Virginia* .

HOROWITZ, P. & HILL, W. 1989 *The Art of Electronics*. University Press.

HOWE, M. S., LAUCHLE, G. C. & WANG, J. 2001 Aerodynamic lift and drag fluctuations of a sphere. *Journal of Fluid Mechanics* **436**, 41–57.

JEON, S., CHOI, J., JEON, W., CHOI, H. & PARK, J. 2004 Active control of flow over a sphere for drag reduction at a subcritical Reynolds number. *Journal of Fluid Mechanics* **517**, 113–129.

JUKES, T. N. & CHOI, K. S. 2009*a* Flow control around a circular cylinder using pulsed dielectric barrier discharge surface plasma. *Physics of Fluids* **21**, 084103.

JUKES, T. N. & CHOI, K. S. 2009*b* Long lasting modifications to vortex shedding using a short plasma excitation. *Physical Review Letters* **102** (25), 254501.

KIM, H. J. & DURBIN, P. A. 1988 Observations of the frequencies in a sphere wake and of drag increase by acoustic excitation. *Physics of Fluids* **31**, 3260.

LAUCHLE, G. C. & JONES, A. R. 1998 Unsteady lift force on a towed sphere. *Journal of Fluids and Structures* **12** (8), 949–958.

MAXWORTHY, T. 1969 Experiments on the flow around a sphere at high Reynolds numbers. *Trans. ASME: J. Appl. Mech* **36**, 598–607.

MEHTA, R. D. 1985 Aerodynamics of sports balls. *Annual Review of Fluid Mechanics* **17** (1), 151–189.

MORKOVIN, M. V. 1985 Bypass transition to turbulence and research desiderata. In *In NASA. Lewis Research Center Transition in Turbines p 161-204 (SEE N85-31433 20-34)*, pp. 161–204.

NORMAN, A. K. & MCKEON, B. J. 2008 Effect of sting size on the wake of a sphere at subcritical Reynolds numbers. In *AIAA-2008-4237*.

RAFFEL, M., WILLERT, C., WERELEY, S. & KOMPENHANS, J. 2007 *Particle Image Velocimetry: a Practical Guide*. Springer Verlag.

RAJAMANI, M. R. & RAWLINGS, J. B. 2009 Estimation of the disturbance structure from data using semidefinite programming and optimal weighting. *Automatica* **45** (1), 142–148.

ROSHKO, A. 1955 On the wake and drag of bluff bodies. *J. Aeronaut. Sci* .

ROSHKO, A. 1961 Experiments on the flow past a circular cylinder at very high Reynolds number. *Journal of Fluid Mechanics* **10** (03), 345–356.

SAKAMOTO, H. & HANIU, H. 1990 A study on vortex shedding from spheres in a uniform flow. *ASME, Transactions, Journal of Fluids Engineering* **112**, 386–392.

SCHEWE, G. 1982 A multicomponent balance consisting of piezoelectric force transducers for a high-pressure wind tunnel. *Sensors and systems'82* pp. 13–23.

SCHEWE, G. 1983 On the force fluctuations acting on a circular cylinder in crossflow from subcritical up to transcritical Reynolds numbers. *Journal of Fluid Mechanics* **133**, 265–285.

SEIFERT, A., GREENBLATT, D. & WYGNANSKI, I. J. 2004 Active separation control: an overview of Reynolds and Mach numbers effects. *Aerospace Science and Technology* **8** (7), 569–582.

STANISLAS, M., OKAMOTO, K. & KAHLER, C. 2003 Main results of the first international PIV challenge. *Meas. Sci. Technol* **14** (10), R63–R89.

STANISLAS, M., OKAMOTO, K., KÄHLER, C. J. & WESTERWEEL, J. 2005 Main results of the second international PIV challenge. *Experiments in Fluids* **39** (2), 170–191.

SURYANARAYANA, G. K. & PRABHU, A. 2000 Effect of natural ventilation on the boundary layer separation and near-wake vortex shedding characteristics of a sphere. *Experiments in Fluids* **29** (6), 582–591.

TANEDA, S. 1978 Visual observations of the flow past a sphere at Reynolds numbers between 10^4 and 10^6. *Journal of Fluid Mechanics* **85** (01), 187–192.

UNAL, M. F. & ROCKWELL, D. 1988*a* On vortex formation from a cylinder. Part 1. The initial instability. *Journal of Fluid Mechanics* **190**, 491–512.

UNAL, M. F. & ROCKWELL, D. 1988*b* On vortex formation from a cylinder. Part 2. Control by splitter-plate interference. *Journal of Fluid Mechanics* **190**, 513–529.

WELCH, P. 1967 The use of fast Fourier transform for the estimation of power spectra: a method based on time averaging over short, modified periodograms. *IEEE Transactions on Audio and Electroacoustics* **15** (2), 70–73.

WHITE, F. M. 2006 *Viscous Fluid Flow*. McGraw-Hill.

WILLIAMS, D. R., TADMOR, G., COLONIUS, T., KERSTENS, W., QUACH, V. & BUNTAIN, S. 2009 Lift response of a stalled wing to pulsatile disturbances. *AIAA journal* **47** (12), 3031–3037.

WILLMARTH, W. W. & ENLOW, R. L. 1969 Aerodynamic lift and moment fluctuations of a sphere. *Journal of Fluid Mechanics* **36** (03), 417–432.

YUN, G., KIM, D. & CHOI, H. 2006 Vortical structures behind a sphere at subcritical Reynolds numbers. *Physics of Fluids* **18**, 015102.